UNIVERSITY OF OKLAHOMA

GRADUATE COLLEGE

CHARACTERISTICS OF TROPOPAUSE POLAR VORTICES BASED ON OBSERVATIONS OVER THE GREENLAND ICE SHEET

A THESIS

SUBMITTED TO THE GRADUATE FACULTY

in partial fulfillment of the requirements for the

Degree of

MASTER OF SCIENCE IN METEOROLOGY

By

SARAH MICHELLE BORG
Norman, Oklahoma
2018

Downloaded from SHAREOK. Persistent Handle URL: https://hdl.handle.net/11244/316253

CHARACTERISTICS OF TROPOPAUSE POLAR VORTICES BASED ON OBSERVATIONS OVER THE GREENLAND ICE SHEET

A THESIS APPROVED FOR THE
SCHOOL OF METEOROLOGY

BY

Dr. Steven Cavallo, Chair

Dr. David Turner

Dr. Greg McFarquhar

© Copyright by SARAH MICHELLE BORG 2018
All Rights Reserved.

Acknowledgments

First and foremost, I would like to thank all of my committee members for their continued guidance and support throughout this project and my degree. To Dr. Steven Cavallo, thank you for believing in me from day one in your class, encouraging me through all of the difficult times (academic and personal), and always welcoming my questions, large or small. Thank you for giving me the opportunity to study at OU and work with the amazing research group you have here. Dr. Dave Turner, thank you for continuing to be present throughout the past two years, even from miles away. You have always made time for me in your busy schedule, challenging my knowledge and helping me grow as a researcher. From Skype radiation lessons to ARM field projects, I have learned a tremendous amount from you and have felt your support in every step. To Dr. Greg McFarquhar, thank you for your advice, suggestions, and welcoming attitude with anything I have brought to you, and especially for being present at my talk at the AMS Radiation Conference in Vancouver. Having a familiar face there to support me in a sea of people I did not know meant so much to me.

Secondly, I would like to thank my family: my mom, dad, and Amanda. Each of you have provided so much support and comfort through some of my most difficult times in this journey. Mom, thank you for answering my phone calls in the middle of the night when my anxiety got the best of me and always having the right words to say. Dad, thank you for providing logical reasoning for my toughest situations and knowing that is how I work through things. And when no one else did, you always remembered and cared about even the smallest things I had going on. Amanda, thank you for always reminding me that everything would be OK, for having pride in every one of my accomplishments, and for understanding me when no one else did. I love all of you so much.

To Allie Brannan: Thank you for being my first, and best, friend since I stepped foot in Norman. Throughout my time in grad school, you have been the person I have gone to for anything and everything, school related or not, even after you left. I am so appreciative

to have someone who relates to me on so many levels. The friendship I have with you, and the reassurance you have provided in every moment of doubt I have had through my time in this program is incredibly special to me.

To all of my friends from my first year here - Elisa, Amanda, Ryann, Kelsey, Matt, Tyler, Brian, and Andrew: Thank you for pulling me through my first semester in a new field and a tough program. Thank you for never judging me for the dumb questions I asked in class or the extra help I needed on homeworks. I have loved all of the time we have spent together, from discussing nightmares at every pre-class meet up to daily lunch talks reaching death in a matter of minutes. You all have truly made my experience in this program better than I could have ever imagined, and I know I have friends for a lifetime.

To my office mates - Zach and Dylan: Thank you both for welcoming me into your space and providing countless hours of coding help, study sessions, snacking, venting, and general advice about anything and everything. My thesis and my passing grades in every class would definitely have not been possible without the sacrifices you both have made to help me along the way. I have loved all the fun times we've had, from office decorating and bird tornadoes to stupid videos and trips to The Baked Bear. I literally could not ask for more genuine people to spend every day with while I was here.

To AAARG - Thank you all for always proving a safe space for me to share my work and providing constructive feedback on everything. The knowledge you have all shared with me along the way has helped me grow as a researcher. Thank you all for always being happy to help with any questions, problems, or worries I had.

And finally, Zachary Chambers. Thank you for coming into my life right as I began one of the most difficult challenges in this degree and being nothing but patient, supportive, and proud. You have done so much for me in the way of relieving stress and putting everything in perspective any time I was overwhelmed. Leaning on you throughout this semester has truly gotten me through the times when I had no motivation to move forward. Thank you for always being my rock.

Table of Contents

Acknowledgments iv

List of Tables viii

List of Figures ix

Abstract xix

1 Introduction and Background 1
- 1.1 Definition and Properties of Tropopause Polar Vortices . . . 2
  - 1.1.1 Structure . . . 3
  - 1.1.2 Theoretical Framework . . . 3
- 1.2 Tropopause Polar Vortex Intensity Changes . . . 5
  - 1.2.1 Case Study . . . 6
  - 1.2.2 Composite Study . . . 6
- 1.3 Properties of the Arctic Atmosphere . . . 13
  - 1.3.1 Early Studies . . . 13
  - 1.3.2 Recent Studies . . . 16
  - 1.3.3 Properties of the Atmosphere Over Greenland . . . 28
- 1.4 Motivation and Goals . . . 39

2 Data and Methodology 42
- 2.1 Data . . . 42
  - 2.1.1 ERA5 Data and Usage . . . 42
  - 2.1.2 TPV Tracks . . . 43
  - 2.1.3 Instrumentation at Summit Station, Greenland . . . 45
  - 2.1.4 Shupe-Turner Algorithm . . . 48
- 2.2 Methods . . . 51
  - 2.2.1 Verification of Composite Structure . . . 51
  - 2.2.2 Rapid Radiative Transfer Model . . . 52
    - 2.2.2.1 Clear-Sky . . . 53
    - 2.2.2.2 All-Sky . . . 56

3 Results and Analysis 62
- 3.1 Case Study . . . 62
- 3.2 General Characteristics and Composites . . . 80
  - 3.2.1 Atmospheric State Properties . . . 80
  - 3.2.2 Observed Structure . . . 83
  - 3.2.3 Observed Radiative Properties . . . 87

3.2.3.1 Strengthening Cases 87
3.2.3.2 Weakening Cases 92
3.2.4 Cloud Properties 99

4 Summary and Conclusions **104**

Reference List **108**

List of Tables

1.1 Summary of the experiment types run by Cavallo and Hakim (2013) to test the effects of longwave radiation, shortwave radiation, water vapor, and microphysics on TPV amplitude changes. 13

2.1 Table detailing specifications, measurements, and derived parameters for instruments at Summit Station. Original table from Shupe et al. (2013). . . 47

2.2 Summary of experiments run for this study using the RRTM and different forcings. An X represents the presence of the forcing in the respective experiment. 61

List of Figures

1.1 West-east composite cross sections of anomalous (a) temperature (K), (b) v-wind component (m s^{-1}), (c) Ertel potential vorticity (PVU), (d) and relative humidity (%) constructed by Cavallo and Hakim (2010). 4

1.2 Time-height cross sections of anomalous EPV tendency in PVU hr^{-1} due to (a) all diabatic effects, (b) radiation, (c) latent heating, and (d) all others for a vortex case study. (Cavallo and Hakim 2009). 7

1.3 Composite west-east cross sections of (a) total diabatic heating rate, (c) radiative heating rate, and (e) latent heating rate in K day^{-1}. The right panel ((b), (d), (f)) shows the anomalous heating rate for the respective properties. (Cavallo and Hakim 2010). 9

1.4 Composite west-east cross sections of anomalous EPV tendency in PVU day^{-1} due to (a) all diabatic effects, (b) radiation, (c) latent heating, and (d) all others excluding radiation and latent heating. (Cavallo and Hakim 2010). 10

1.5 TPV amplitude changes over a 5 day period, computed on the 2-PVU surface. These are the results of the experiments run by Cavallo and Hakim (2013) which are described in table 1.1. 13

1.6 Zonal-mean vertical distributions of specific humidity for annual, winter, and summer months (Serreze et al. 1995). 16

1.7 Annual cycles of a) solar surface cloud forcing and b) longwave surface cloud forcing from SHEBA (Intrieri et al. 2002b). 19

1.8 Map of the locations of Arctic observatories including the SHEBA field campaign and ASCOS. Figure 1 from Shupe et al. (2013). 19

1.9 Comparison of monthly mean profiles of air temperature from radiosonde stations (red) and six reanalyses (gray) used by Serreze et al. (2012) including MERRA, CFSR, NCEP-I, ERA-40, ERA-I, and JRA-25 for the period 1979-2001. The gray shading shows the range in the air temperature between the six reanalyses based on data at the grid point closest to the radiosonde sites. Figure 3 from Serreze et al. (2012). 22

1.10 Comparison of monthly mean profiles of specific humidity from radiosonde stations (red) and six reanalyses (gray) used by Serreze et al. (2012) including MERRA, CFSR, NCEP-I, ERA-40, ERA-I, and JRA-25 for the period 1979-2001. The gray shading shows the range in the specific humidity between the six reanalyses based on data at the grid point closest to the radiosonde sites. Figure 3 from Serreze et al. (2012). 23

1.11 Time series from 1979-2010 of monthly standardized anomalies in surface to 500 hPa precipitable water at the nine radiosonde stations located in figure 1.15. A trend line is shown in black and confidence interval shown in parentheses Serreze et al. (2012). 24

1.12 Annual cycle of monthly mean cloud occurrence fraction at six Arctic observatories (Barrow, SHEBA, Summit, Atqasuk, NyClesund, and Eureka), with the black curve denoting the average cloud fraction for all sites. Past Arctic cloud fraction climatologies are also provided from Huschke (1969), Vowinkel and Orvig (1970), and Warren et al. (1988). Figure from Shupe et al. (2011). 25

1.13 Annual cycles of monthly mean cloud occurrence fraction for different cloud types at (a) Barrow, (b) SHEBA, and (c) Eureka. Curves include the total cloud fraction (solid black), ice-only cloud fraction including snow (solid blue), liquid-only cloud fraction (solid red), liquid precipitation including drizzle and rain (solid orange), mixed-phase cloud fraction (solid light green), and mixed-phase column fraction (solid dark green). Dashed lines indicate the occurrence fractions for: ice in any type of cloud (dashed blue), liquid in any type of cloud (dashed red), and multiple, distinct layers of liquid water in any type of cloud (dashed orange). Figure from Shupe (2011). 26

1.14 Figure from Bennartz et al. (2013) showing frequency of occurrence of thin, liquid-bearing clouds at various Arctic observatories. For the purpose of this plot, "thin, liquid-bearing" clouds are defined as clouds in the range of 10 g m^{-2} < LWP < 60 g m^{-2}, corresponding to the range of maximum enhanced cloud radiative forcing at the surface. (a–d) Comparisons of ground-based observed (blue, microwave radiometer (MWR)) and ERA-Interim simulated (red, ERA) frequencies of occurrence of these clouds for four Arctic observation sites for all seasons and (e) Circumpolar map of the frequency of occurrence of these clouds from 32 yr of ERA reanalysis (1979–2011). The plot in e is conditionally sampled to only include cases with solar zenith angle lower than 80° and a surface albedo higher than 0.5. 27

1.15 Annual mean surface to 500 hPa precipitable water for the region north of 60 N from the MERRA reanalysis for January (upper left), April (upper right), July (lower left), and October (lower right), based on data from 1979-2010. The October panel also shows the locations of the nine radiosonde sites that were included in the analysis done by Serreze et al. (2012) 29

1.16 Monthly statistics of (a) cloud occurrence fraction as a function of height, (b) total cloud occurrence fraction in the vertical column (blue) and the occurrence fraction of liquid water (red), (c) low cloud-base (blue) and high cloud-top (red) heights when clouds are present, (d) maximum depth over which clouds occur (high top to low base, but not necessarily cloudy throughout), when clouds are present, (e) MWR-derived LWP in all conditions (red) and in those conditions identified as cloudy with a LWP $>$ 5 g m^{-2} (blue), and (f) Precipitation occurrence sensor system - derived snowfall occurrence fraction (red) and liquid-equivalent snowfall rate when snow is occurring (blue). Box-and-whisker plots contain information on the 5th, 25th, 50th, 75th, and 95th percentiles and mean (symbol). Figure 13 from Shupe et al. (2013). 32

1.17 A conceptual model from Morrison et al. (2011) illustrating the physical processes involved in the maintenance of Arctic mixed-phase clouds. . . . 33

1.18 Fractional occurrence of surface-based inversion (top) and SBI intensity (bottom) derived from MWR (black), radiosonde (blue), and meteorological tower 10m - 2m temperature difference. In the bottom panel, the box indicates the 25th and 75th percentiles, the whiskers indicate the 5th and 95th percentiles, the middle line is the median, and the asterisk indicates the mean. Figure from Miller et al. (2013). 33

1.19 Surface-based inversion intensity as a function of the mean LWP (top) and mean PWV (bottom) over a 5 minute window surrounding the temperature retrieval from the MWR for cases between July 2010 and May 2012. The box indicates the 25th and 75th percentiles, the whiskers indicate the 5th and 95th percentiles, the horizontal line indicates the median, and the asterisk indicates the mean. Figure from Miller et al. (2013). 34

1.20 Model sensitivity studies with respect to clouds and solar radiation. The turquoise curve represents T_{2m} without solar radiation, the blue curve represents T_{2m} assuming a cloud-free atmosphere (LWP 50 g m^{-2}), the purple curve showing T_{2m} assuming an atmosphere with a very thick cloud with constant LWP of 500 g m^{-2}, and the yellow curve shows the development of T_{2m} simulated using the surface energy balance model driven by simulated radiative fluxes based on water vapor path (WVP) and liquid water path (LWP). The inset shows simulated maximum T_{2m} based on LWP corresponding to the time between days 11 and 12 where the modeled temperature reaches above 0 °C. The red data point shows the observed T_{2m} and LWP at a time of ± 30 min around the time of maximum surface temperature (error bars, ± 1 s.d.) 35

1.21 Normalized vertical distribution of the median longwave and shortwave RHR values for varying amounts of ice in a single-layer, ice-only cloud, with respect to cloud top height and cloud base height. Figure from Turner et al. (2018). 38

1.22 Normalized vertical distribution of the median longwave RHR values for varying amounts of liquid in a single-layer, liquid-bearing cloud, with respect to cloud top height and cloud base height. Panel b) shows a closer look at the small-scale changes in heating rates close to 0. Figure from Turner et al. (2018). 38

1.23 The normalized vertical distribution of the median LW RHR for two-layer clouds (a),(b) where both layers contain some liquid water, or (c),(d) where only the bottom layer contains liquid water and the upper layer is ice only. The profiles were normalized between Sfc, first cloud base (CBH1), first cloud top (CTH1), second cloud base (CBH2), and second cloud top (CTH2). Figure from Turner et al. (2018). 39

2.1 The Shupe-Turner microphysics retrieval flowchart showing input measurement streams in green and individual algorithm elements in red boxes. (Shupe et al. 2015) 51

3.1 Hourly plots of potential temperature contours on the 2 PVU surface for $\pm$12 hours of the TPV passing over Summit on 2012-07-24 at 23Z (highlighted in blue). The red contour is representative of the TPV's core (minimum θ: 298 K, red contour: 300 K). Contours intervals are 10 K (i.e., the first black contour outward from the red contour is 310 K). 70

3.2 Line plots showing the TPV's amplitude (blue), core potential temperature (green), and last closed contour potential temperature (green dashed). The vertical red line represents the time of the TPV's closest passage, on 24 July 2012 at 23Z. The red shading represents the $\pm$6 hours from the TPV's closest passage 71

3.3 Time-height cross sections showing ice water concentration (top) and liquid water concentration (bottom) at Summit over the time period of the passing TPV on 24 July 2012. Ice water concentration is given in mg m^{-3} and liquid water concentration is given in g m^{-3}. 72

3.4 Time-height cross sections of a) temperature (K) and b) temperature anomalies (K) centered on 24 July 2012 at 23Z. Height is shown in km above ground level at Summit. The black vertical line represents the time the TPV's core was the closest to Summit, 24 July 2012 at 23Z. The blue line represents the height of the 2 PVU surface from ERA5. 73

3.5 Time-height cross sections of a) relative humidity with respect to liquid water (%) and b) relative humidity anomalies (%) centered on July 24th, 2012 at 23Z. Height is shown in km above ground level at Summit. The black vertical line represents the time the TPV's core was the closest to Summit, 24 July 2012 at 23Z. The blue line represents the height of the 2 PVU surface from ERA5. 74

3.6 Results from experiment 1 in table 2.2 showing the time-height cross section of a) all-sky, longwave RHR centered on 24 July 2012 at 23Z and b) the standardized anomalies of the all-sky, longwave RHR. The black vertical line represents the time the TPV's core was the closest to Summit. The blue line represents the height of the 2 PVU surface from ERA5. Black contours represent liquid clouds and white contours represent ice clouds. . . 75

3.7 Results from experiment 2 in table 2.2 showing the time-height cross section of a) clear-sky, longwave RHR centered on 24 July 2012 at 23Z and b) the standardized anomalies of the clear-sky, longwave RHR. The black vertical line represents the time the TPV's core was the closest to Summit. The blue line represents the height of the 2 PVU surface from ERA5. . . . 76

3.8 Results from experiments 3 and 4 in table 2.2 showing the heating rate profile from the mean water vapor and mean temperature (blue), and the mean temperature only (purple) in each layer over a 5-day period centered on 24 July 2012 at 23Z. 77

3.9 Results from experiments 5 and 6 in table 2.2 showing time-height cross sections of longwave RHR values from a) water vapor changes only, b) temperature changes only, and c) the difference between a and b centered on 24 July 2012 at 23Z. The black vertical line represents the time the TPV's core was the closest to Summit. The blue line represents the height of the 2 PVU surface from ERA5. 78

3.10 Results from experiments 7 and 8 in table 2.2 showing time-height cross sections of longwave RHR values from a) ice in clouds only and b) liquid in clouds only, centered on 24 July 2012 at 23Z. The black vertical line represents the time the TPV's core was the closest to Summit. The blue line represents the height of the 2 PVU surface from ERA5. Black contours represent liquid clouds and white contours represent ice clouds. 79

3.11 Scatter plot showing size, amplitude, and atmospheric state properties for the 40 TPVs in the analysis. The size and amplitude of each TPV are taken at the time of the TPV's closest point to Summit. Squares represent TPVs that strengthened, on average, over a 12-hour period surrounding the TPV's closest passage to Summit, and circles represent TPVs that weakened, on average, over the 12-hour period. Colors represent the average 12-hour difference between the maximum positive anomaly and minimum negative anomaly (i.e. the anomaly dipole) for a) temperature and b) water vapor mixing ratio for $\pm$6 hours from the TPV's closest point to Summit. 82

3.12 Composite time-height cross section of anomalous a) temperature (K) and b) relative humidity (%) for $\pm$24 hours of a TPV's closest passage to Summit, including TPVs passing Summit during the time period from March 2012 to October 2014. 84

3.13 As in figure 3.12 with anomalous a) v-wind (m s^{-1}) and b) u-wind (m s^{-1}). 86

3.14 Composite time-height cross section of RHR for a) clear-sky (experiment 2), b) water vapor contributions (experiment 5), and c) temperature contributions (experiment 6) based on $\pm$24 hours of a TPV's closest passage considering only TPVs that strengthened on average over a $\pm$6 hour period. 89

3.15 Composite time-height cross section of anomalous RHR for a) clear-sky (experiment 2), b) water vapor contributions (experiment 5), and c) temperature contributions (experiment 6) based on $\pm$24 hours of a TPV's closest passage considering only TPVs that strengthened on average over a $\pm$6 hour period. Anomalies are measured in standard deviations from the mean heating rate. 91

3.16 Composite time-height cross section of anomalous EPV tendency for a) clear-sky (experiment 2), b) water vapor contributions (experiment 5), and c) temperature contributions (experiment 6) based on $\pm$24 hours of a TPV's closest passage considering only TPVs that strengthened on average over a $\pm$6 hour period. Anomalies are measured in standard deviations from the mean EPV tendency, measured in PVU day^{-1}. 93

3.17 As in figure 3.14, but considering only TPVs that weakened on average over a $\pm$6 hour period. 95

3.18 As in figure 3.15, but considering only TPVs that weakened on average over a $\pm$6 hour period. 96

3.19 As in figure 3.16, but considering only TPVs that weakened on average over a $\pm$6 hour period. 98

3.20 Scatter plot showing size, amplitude, and cloud microphysical properties for the TPVs in the analysis with cloud data available. The size and amplitude of each TPV are taken at the time of the TPV's closest point to Summit. Squares represent TPVs that strengthened, on average, over a 12-hour period surrounding the TPV's closest passage to Summit, and circles represent TPVs that weakened, on average, over the 12-hour period. Colors represent the average 12-hour column integrated a) ice water path and b) liquid water path for $\pm$6 hours from the TPV's closest point to Summit. . . 101

3.21 Scatter plot showing size, amplitude, and average 12-hour heating rate anomaly on the tropopause for all TPVs included in the analysis. The size and amplitude of each TPV are taken at the time of the TPV's closest point to Summit. Squares represent TPVs that strengthened, on average, over the 12-hour period, and circles represent TPVs that weakened, on average, over the 12-hour period. Colors represent the average 12-hour heating rate anomaly on the tropopause for a) the clear-sky case and b) the all-sky case in terms of standard deviations from the mean. Panel c) shows the difference in the anomalies between b) and a). For cases with no cloud data available, the clear-sky anomaly averages were used for the both the clear-sky and the all-sky cases. 103

Abstract

Tropopause Polar Vortices (TPVs) are long-lived, coherent vortices that are identified by closed material contours of potential temperature on the dynamic tropopause. They are characterized by PV anomalies that spend most of their lifetime in the Arctic, can impact their surrounding environment by introducing variability in sea ice, generate surface cyclones, and intensify midlatitude weather systems when influenced by midlatitude Rossby waves. While several studies have modeled the structure and climatology of TPVs, there is much to be discovered in terms of their evolution, intensification, and genesis. Case studies and composite studies from previous model simulations have shown that changes in TPV intensity can be attributed to diabatic forcings such as radiative cooling and latent heating. Specifically, models indicate that clear-sky longwave radiative cooling is an important factor in the maintenance of TPVs while clouds can contribute to large amplitude changes in response to cloud-top radiative cooling in the vortex core. This study uses cloud and atmospheric state observations from Summit Station, Greenland, in combination with single column experiments using the Rapid Radiative Transfer Model (RRTM) to investigate the effects of clear-sky, ice-only, and all-sky radiative cooling on TPV intensification.

As part of the Integrated Characterization of Energy, Clouds, Atmospheric State, and Precipitation at Summit (ICECAPS) project, observations of tropospheric and cloud properties at Summit Station, Greenland have been collected since 2010. This ground-based observing system combined with temperature and humidity profiles from the European Centre for Medium-Range Weather Forecasts' fifth Reanalysis dataset (ERA5), which assimilates the twice-daily soundings launched at Summit, provides novel details of local characteristics of TPVs. Longwave radiative contributions to TPV diabatic intensity changes from both clouds and clear-sky water vapor effects are analyzed with these resources. A case study is broken down to consider cloud properties and the details of the radiative effects, followed by an in-depth composite study used to compare observed results to previously simulated results. Cloud and atmospheric state properties associated

with TPVs are also analyzed in this study via a breakdown of strengthening and weakening cases. Results from the case study show that clouds can sometimes be influential in the intensification of a TPV. Composite results share promising similarities to previous studies in terms of atmospheric state structure and radiative structure. Vertical gradients of clear-sky positive radiative heating rate (RHR) anomalies show positive (negative) signatures for strengthening (weakening) TPVs, contributing positively (negatively) to EPV tendency, as expected. Cloud property results show little indication that various TPVs have similar cloud features, however the presence of cloud water may be more common in smaller and/or weaker TPVs.

Chapter 1

Introduction and Background

Since 2005, there has been an increased focus on coherent vortices in the upper troposphere and understanding their impacts. The focus on tropopause vortices north of 65°N spurred from a general lack of understanding of these features due to previous studies' focus on tropospheric wave features (Hakim and Canavan 2005). Although the impacts of Tropopause Polar Vortices (TPVs) are still being discovered, upper tropospheric disturbances originating in the Arctic have been linked to a variety of important events. TPVs have been shown to influence the formation of surface cyclones (Hoskins et al. 1985), which can then have a variety of other impacts, depending on their location. Cyclones in the Arctic Sea have been shown to cause breaking of sea ice, therefore allowing for easier melt and transport out of the Arctic. One example of this is The Great Arctic Cyclone of 2012, as analyzed by Simmonds and Rudeva (2012), who track the formation of the cyclone back to a TPV that existed in the Arctic for sixteen days prior to its genesis. This storm was noteworthy for having reduced sea ice extent by four percent in the Arctic in an already anomalously low sea ice year. TPVs can also be carried equatorward by the jet stream where they can be precursors to midlatitude cyclones (Hoskins et al. 1985; Hakim et al. 1995). Midlatitude cyclones are commonly known to produce severe weather and other weather extremes. Knowing more about TPVs in terms of genesis, structure, evolution, and dynamics can lead to improved long-term forecasting for these severe events.

Several studies have since been completed to learn more about the structure, dynamics, and climatology of TPVs. All of these studies have been simulation-based, and no previous studies have looked in depth at observations of TPVs, especially on a local scale. The following sections will discuss the results of previous studies and the goals of the current study.

1.1 Definition and Properties of Tropopause Polar Vortices

Tropopause polar vortices are defined by closed material contours and can easily be identified as local extrema on a potential vorticity (PV) surface (Hakim and Canavan 2005). TPVs can exist as cold core cyclones or warm core anticyclones. Cold core vortices are associated with relatively cold air at the tropopause and warm core vortices are associated with warm air at the tropopause. Early studies defined a TPV as a closed contour that spends at least 60 percent of its lifetime north of 65°N and survives at least two days (Hakim and Canavan 2005). Using the six-hourly NCEP-NCAR reanalysis data from 1948-1999 to consider 9,023 Arctic cyclone tracks and 6,861 Arctic anticyclone tracks, Hakim and Canavan (2005) were the first to solidify many of the fundamental properties of TPVs based on a large sample population of vortices. In their study, the amplitude of a vortex was defined as the difference between the core potential temperature (i.e. the extrema value) and the potential temperature of the last closed contour on the 1.5 PVU surface. Cyclone tracks tended to coincide with preferred locations for surface cyclones, while anticyclone tracks did not, indicating the possibility that cold-core TPVs may be responsible for some Arctic storms.

The tracks showed that cyclones were more frequent than anticyclones in the 52-year period by 32 percent, and that the number of cyclone tracks peaks in the winter while the number of anticyclone tracks peaks in the summer. Cyclones had longer lifetimes than anticyclones, with both types of vortices lasting from days to weeks or even months. Anticyclones were found to be larger than cyclones, but both types of vortices were noted to be generally less than 1000 kilometers in radius. The amplitudes of both cyclones and anticyclones appeared at values up to 50 K with cyclones having slightly higher amplitudes than anticyclones.

The study by Hakim and Canavan (2005) provides many of the fundamental facts about TPVs that have allowed for the growth of this area of study. Since cold-core, cyclonic TPVs are precursors to surface cyclones and are more frequent in the Arctic, these have been the

focus of the majority of previous literature. For this reason, cold-core TPVs will also be the focus of this study. The remainder of this background as well as the results presented will focus on these cold-core features rather than their warm-core counterparts.

1.1.1 Structure

The composite structure of a cold-core TPV is shown in figure 1.1. This composite figure was created using WRF ARW model simulations with 568 vortex samples over a two year period. A cold-core TPV has anomalously warm temperatures above the background tropopause and anomalously colder temperatures below it. There are southerly winds on the east side of the vortex center and northerly winds on the west side, indicating cyclonic flow around the vortex center. Ertel potential vorticity (EPV) is shown to be anomalously high directly above the core of the TPV, and relative humidity anomalously low directly above the core. The anomalies described in temperature, EPV, and relative humidity can be noted as an effect of a lowering of the tropopause in the presence of a TPV. Since stratospheric air is warmer and drier than tropospheric air, these warm, dry anomalies exist where that stratospheric air intrudes to lower atmospheric levels. Since PV is higher in the stratosphere, the lowering of the tropopause allows for higher-PV air to fall into an environment that is surrounded by lower-PV air, creating the strong, positive EPV anomaly at the tropopause. The increased gradient in water vapor that is caused by the lowering of dry, stratospheric air is important when considering TPV maintenance and evolution (Cavallo and Hakim 2013). This idea will be discussed further in section 1.2.

1.1.2 Theoretical Framework

In order to understand the mechanisms that affect TPV evolution, it is important to look at the theoretical framework behind a TPV's amplitude, which is Ertel Potential Vorticity (EPV), as defined by Ertel (1942). In recent years, EPV has become a common feature for tracking air parcels and understanding atmospheric dynamics due to its usefulness in

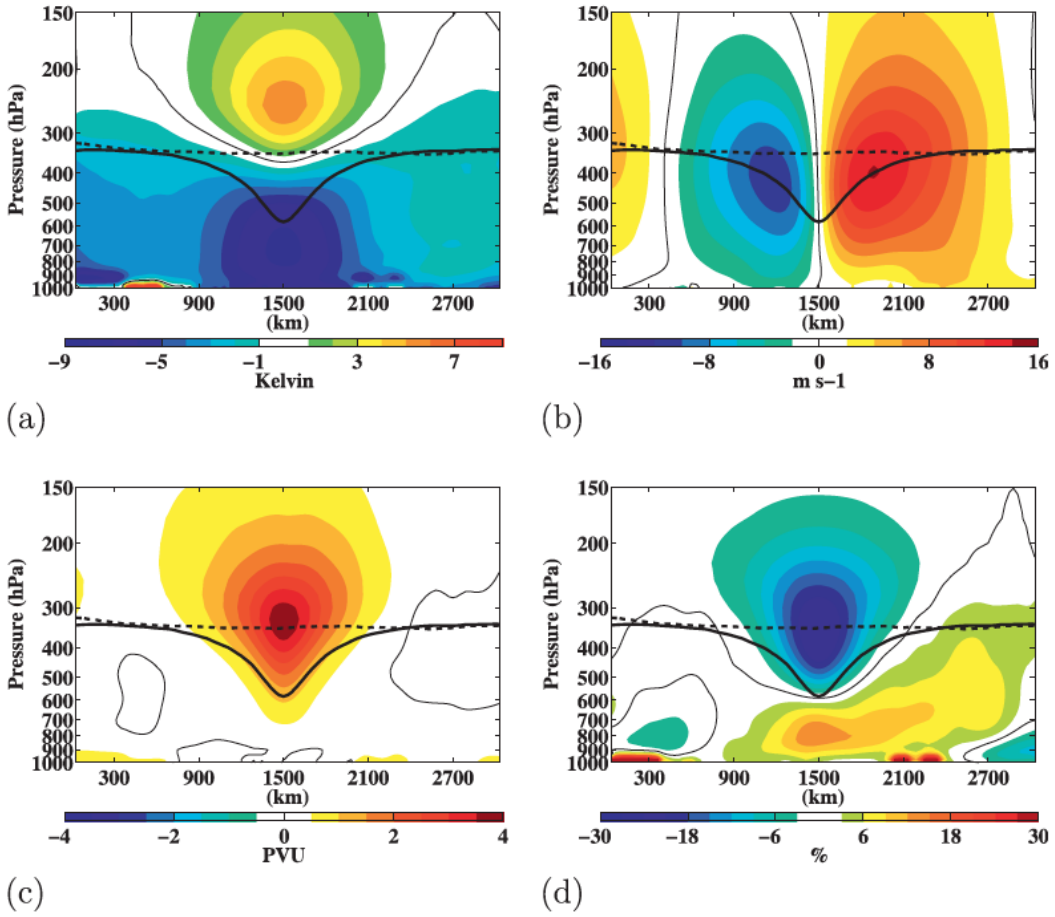


Figure 1.1: West-east composite cross sections of anomalous (a) temperature (K), (b) v-wind component (m s^{-1}), (c) Ertel potential vorticity (PVU), (d) and relative humidity (%) constructed by Cavallo and Hakim (2010).

retrieving properties of the flow field (Hoskins et al. 1985). Ertel potential vorticity is given by

$$\Pi = \frac{1}{\rho}\omega_a \cdot \nabla\theta \tag{1.1}$$

where ρ is the density, ω_a is the absolute vorticity, and θ is the potential temperature. Here, the gradient of potential temperature is representative of a TPV's amplitude. Considering the EPV tendency equation (Edwards and Pedlosky 1998), by taking the total derivative of

EPV with respect to time, one can then note that PV is conserved in the absence of diabatic and frictional effects (e.g. Holton 2004):

$$\frac{D\Pi}{Dt} = \frac{\omega_a}{\rho} \cdot \nabla \frac{D\theta}{Dt} \tag{1.2}$$

Since TPVs are based on the tropopause, which is far removed from the frictional effects of the boundary layer, one can assume that changes in PV contributing to TPV amplitude changes are due to diabatic effects. These diabatic effects may include radiation, latent heating, planetary boundary layer mixing, convection, and other mixing and diffusional processes. However, in the Arctic, there are consistently low temperatures and widespread cloudiness (see section 1.3) allowing for a further break down of the EPV tendency equation into diabatic contributions mostly attributed to radiation and latent heating:

$$\frac{D\Pi}{Dt} = \frac{\omega_a}{\rho} \cdot \nabla(\dot{\theta}_{\text{radiation}} + \dot{\theta}_{\text{latent heating}} + \dot{\theta}_{\text{other}}) \tag{1.3}$$

Cavallo and Hakim (2009) go through a component-wise breakdown of a TPV's PV tendency that leads to the theory presented in this section regarding a TPV's intensity. The details of this study and others that lead to our current understanding of how TPVs evolve is presented in section 1.2.

1.2 Tropopause Polar Vortex Intensity Changes

Before detailing the PV aspects, Cavallo and Hakim (2009) investigate whether synoptic scale patterns may lead to vortex intensification. Large scale dynamics were studied in a 264-case composite centered on a latitude-longitude box where maximum cyclone growth was shown to occur in climatology. The 500 hPa height patterns beginning 120 hours before maximum cyclone growth remained largely unchanged until the time of maximum cyclone growth implying that these synoptic patterns do not precede intensity changes at locations distant from the vortex. While large-scale dynamics don't impact intensity changes, these

large-scale dynamics may be important for TPV genesis, such as wave breaking, vortex splitting, etc., however genesis and lysis of TPVs requires further research.

1.2.1 Case Study

The bulk of the study done by Cavallo and Hakim (2009) considers a single observed event and uses numerical modeling to provide a complete PV budget. They hypothesize that radiative tendencies will dominate latent heating tendencies when it comes to the creation and destruction of PV due to the fact that the cold temperatures of the Arctic do not allow water vapor to exist in high amounts such as it would in the midlatitudes or tropics. For the chosen case, which was a cyclonic TPV that existed from 1 November to 7 December, 2005, they break down the lifetime into an intensification phase and a weakening phase to consider the EPV tendencies for both. For the intensification phase, results showed that the net EPV creation was positive mostly due to cloud-top radiative cooling even though the effects of latent heating acted to destroy some EPV below the tropopause, as shown in figure 1.2. The results of the simulation for the weakening phase were not as conclusive as for the intensification phase, however it was noted that there was a strong EPV tendency dipole found due to latent heating below the tropopause and radiation contributed only slightly to a positive EPV tendency near the tropopause.

1.2.2 Composite Study

The results of the case study detailed in Cavallo and Hakim (2009) led to another study to further investigate how diabatic forcings contribute to TPV amplitude changes based on changes in EPV. The goal, then, of Cavallo and Hakim (2010) was to determine if the results found in Cavallo and Hakim (2009) held true in the context of a much larger sample of TPVs. For the study, a model simulation was set up with a domain over the Canadian Arctic, as this has been noted as a high-density location for the existence and intensification of cold-core TPVs (Hakim and Canavan 2005). Cyclonic vortices were identified by locating

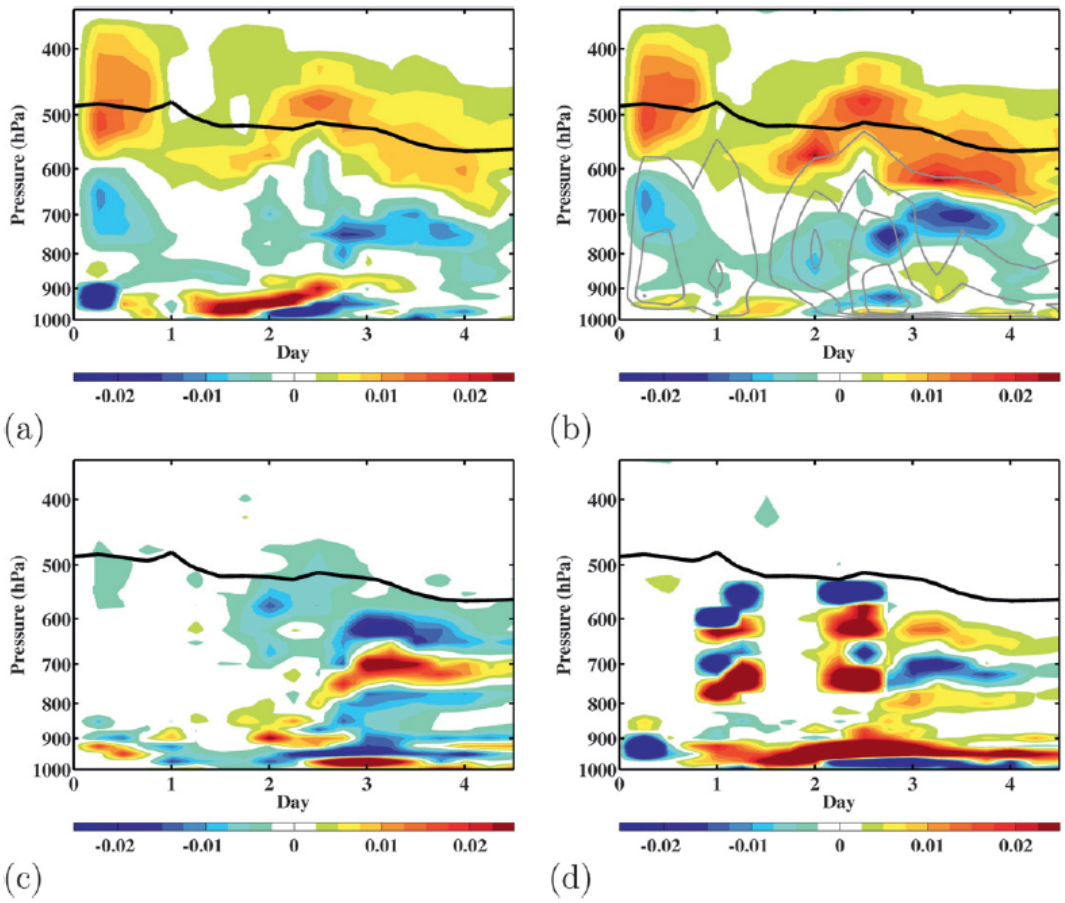


Figure 1.2: Time-height cross sections of anomalous EPV tendency in PVU hr^{-1} due to (a) all diabatic effects, (b) radiation, (c) latent heating, and (d) all others for a vortex case study. (Cavallo and Hakim 2009).

the minimum potential temperature on the dynamic tropopause, which is defined as the 2 PVU surface, and scanning outward along eight equally spaced radials to determine where the gradient in potential temperature changed signs. This point was considered the last closed contour, or the bounding contour, of the TPV, and the TPV's amplitude would then be determined by the absolute difference between the potential temperature of the bounding contour and the core. Using this method, a total of 568 vortices were determined during a 2-year period to consider in the composite analysis of a TPV's structure (see section 1.1.1)

and radiative properties. In addition to the determination of a composite structure, composite west-east cross sections of diabatic tendency terms were also created from this analysis. The composite total heating rate resulted in the largest cooling at the tropopause with this cooling mostly due to radiative effects (figure 1.3). These radiative effects create a dipole in heating rate anomalies centered on the vortex, with high anomalies above the tropopause and low anomalies below. Similarly, composite west-east cross sections of EPV tendency are found in the vortex core just above the tropopause for both total diabatic forcings and radiative forcings, while a negative tendency is found due to latent heating just below the tropopause at the core (figure 1.4). It is clear from the analysis that the EPV tendency due to radiative effects had the largest contribution to the total EPV tendency in the core of the TPV. This suggests that cyclonic TPVs would tend to intensify on average due to radiative effects, as these outweigh the destructive effects of latent heating on EPV, which is consistent with the fact that TPVs are Arctic features. It is also hypothesized by Cavallo and Hakim (2010), due to these results, that the lowering of the tropopause in the presence of a TPV induces EPV generation because of an increased vertical gradient in water vapor, and hence an increased vertical gradient in heating rate across the tropopause.

Since the Arctic is characterized by several months of little to no solar radiation each year, it is important to also consider how this lack of solar radiation affects TPVs. TPVs are generally isolated from the midlatitude jet stream, and they can exist for long periods of time in the Arctic (weeks to months), allowing for long-term radiative affects to play a larger role in their evolution. Cavallo and Hakim (2012) showed that without radiation (shortwave or longwave), TPVs tend to weaken over time, on average, and their amplitudes have a greater reduction during the summer due to increased water vapor in the Arctic atmosphere. It is also noted that changes in TPV lifetime lengths can be affected by radiation as well, since in the summer the mid-latitude jet stream has less of an influence on TPVs (i.e. the region where TPVs exist), allowing radiation to play a greater role in the maintenance of the TPV. However, while the study done by Cavallo and Hakim (2012)

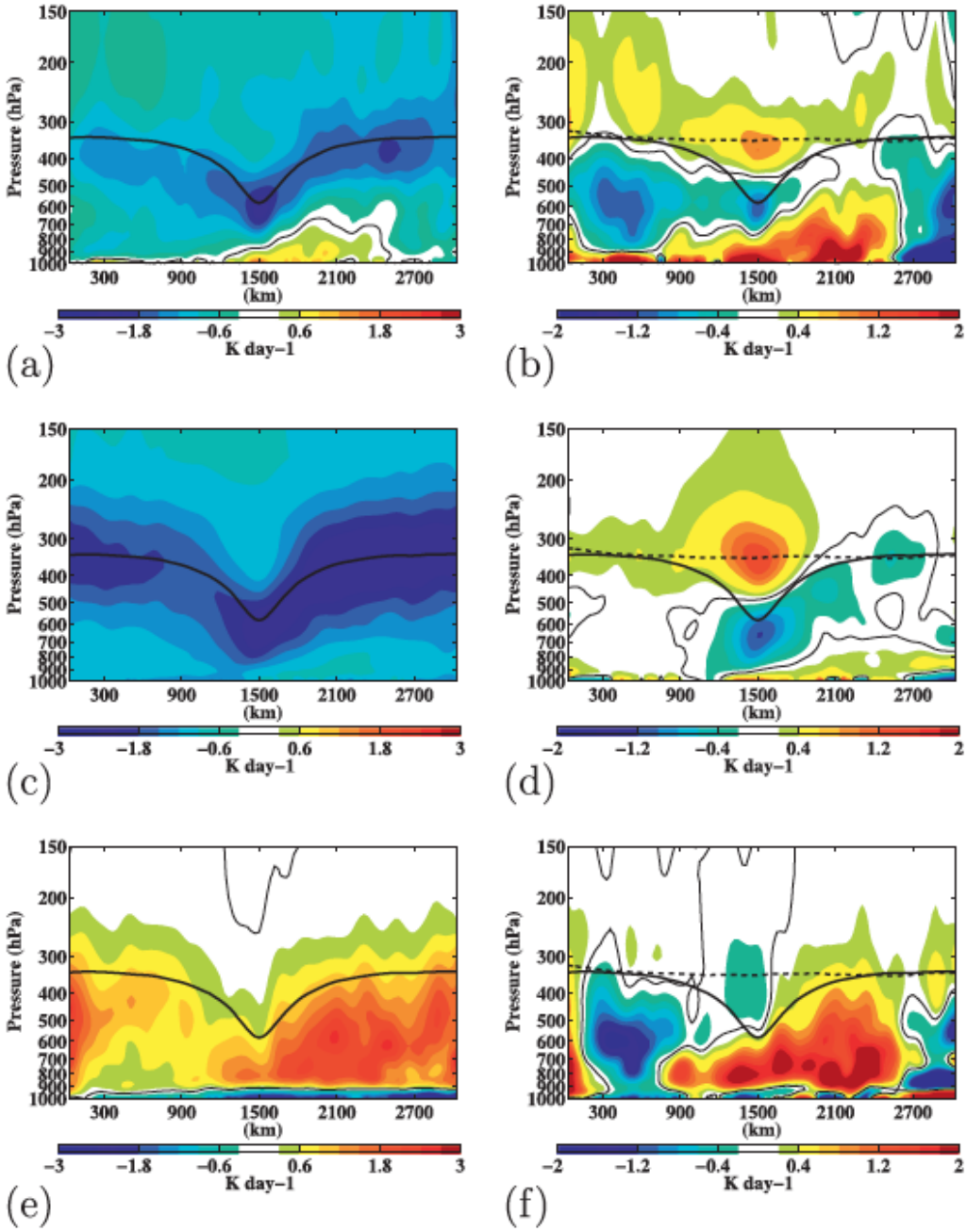


Figure 1.3: Composite west-east cross sections of (a) total diabatic heating rate, (c) radiative heating rate, and (e) latent heating rate in K day^{-1}. The right panel ((b), (d), (f)) shows the anomalous heating rate for the respective properties. (Cavallo and Hakim 2010).

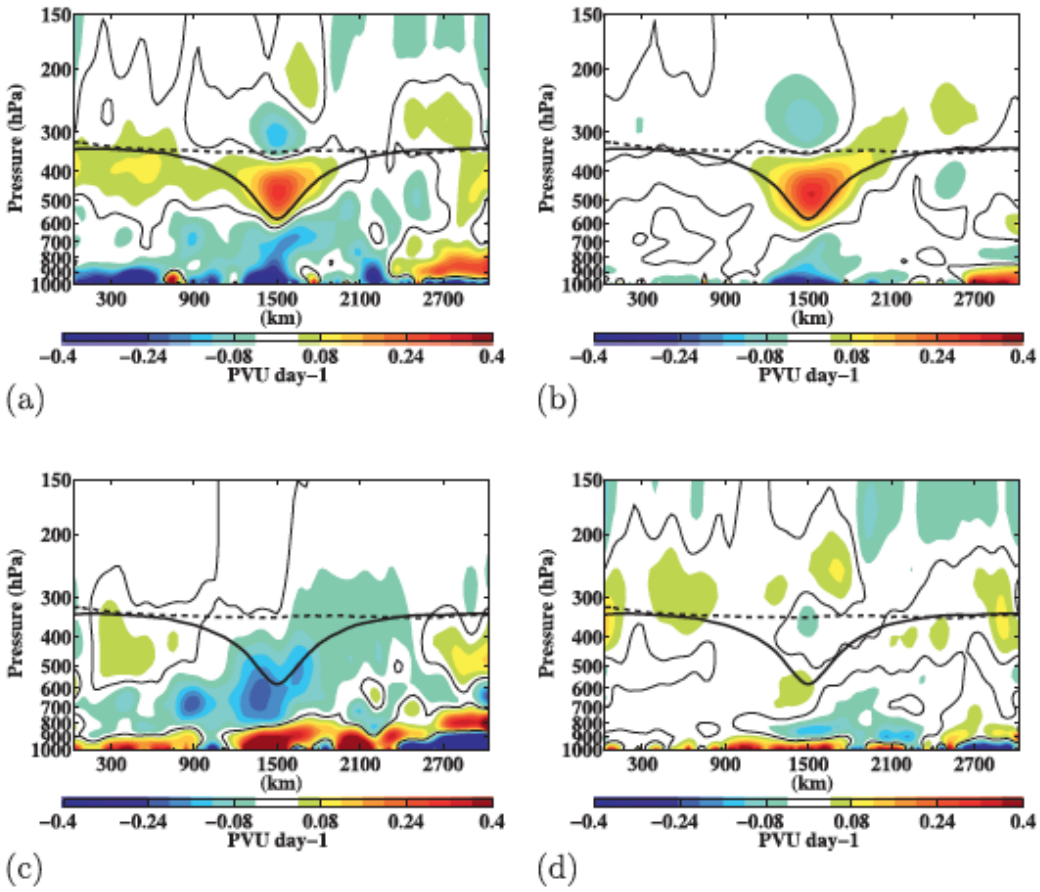


Figure 1.4: Composite west-east cross sections of anomalous EPV tendency in PVU day^{-1} due to (a) all diabatic effects, (b) radiation, (c) latent heating, and (d) all others excluding radiation and latent heating. (Cavallo and Hakim 2010).

investigates long-term, large-scale effects of radiation on TPVs, they also note that their approach in this study does not allow for a more detailed, localized understanding of the radiative effects on TPVs. Since radiation had already proven to be a significant contributor to TPV evolution (Cavallo and Hakim 2009, 2010, 2012), Cavallo and Hakim (2013) set up an experimental study to determine how local factors such as water vapor, shortwave radiation, longwave radiation, and clouds all influenced TPV amplitude over a five-day period. To do so, idealized numerical modeling experiments were performed with different

mechanisms isolated each time. A summary of the experiments is provided in table 1.1, and the results of the simulations shown in figure 1.5.

Experiments 2 and 3 are representative of clear-sky cases. An experiment is characterized as "clear-sky" when temperature, water vapor, and other aerosol effects are considered in the radiative transfer calculations, however the effects of clouds are ignored. Experiments 4 and 5 investigate the effects of cloud microphysics in addition to the clear-sky variables. Experiment 1 is unique in the sense that water vapor is isolated from the standard clear-sky environment, allowing for a consideration of the specific effects of water vapor on TPV amplitude changes. All five experiments show the vortex amplitude increasing over the five-day period.

Experiment 1 shows a small but steady increase in amplitude over the 5 day period. This is due to the fact that EPV tendency is dependent on vorticity as well as the vertical heating rate gradient. In the background environment, EPV generation is based on density, Coriolis parameter ($f = 2\Omega$ sin(lat)) and vertical heating rate, however, in the vortex, the vertical component of relative vorticity is also included. Since relative vorticity is large within the vortex, this contributes to the positive EPV tendency and hence the amplitude increase of the TPV. Experiment 2, which includes water vapor, shows a 16.8% greater increase in amplitude at the end of the 5 day period than experiment 1. Water vapor is a strong absorber of longwave radiation, and within the vortex, the water vapor gradient is stronger because of the dry air intrusion. In this experiment, intensification occurs because longwave cooling is enhanced in the vortex core compared to the surrounding environment. Experiment 3, which includes water vapor and shortwave radiation, has results similar to those in experiment 2, however the resulting amplitude is slightly lower. Since shortwave radiation is not as strongly absorbed by water vapor as longwave radiation, the shortwave heating that results from the water vapor gradient across the tropopause in the vortex core has only a small negative contribution to the EPV tendency, as compared to the contribution from the longwave cooling. This causes slowed intensification, but intensification still

occurs. Experiments 1 through 3 together support the hypothesis presented in Cavallo and Hakim (2009) that an increased vertical gradient in water vapor due to the lowered tropopause acts as a mechanism for intensification.

Experiments 4 and 5 also show an overall increase in TPV amplitude over the five-day period, while not as steady as the clear-sky cases. The amplitude peaks found in the 20 - 40 hour range are due to additional EPV creation from enhanced longwave cooling in areas where vertical cloud gradients are present. While latent heating destroys EPV, it does not equally counteract the positive EPV tendency from the longwave cooling at cloud top. Experiment 4 shows the greatest increase in amplitude as longwave radiation is the most sensitive to clouds. In experiment 5, shortwave radiation is included, and this shortwave radiation reduces cloud content in the vortex, hence reducing the longwave cooling due to clouds. This leads to slower intensification of the vortex, but intensification still occurs similarly to experiments 2 and 3 due to the fact that shortwave radiative heating rates are more sensitive to water vapor than clouds.

Within the first 120 hours of the simulation, the TPV's amplitude sees a resulting increase in all experiments. It is important to note, however, that at the end of the five-day simulation, the vortices in the cloudy experiments had the highest amplitudes, and the experiments with longwave radiation and clouds in the absence of shortwave radiation was almost 4 K higher in amplitude than the complimentary experiment with shortwave included. These results suggest two important points:

1. Vertical water vapor gradients are an important factor in TPV evolution and strengthening during clear-sky cases.

2. Clouds are an important factor in TPV evolution and intensification, likely due to the increased radiative cooling they present.

Expt	Description
E1	LW, without H_2O
E2	LW, with H_2O
E3	LW, SW
E4	LW, MP
E5	LW, SW, MP

Table 1.1: Summary of the experiment types run by Cavallo and Hakim (2013) to test the effects of longwave radiation, shortwave radiation, water vapor, and microphysics on TPV amplitude changes.

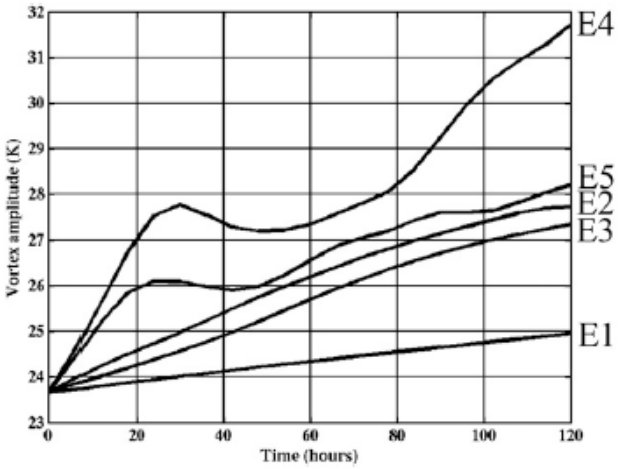


Figure 1.5: TPV amplitude changes over a 5 day period, computed on the 2-PVU surface. These are the results of the experiments run by Cavallo and Hakim (2013) which are described in table 1.1.

1.3 Properties of the Arctic Atmosphere

1.3.1 Early Studies

The desire to understand Arctic clouds has long been motivated by the desire to understand Arctic air masses as a whole. Arctic air masses play an important role in the heat budget of the Arctic Ocean, the evolution of synoptic systems, and the prediction of many weather phenomena by general circulation models (Curry 1983). Starting in the early 1930s (e.g.

the *Maud* expedition), studies have been done to better characterize Arctic air masses, providing important first steps in this area of research. Many studies described typical characteristics of continental polar air masses, one of the most important being the presence of deep surface based inversions that are caused by radiative cooling of the surface (e.g. Petterssen (1956), Belmont (1957), Vowinckel and Orvig (1970), Serreze et al. (1992)). These studies demonstrated that surface-based inversions occurred at least 50% of the time in the Arctic and consistently during the winter months (December through April), with the strongest inversions occurring in late winter. Wexler (1936) and Curry (1983) were among the first to investigate the structure of polar air masses and model the physical mechanisms leading to inversions in the Arctic. Since in idealized conditions (i.e. calm, cloudless, no solar radiation, no turbulent mixing and no subsidence), a snow or ice surface radiates much like a black body and the surface cools much faster than the overlying atmosphere, even when the overlying layer is emitting energy back towards the surface (Wexler 1936). Because the Arctic sees little to no solar radiation during most of the year, these surface based inversions are much more frequent and persistent than the common nocturnal inversions found at midlatitudes, which are generally mixed out by daytime heating. Curry (1983) investigated the mechanisms affecting the formation of polar continental air, complementing the idealized approach by Wexler (1936). For the clear-air cases (i.e. no condensate), temperature profiles found by Curry's model were very similar to those found by Wexler, however when condensate is present (often in the form of ice fog), the condensate allows the surface to warm and the inversion layer is shifted to the top of the fog layer, where longwave cooling is enhanced.

Curry (1983) also investigated the development of a humidity inversion, which was found to occur mainly due to gravitational ice crystal fallout and the deposition of hoar frost near the surface depleting the air mass of moisture. Although humidity inversions had been noted in previous literature, up to this point vertical profiles of moisture in the Arctic remained uncertain mostly due to the lack of observations available at high latitudes and

difficulty in measuring water vapor at high altitudes (Serreze et al. 1995). Advancements were made to close this gap by Serreze et al. (1995) in a study specific to water vapor characteristics north of 70° N. Specific humidity profiles in the Arctic show a linear decrease with pressure, with values generally dropping to near 0 g kg^{-1} above 300 hPa and 95% of the moisture concentrated below 500 hPa for all seasons, as shown in figure 1.6 by Serreze et al. (1995). It is clear that moisture varies greatly by season, but this variability is restricted mostly to the surface to 500-hPa layer (Figure 1.6).

While understanding the surface heat budget was the motivation to study Arctic air masses, understanding Arctic clouds was a very large part of this goal. Gathering accurate cloud observations in the Arctic remained a difficult task, mainly due to sparse observations and discrepancies between satellite and surface observations (Curry et al. 1996). The largest challenge in retrieving cloud properties from satellite and passive infrared sensors in the Arctic is the similarity in albedos and temperatures between clouds and the ice-covered surfaces below (Curry et al. 1996). Despite these discrepancies, cloud property data and cloud cover climatologies did still exist. Most reports, such as the International Satellite Cloud Climatology Project (ISCCP) climatology and a surface-based climatology by Warren et al. (1980) had a broad general agreement that cloud fraction (averaged above 60° N) was greater than 40% year-round with maximum values in the summer months. Summertime Arctic stratus clouds were studied by Herman and Goody (1976) who found that Arctic stratus clouds were often present in layers, however it was uncertain why this occurred. Along with cloud layering, mixed-phased clouds were a feature that had been observed in the Arctic boundary layer (e.g. Witte (1986), Curry and Radke (1994), Pinto et al (1995b), Curry et al. (1996)) during various field experiments. Curry and Herman (1985) also studied summertime Arctic stratus clouds as part of the 1980 Arctic Stratus Experiment, finding that longwave emission by these clouds had a large dependency on liquid water path and cloud drop size distribution.

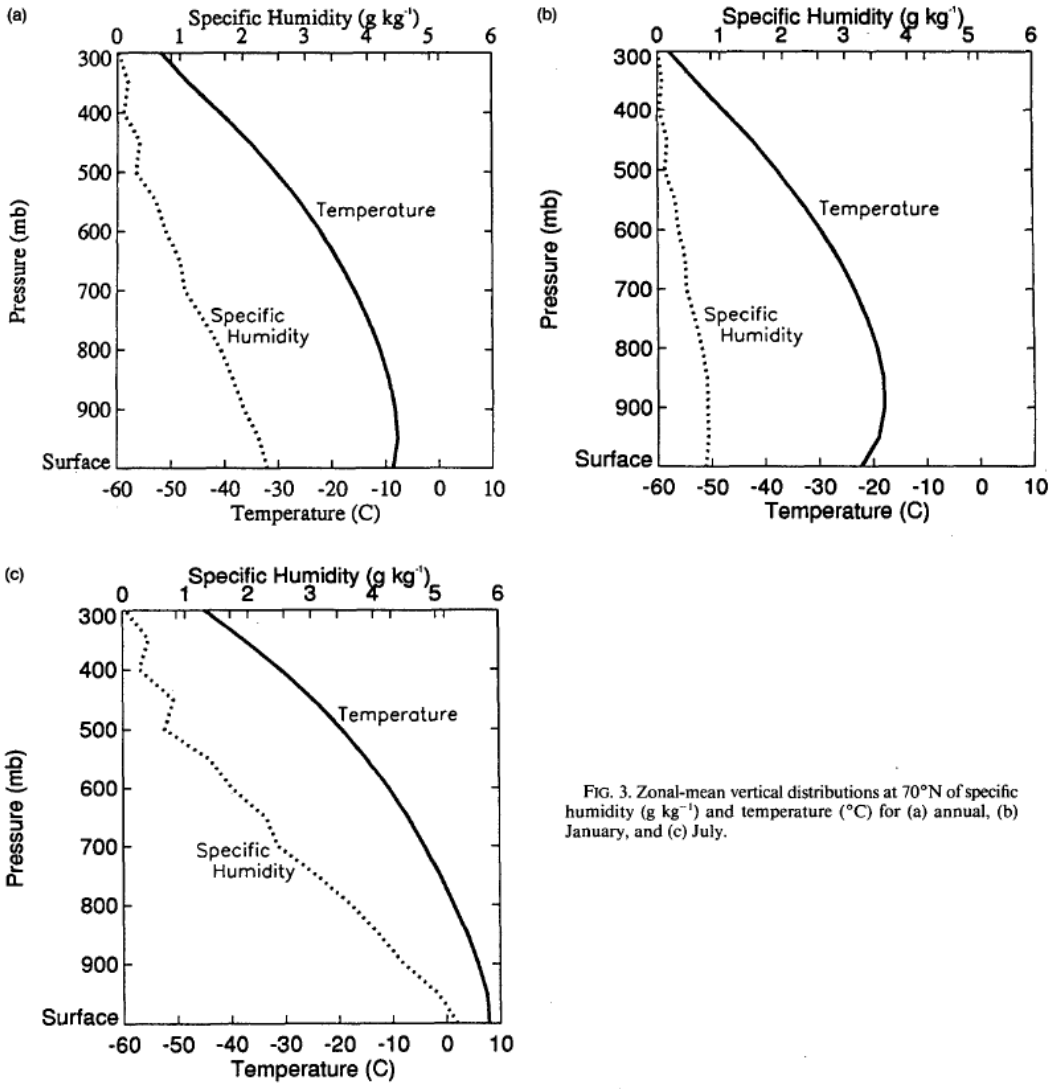


FIG. 3. Zonal-mean vertical distributions at 70°N of specific humidity (g kg^{-1}) and temperature (°C) for (a) annual, (b) January, and (c) July.

Figure 1.6: Zonal-mean vertical distributions of specific humidity for annual, winter, and summer months (Serreze et al. 1995).

1.3.2 Recent Studies

While much was known about Arctic thermodynamics by the early 1990s, many gaps in the understanding of Arctic clouds and their impact on radiation still existed. In 1995, plans began for a program called The Surface Heat Budget of the Arctic Ocean (SHEBA), which included a field experiment consisting of a drifting station in the pack ice of the Arctic Ocean between October 1997 and October 1998 (Uttal et al. 2002). While the main

goal of SHEBA was to gather measurements to improve model parameterizations of Arctic ocean–atmosphere–ice processes, SHEBA also allowed for numerous advances in our understanding of the physical processes occurring in the Arctic Ocean and cloud characteristics, and it was especially valuable due to the fact that it captured an entire annual cycle. Observations from SHEBA showed that the region sampled had cloud coverage 85% of the year, with the greatest cloudiness occurring in the September (up to 97%), and the least cloudiness occurring during the February (63%) (Intrieri et al. 2002a). SHEBA also showed, based on lidar measurements, that liquid-bearing clouds (i.e. clouds that included some amount of liquid), existed in every month of the SHEBA year, with August having the the greatest percentage of clouds containing liquid (Intrieri et al. 2002a). During SHEBA, stratus clouds were observed in up to five thin layers, although more commonly found in one or two well-defined layers (Intrieri et al. 2002a), in agreement with the findings of Herman and Goody (1976).

What is the impact of these observed cloud properties from SHEBA? Surface cloud radiative forcing (SCF) is a metric used by Shupe and Intrieri (2004) (following Ramanathan et al. (1989)) to assess the impact of clouds on the surface energy balance in comparison to clear-skies during SHEBA. SCF is defined as follows:

$$CF_{LW} = F(A_c) - F(0) \tag{1.4}$$

$$CF_{SW} = Q(A_c) - Q(0) \tag{1.5}$$

$$SCF = CF_{LW} + CF_{SW} \tag{1.6}$$

where A_c is the cloud fraction, F is the surface LW flux, and Q is the surface SW flux. $F(A_c)$ and $F(0)$ represent the all-sky and clear-sky conditions, respectively, and similarly for the SW forcing. A negative SCF implies clouds are acting to cool the surface, and a positive SCF implies clouds are acting to warm the surface. Intrieri et al. (2002b) conclude that for all months except July (during SHEBA), clouds produce a net warming effect on

the surface, the opposite effect of that in lower latitudes (Figure 1.7). This effect was similarly discussed by Curry et al. (1996). During July, solar zenith angle is the lowest, albedos are low, and clouds reflect more incoming solar radiation away from the surface. SHEBA also led to the conclusions that cloud surface forcing is a function of phase, optical depth, liquid water path, particle size, cloud temperature, cloud height, and to a smaller degree, solar zenith angle and surface albedo (Shupe and Intrieri 2004), which are several more factors than previously hypothesized. The majority of longwave radiatively impactful clouds were low-lying (i.e. bases below 4.3 km) and relatively warm due to frequent temperature inversions (Shupe and Intrieri 2004). Shupe and Intrieri (2004) also found that cloud forcing in the longwave was particularly sensitive to liquid water paths below 30 g m^{-2} however above this threshold not as sensitive. Altogether, SHEBA provided information on cloud types, cloud macro and microphysical properties, and cloud radiative properties over an annual cycle that pushed the boundaries of the current state of understanding of the Arctic atmosphere. It is important to note, however, that SHEBA was based over very high latitudes and observations are specific to Arctic Ocean air masses. An important next step in research was applying the knowledge gained by SHEBA to other Arctic locations and continental air masses such as those over the Greenland Ice Sheet.

The last decade, especially, has led to further advancements in our understanding of Arctic thermodynamics and cloud properties due in large part to field campaigns such as SHEBA and the Arctic Summer Cloud Ocean Study (ASCOS) as well as the implementation of more Arctic observatories such as those at Barrow (Alaska), Atqasuk (Alaska), Eureka (Nunavut), Ny'Alesund (Norway), and Summit (Greenland) (Figure 1.8). Together, these projects have provided more frequent and complete observations for analysis. In addition to Arctic observatories, models and satellite technology have improved, in particular the launching of active profiling systems (CloudSat and CALIPSO) assisted in providing much improved retrieved cloud properties from satellites (e.g. Lacour et al. (2017)). As

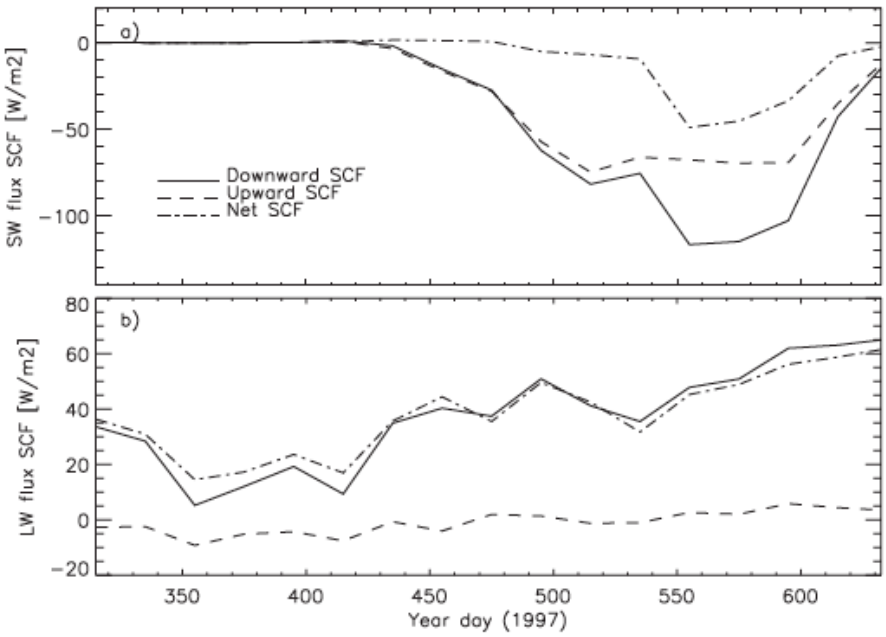


Figure 1.7: Annual cycles of a) solar surface cloud forcing and b) longwave surface cloud forcing from SHEBA (Intrieri et al. 2002b).

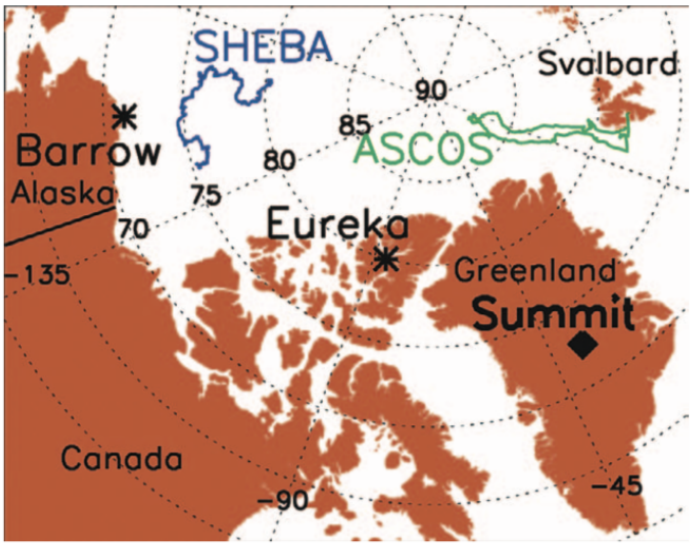


Figure 1.8: Map of the locations of Arctic observatories including the SHEBA field campaign and ASCOS. Figure 1 from Shupe et al. (2013).

another example of improved analysis techniques, Serreze et al. (2012) compiled observations from nine high latitude radiosonde stations and six atmospheric reanalyses to examine changes in tropospheric water vapor over a 30-year period around the globe. This study tied together previous knowledge of Arctic tropospheric water vapor and water vapor profiles while also providing a climatological look at large-scale changes. Radiosonde analyses showed consistency with previous studies in terms of surface based inversions in temperature and humidity (Figures 1.9, 1.10), but reanalyses still did not appear to capture these inversions well, especially the humidity inversions. While providing valuable analyses regarding water vapor properties in the Arctic, the main takeaway from the study done by Serreze et al. (2012) is the fact that water vapor characteristics are consistent with a changing Arctic environment. Statistically significant trends in precipitable water over the Arctic are mostly positive for all nine locations of interest (Figure 1.11), however uncertainties in radiosonde and reanalysis data are still high due to the difficult nature of obtaining accurate humidity data in polar regions.

Another example of recent exploitation of available Arctic observations is a study done by Shupe et al. (2011), who compared cloud thermodynamic and macrophysical properties between various Arctic observatories. Comparisons between the observations from six Arctic observatories and previous studies show general agreement in annual cloud occurrence fraction with values above 40% at most sites for the entire year and the highest cloud occurrence fractions during summer months (Shupe et al. 2011) (Figure 1.12). It is shown, however, that the winter cloud fraction is higher at many sites than suggested by previous studies. Shupe (2011), a complimentary study to Shupe et al. (2011), focused on microphysical properties of clouds and cloud occurrence by type from three of the six Arctic observatories containing a full suite of cloud-observing instruments to determine phase. It was found that ice clouds are the most common, while mixed-phase clouds are still more prevalent than liquid-only clouds (Figure 1.13). Liquid water in clouds occurred often during summer months and at least 10%-20% of the time during winter months, and was

observed at temperatures as cold as -40°C indicating that supercooled liquid and mixed-phase clouds are not uncommon even at high latitudes (Shupe 2011; Bennartz et al. 2013) (Figure 1.14). It is worth noting that higher percentages of occurance of liquid-bearing clouds exist in locations that are on (SHEBA) or near (Barrow, Eureka) oceans.

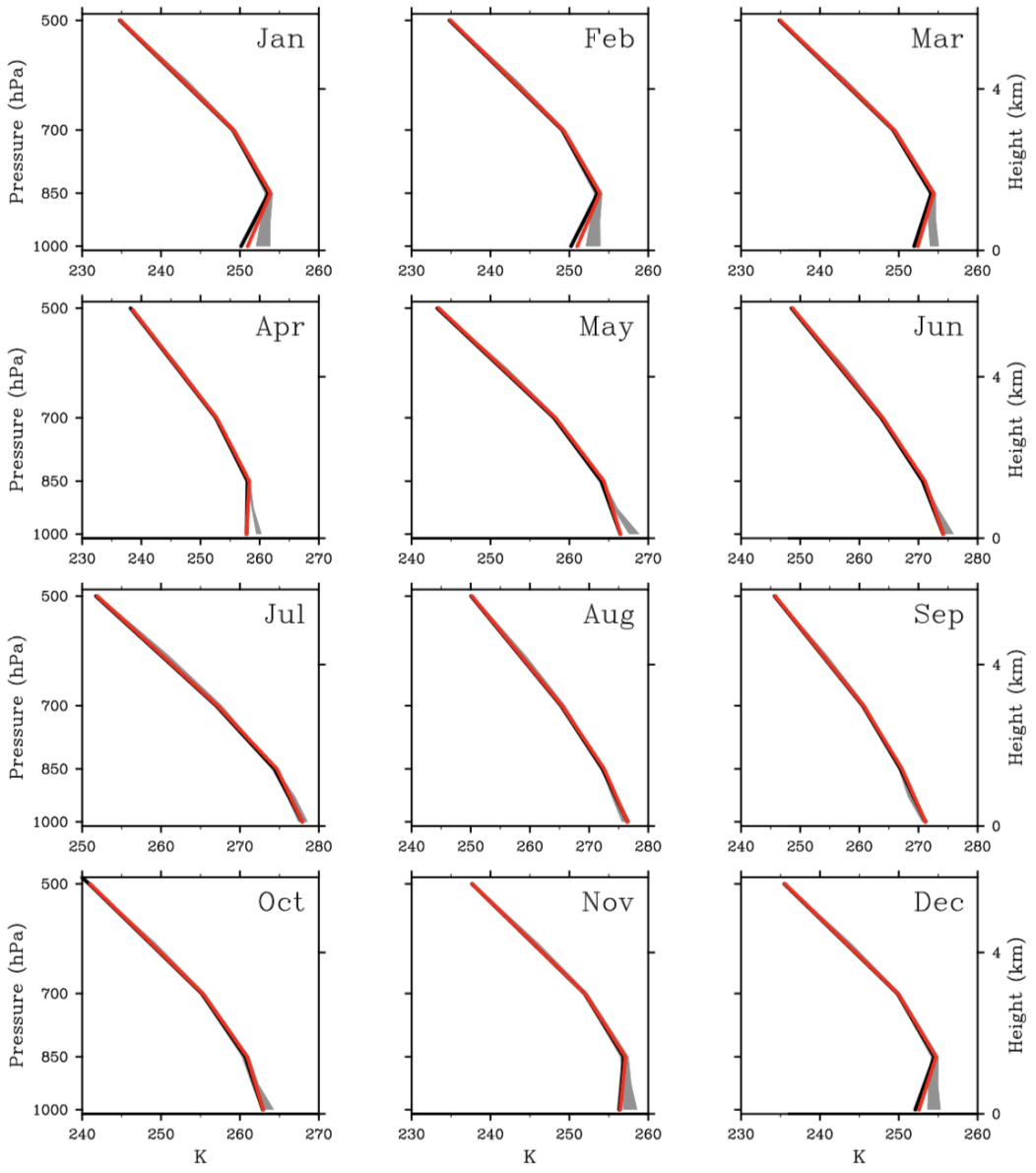


Figure 1.9: Comparison of monthly mean profiles of air temperature from radiosonde stations (red) and six reanalyses (gray) used by Serreze et al. (2012) including MERRA, CFSR, NCEP-I, ERA-40, ERA-I, and JRA-25 for the period 1979-2001. The gray shading shows the range in the air temperature between the six reanalyses based on data at the grid point closest to the radiosonde sites. Figure 3 from Serreze et al. (2012).

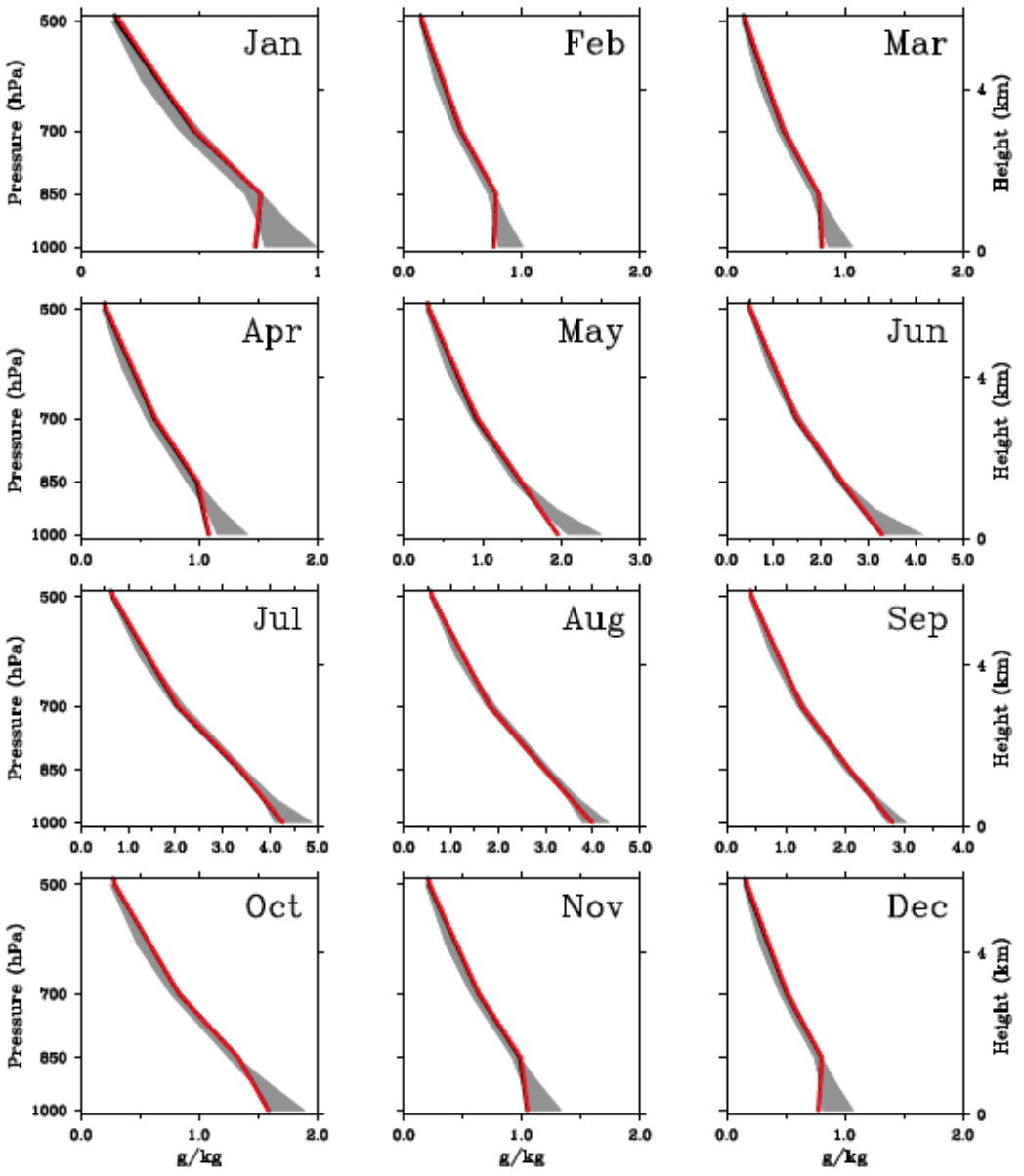


Figure 1.10: Comparison of monthly mean profiles of specific humidity from radiosonde stations (red) and six reanalyses (gray) used by Serreze et al. (2012) including MERRA, CFSR, NCEP-I, ERA-40, ERA-I, and JRA-25 for the period 1979-2001. The gray shading shows the range in the specific humidity between the six reanalyses based on data at the grid point closest to the radiosonde sites. Figure 3 from Serreze et al. (2012).

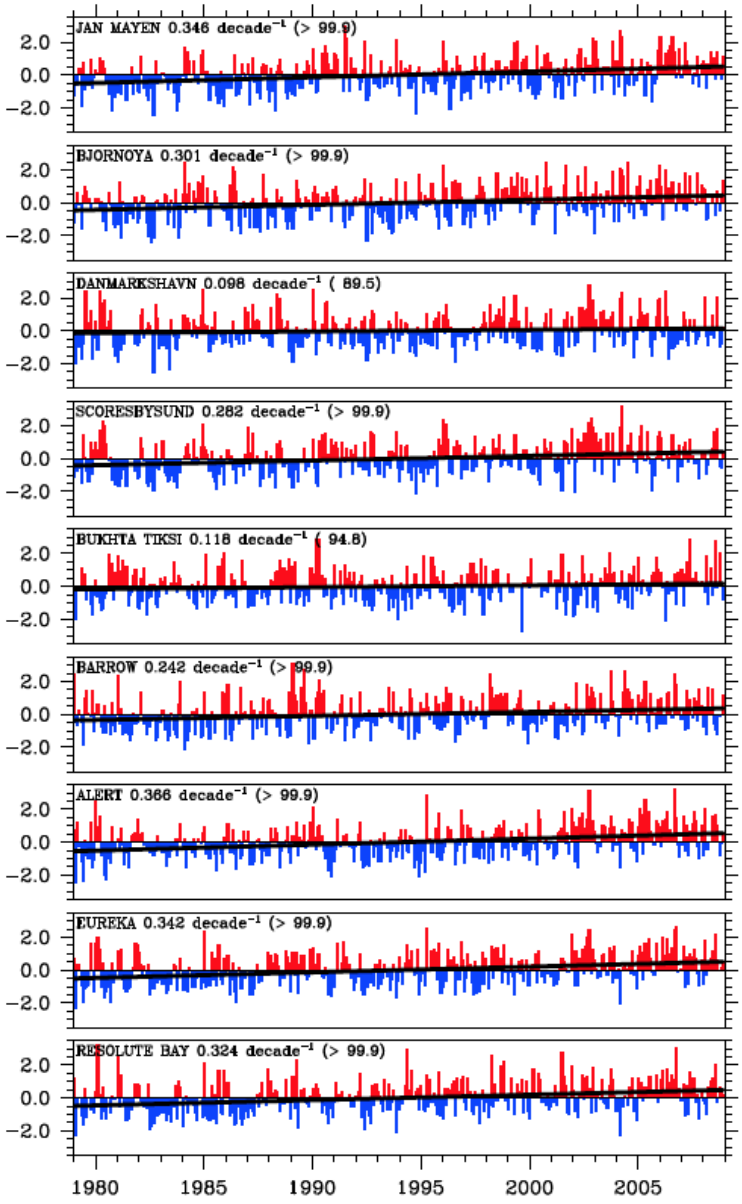


Figure 1.11: Time series from 1979-2010 of monthly standardized anomalies in surface to 500 hPa precipitable water at the nine radiosonde stations located in figure 1.15. A trend line is shown in black and confidence interval shown in parentheses Serreze et al. (2012).

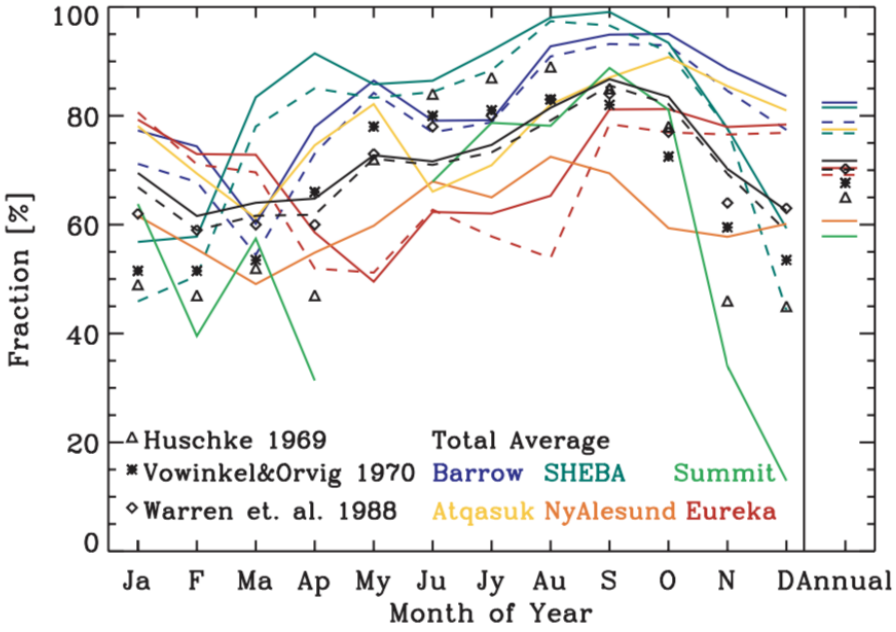


Figure 1.12: Annual cycle of monthly mean cloud occurrence fraction at six Arctic observatories (Barrow, SHEBA, Summit, Atqasuk, NyClesund, and Eureka), with the black curve denoting the average cloud fraction for all sites. Past Arctic cloud fraction climatologies are also provided from Huschke (1969), Vowinkel and Orvig (1970), and Warren et al. (1988). Figure from Shupe et al. (2011).

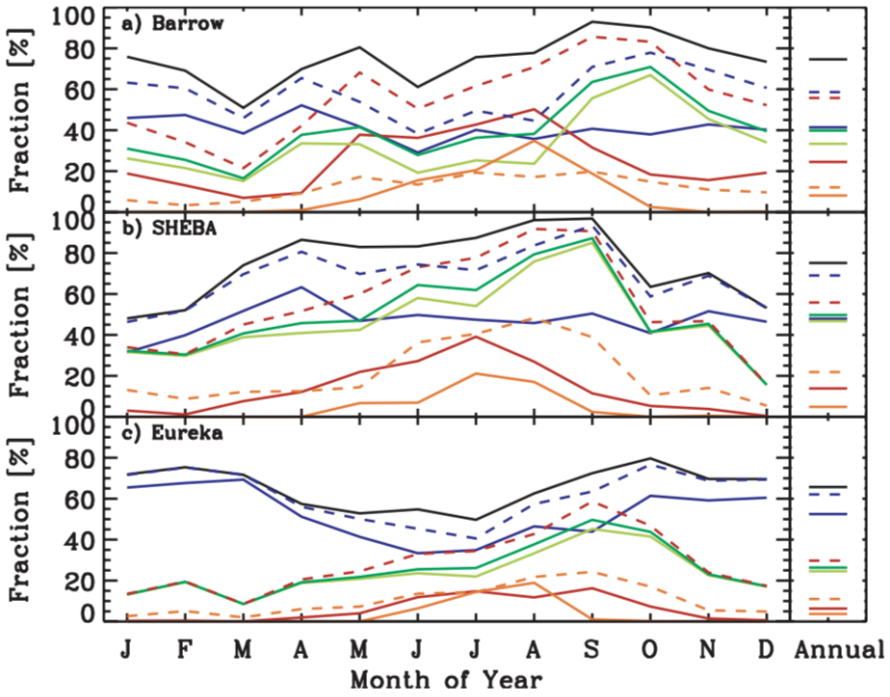


Figure 1.13: Annual cycles of monthly mean cloud occurrence fraction for different cloud types at (a) Barrow, (b) SHEBA, and (c) Eureka. Curves include the total cloud fraction (solid black), ice-only cloud fraction including snow (solid blue), liquid-only cloud fraction (solid red), liquid precipitation including drizzle and rain (solid orange), mixed-phase cloud fraction (solid light green), and mixed-phase column fraction (solid dark green). Dashed lines indicate the occurrence fractions for: ice in any type of cloud (dashed blue), liquid in any type of cloud (dashed red), and multiple, distinct layers of liquid water in any type of cloud (dashed orange). Figure from Shupe (2011).

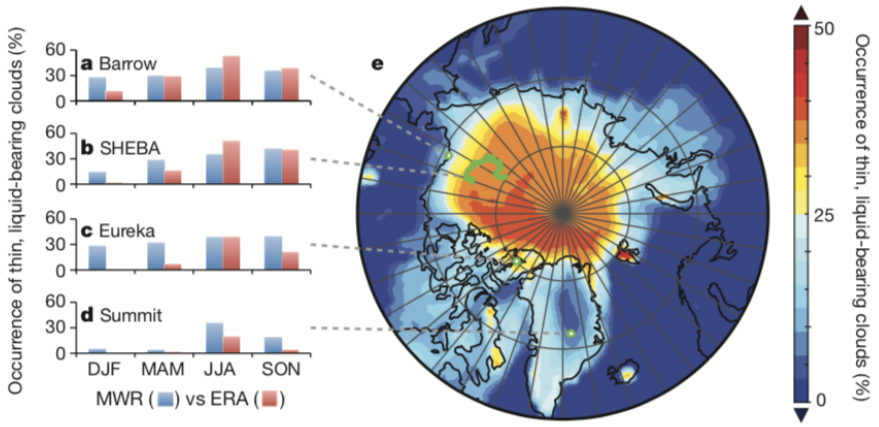


Figure 1.14: Figure from Bennartz et al. (2013) showing frequency of occurrence of thin, liquid-bearing clouds at various Arctic observatories. For the purpose of this plot, "thin, liquid-bearing" clouds are defined as clouds in the range of 10 g m^{-2} < LWP < 60 g m^{-2}, corresponding to the range of maximum enhanced cloud radiative forcing at the surface. (a–d) Comparisons of ground-based observed (blue, microwave radiometer (MWR)) and ERA-Interim simulated (red, ERA) frequencies of occurrence of these clouds for four Arctic observation sites for all seasons and (e) Circumpolar map of the frequency of occurrence of these clouds from 32 yr of ERA reanalysis (1979–2011). The plot in e is conditionally sampled to only include cases with solar zenith angle lower than 80° and a surface albedo higher than 0.5.

1.3.3 Properties of the Atmosphere Over Greenland

While the previous studies outlined in this chapter have provided beneficial information on Arctic thermodynamic and cloud characteristics, since the study at hand focuses on ground based observations from the summit of Greenland, it is important to note that this ice sheet is a unique feature of the Arctic. With its peak sitting at 3.25 kilometers above sea level, conditions are expected to differ somewhat from the general conclusions found for the Arctic region as a whole. For example, values of precipitable water remain low year-round at the summit of Greenland on average (Serreze et al. 2012; Shupe et al. 2013), relative to other Arctic locations (Figure 1.15), which may be an important factor in considering how TPVs evolve over it.

The Integrated Characterization of Energy, Clouds, Atmospheric State, and Precipitation at Summit (ICECAPS) project, funded by the National Science Foundation, is an observing system at Summit, Greenland which has helped build a better understanding of the atmosphere over Greenland since 2010 (Shupe et al. 2013) (see section 2.1.3 for more information). Active and passive sensors at Summit, combined with models, help us to assess the environment at high resolutions and study the surface heat budget at Summit. A first look at some of the atmospheric state properties over Greenland is discussed in Shupe et al. (2013), who use the first 20 months of data to analyze various cloud and thermodynamic properties at Summit. Due to the high altitude of Summit, specific humidity remains low year-round (as shown in Figure 1.15), with ICECAPS data showing near-surface maximum values around 2 g kg^{-1} in summer months. Temperature and moisture inversions are found consistently in soundings from Summit, with at least one surface-based temperature inversion occurring in all but one of the soundings during the first 20 months. Inversions were also notably deeper and stronger during winter months, reaching strengths greater than 10° C and depths of about 200 m (Shupe et al. 2013). Moisture inversions generally occur about 87% of the time when temperature inversions are present, and 47% of the time when elevated inversions are present (Shupe et al. 2013). A variety of cloud structure properties

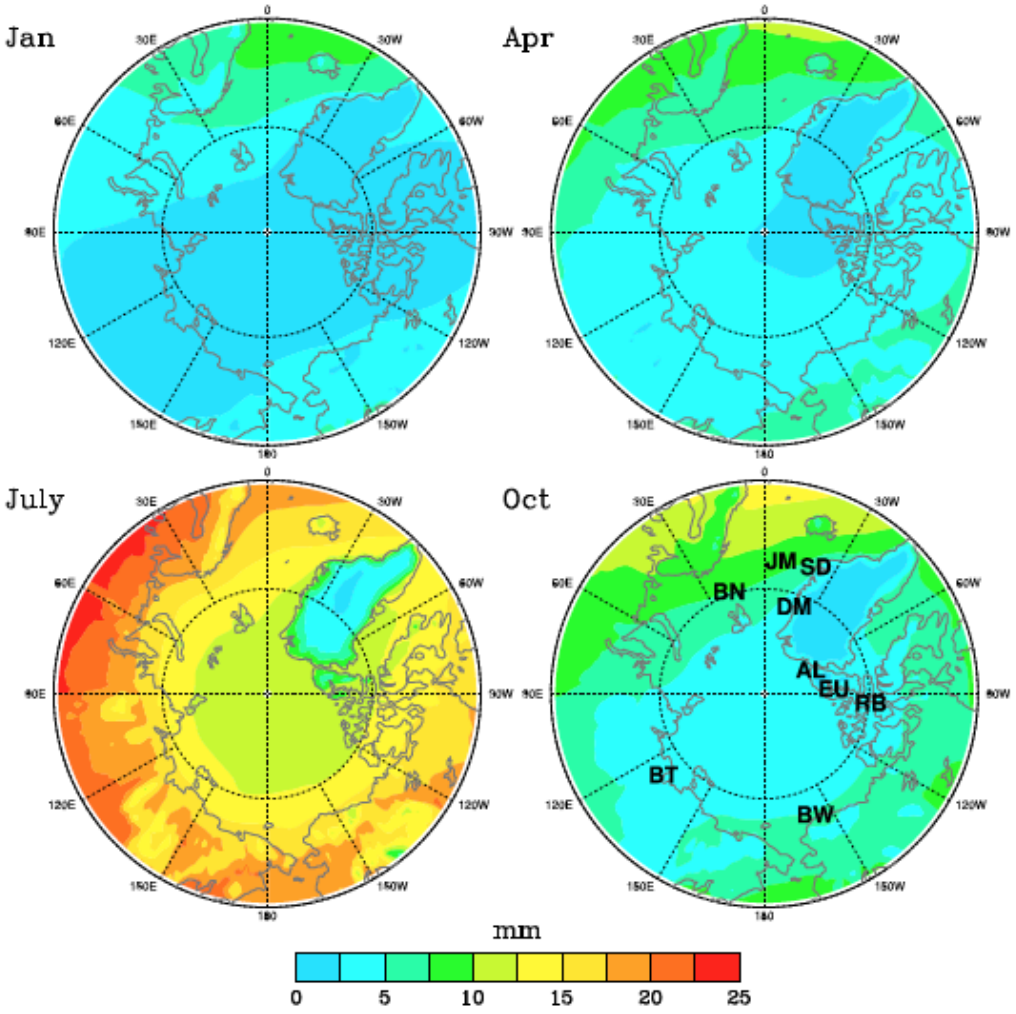


Figure 1.15: Annual mean surface to 500 hPa precipitable water for the region north of 60 N from the MERRA reanalysis for January (upper left), April (upper right), July (lower left), and October (lower right), based on data from 1979-2010. The October panel also shows the locations of the nine radiosonde sites that were included in the analysis done by Serreze et al. (2012)

above Summit are summarized in figure 1.16. Cloud cover over Summit reaches a maximum during the summer, with 85% cloud cover near the surface, and a minimum cloud cover is reached during late winter and early spring with total monthly fractions around 65%. The lowest cloud-base height tends to be lower in the summer and higher in winter, with the deepest clouds being present in summer months, consistent with seasonal changes in low-level static stability (Shupe et al. 2013). Liquid water in these clouds is shown to be present year-round ranging from 10% occurrence fraction in winter months to 40%-60% in summer months, consistent with other studies showing low-level, mixed-phase stratus clouds present in Arctic locations year-round (see figure 1.14).

Since Summit is located inland on the Greenland ice sheet, far removed from many surface sources of heat and moisture which make these low-level, mixed phase clouds so common around the Arctic, different processes are working to maintain these clouds. Morrison et al. (2011) describes the process responsible for the resilience and persistence of such stable mixed-phase stratus clouds in the Arctic. Contrary to what may be expected in the cold Arctic climate, mixed-phased clouds are often present and persistent due to a delicate balance between the effects of liquid water, radiation, and turbulence (Morrison et al. 2011). Since the vapor pressure of ice is lower than that of liquid water, one would expect ice crystals to grow at the expense of the evaporation of supercooled droplets (i.e. The Wegener – Bergeron–Findeisen (WBF) mechanism), making it unlikely for supercooled droplets and ice crystals to coexist for long periods of time. These mixed-phase clouds tend to have a structure containing supercooled liquid droplets near cloud top, which form in updrafts, and precipitating ice crystals below this liquid layer (Morrison et al. 2011). The cloud top radiative cooling from the liquid layer decreases static stability, drives turbulence within the cloud and often helps to maintain a temperature and moisture inversion above the cloud. The turbulence induces updrafts that can be strong enough for conditions to become supersaturated with respect to water, hence allowing the growth of both liquid droplets and

ice particles, creating a positive feedback mechanism for the maintenance of the mixed-phase clouds (Figure 1.17). Entrainment of moisture above the cloud top inversion also assists with their maintenance, a mechanism not commonly found in lower latitudes where cloud top entrainment is usually dominated by dry air (Morrison et al. 2011).

While Shupe et al. (2013) provide an overview of atmospheric properties at Summit, including notes regarding surface based inversions (SBIs) at Summit, Miller et al. (2013) makes use of radiosonde, microwave radiometer, and meteorological tower datasets available from ICECAPS to specifically characterize SBIs at Summit and the cloud scenes affecting them. The annual cycle of SBI occurrence and intensity from the three measurements shows a general agreement with previous studies (Figure 1.18), that is that SBIs are the most frequent and the most intense in the winter months, with frequencies reaching close to 100% in several winter months. This higher frequency in the winter is due to the cold, dry, sunless, and mostly cloudless atmosphere found more often in winter months over Greenland, allowing for strong radiative cooling at the surface (Miller et al. 2013). An important takeaway from Miller et al. (2013) is the relationship clouds have with SBIs over Greenland, which is that liquid-bearing clouds tend to weaken SBIs by radiatively warming the surface, while low precipitable water vapor and a clear-sky scene tend to allow the SBI to deepen and persist (Figure 1.19). The latter conclusion is in agreement with many early studies of SBIs and is consistent with the findings of Shupe et al. (2013). This becomes important when considering how a warming climate would lead to fewer SBIs over Greenland, affecting the surface energy balance.

An example of low-lying liquid-bearing clouds affecting the surface energy budget is the July 2012 enhancement of the Greenland ice melt, discussed by Bennartz et al. (2013). This study helped solidify the radiative impact of the ubiquitous low-lying mixed-phase clouds seen around the Arctic with direct evidence of their effects. During July of 2012, air temperatures at lower-elevation regions of the Greenland Ice Sheet were warm enough to induce melting, however surface air temperatures at Summit were not, leading to the

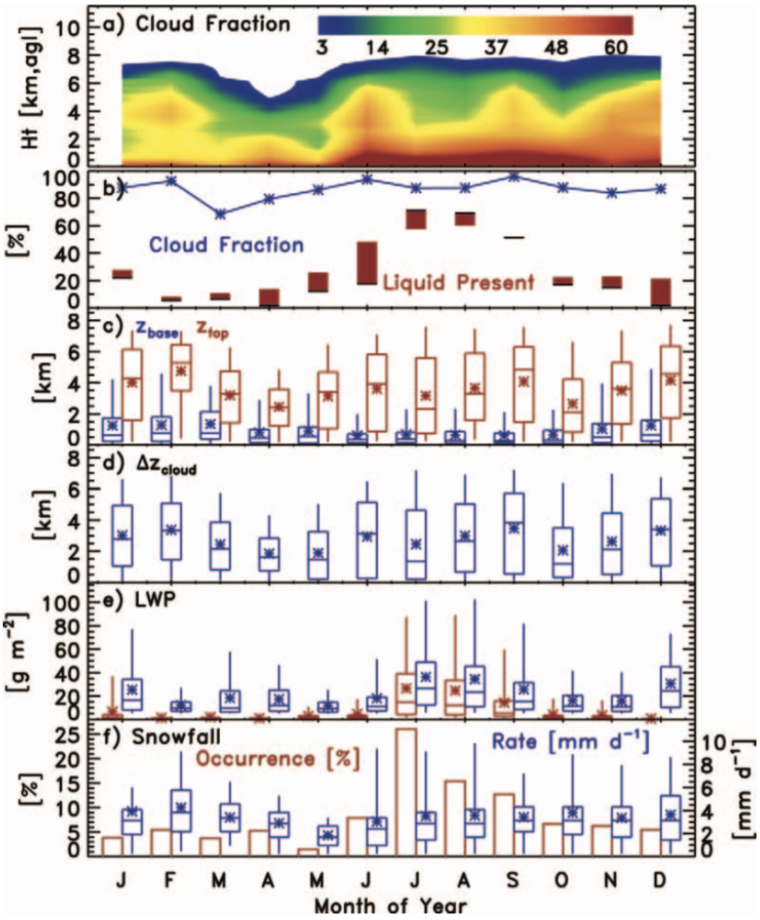


Figure 1.16: Monthly statistics of (a) cloud occurrence fraction as a function of height, (b) total cloud occurrence fraction in the vertical column (blue) and the occurrence fraction of liquid water (red), (c) low cloud-base (blue) and high cloud-top (red) heights when clouds are present, (d) maximum depth over which clouds occur (high top to low base, but not necessarily cloudy throughout), when clouds are present, (e) MWR-derived LWP in all conditions (red) and in those conditions identified as cloudy with a LWP > 5 g m^{-2} (blue), and (f) Precipitation occurrence sensor system - derived snowfall occurrence fraction (red) and liquid-equivalent snowfall rate when snow is occurring (blue). Box-and-whisker plots contain information on the 5th, 25th, 50th, 75th, and 95th percentiles and mean (symbol). Figure 13 from Shupe et al. (2013).

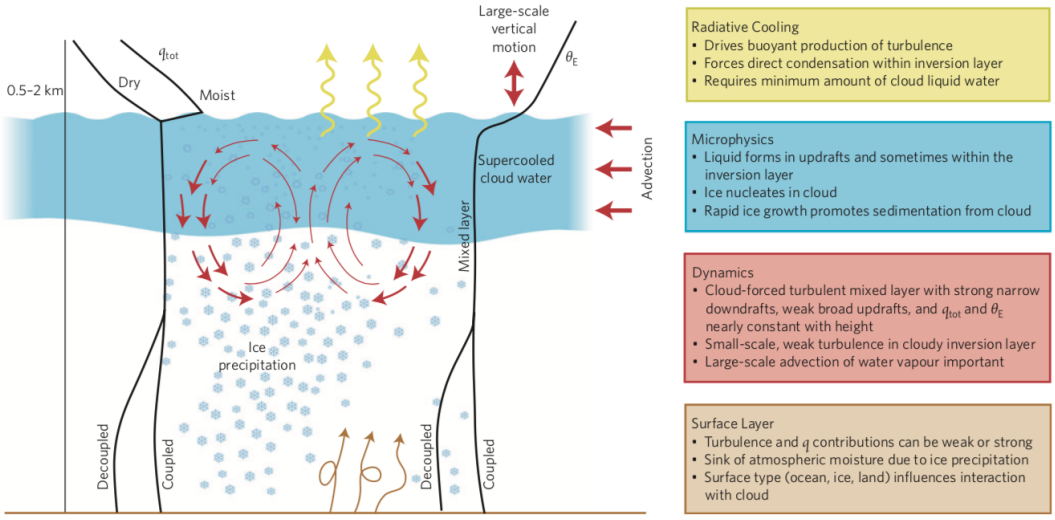


Figure 1.17: A conceptual model from Morrison et al. (2011) illustrating the physical processes involved in the maintenance of Arctic mixed-phase clouds.

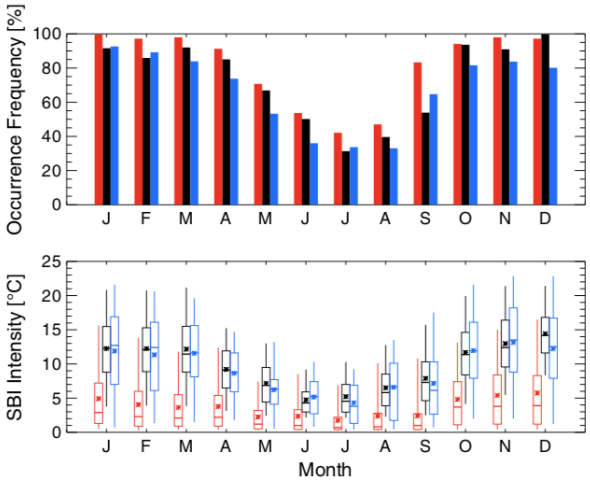


Figure 1.18: Fractional occurrence of surface-based inversion (top) and SBI intensity (bottom) derived from MWR (black), radiosonde (blue), and meteorological tower 10m - 2m temperature difference. In the bottom panel, the box indicates the 25th and 75th percentiles, the whiskers indicate the 5th and 95th percentiles, the middle line is the median, and the asterisk indicates the mean. Figure from Miller et al. (2013).

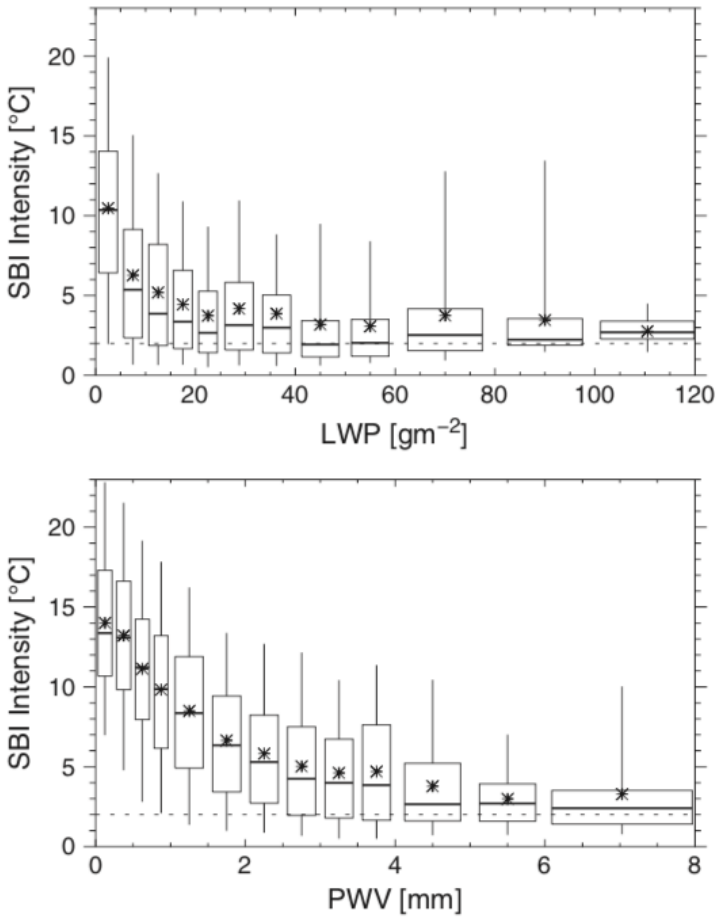


Figure 1.19: Surface-based inversion intensity as a function of the mean LWP (top) and mean PWV (bottom) over a 5 minute window surrounding the temperature retrieval from the MWR for cases between July 2010 and May 2012. The box indicates the 25th and 75th percentiles, the whiskers indicate the 5th and 95th percentiles, the horizontal line indicates the median, and the asterisk indicates the mean. Figure from Miller et al. (2013).

hypothesis that clouds must be responsible for the increased downwelling infrared radiation causing surface melt. Results from modeled radiative surface fluxes (model results for temperatures were validated against observations from meteorological tower and radiosonde data at Summit) involving clouds showed that the surface energy balance over Greenland is determined by the competing effects of clouds reflecting shortwave radiation,

hence reducing the warming at the surface, and clouds emitting infrared radiation back to the surface, acting to warm the surface (Bennartz et al. 2013). It was determined that there is a specific range of liquid water path values for which surface temperatures will rise above 0 °C and induce melting, that being 10 to 40 g m^{-2} (Figure 1.20). Within this range, the optical properties of the cloud allow for sufficient shortwave radiation to still reach the surface, while the longwave emission from the cloud is also strongly contributing to warming at the surface. It is important to note, however, that this study is specific to the Greenland Ice Sheet and therefore specific to a surface characterized by ice.

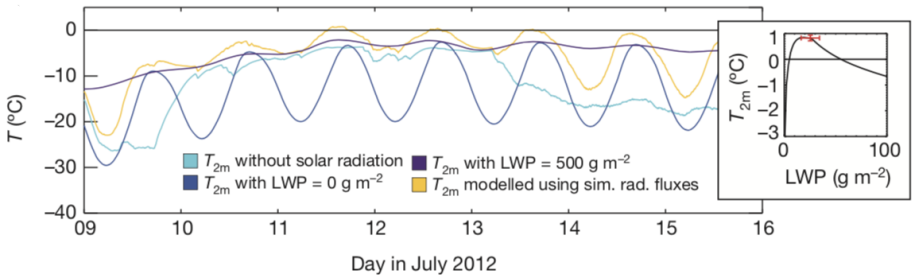


Figure 1.20: Model sensitivity studies with respect to clouds and solar radiation. The turquoise curve represents T_{2m} without solar radiation, the blue curve represents T_{2m} assuming a cloud-free atmosphere (LWP 50 g m^{-2}), the purple curve showing T_{2m} assuming an atmosphere with a very thick cloud with constant LWP of 500 g m^{-2}, and the yellow curve shows the development of T_{2m} simulated using the surface energy balance model driven by simulated radiative fluxes based on water vapor path (WVP) and liquid water path (LWP). The inset shows simulated maximum T_{2m} based on LWP corresponding to the time between days 11 and 12 where the modeled temperature reaches above 0 °C. The red data point shows the observed T_{2m} and LWP at a time of ± 30 min around the time of maximum surface temperature (error bars, ± 1 s.d.)

While radiation is an important component of the surface energy budget, radiative heating in the atmosphere can be an important component to the diabatic heating profile, which

can ultimately influence atmospheric circulations. Radiative heating rate (RHR) is defined as follows:

$$\mathrm{RHR}(z) = \frac{dT(z)}{dt} = \frac{g}{C_p}\left(\frac{\Delta F_{\mathrm{net}}}{\Delta p}\right)(z) \tag{1.7}$$

where T is temperature, t is time, p is pressure, g is the acceleration due to gravity, C_p is the specific heat capacity of air at constant pressure, and z is the vertical height coordinate. F_{net} is the net radiative flux in a layer, defined as the net upwelling minus the net downwelling flux, and Δp is the thickness of the layer in consideration. This equation states that RHR is defined by the change in the net radiative flux over the layer. For example, flux convergence (i.e. a positive net flux) causes an increase in the temperature of the layer. Shortwave and longwave RHR are combined to find the total RHR.

While RHR values can be measured using radiometers, use of such observations directly is not common. In order to acquire the upwelling and downwelling components of the radiative field, radiometers must be flown at two different levels simultaneously and have matching fields of view (e.g. Turner et al. (2018)), making precise and accurate measurements of RHR profiles difficult to obtain. Often times, RHR values are measured by radiometers at the surface and by satellites at the top of the atmosphere and profiles of RHR are calculated based on these measurements. While this method may be more commonly used, these derived profiles also come with sampling uncertainties resulting in large errors in the derived values. Since observed RHR values are not always reliable, the most common method for finding RHR profiles is by way of radiative transfer models. By using a radiative transfer model, high resolution vertical distributions of temperature, gaseous molecules, and clouds from models or observations can be used as input to obtain RHR profiles with greater accuracy. It is important to note, however, that the accuracy of these profiles is highly dependent on the accuracy of the cloud property retrievals used as a component of the input (e.g. Turner et al. (2018), Ebell et al. (2011)).

The most recent analyses have aimed to further characterize how cloud macro and microphysical properties affect the RHR values in the troposphere by investigating radiative heating rate profiles specific to Arctic locations. Turner et al. (2018) conduct an analysis of RHR profiles based on cloud observations over Barrow, Alaska, finding that results differed greatly based on cloud phase (specifically, LWP values) and cloud layers. For single-layer, liquid-bearing clouds, longwave cooling at cloud top dominates shortwave heating and the longwave radiative cooling rates at cloud top were 10-20 times the values for single-layer, ice-only clouds with the same total water path (Figures 1.21 and 1.22). A comparison of liquid-only to mixed-phase clouds in a single layer done in figure 1.22d shows that the liquid in mixed-phase clouds accounts for much of the cloud top cooling, implying that liquid is a major component of radiative effects induced by clouds. For LWP values greater than 10 g m^{-2}, LW and SW RHR values at cloud based combined to have an overall warming effect. This value supports the range of 10 to 40 g m^{-2} found by Bennartz et al. (2013) to induce warming at the surface. Additionally, when considering more than one cloud layer, Turner et al. (2018) found that the LW RHR in the lower cloud layer is modified by variations in LWP in the upper cloud layer due to the addition of downwelling LW radiation from the upper cloud layer (Figure 1.23). Because of this, higher values of LWP in the upper cloud layer induce warming between cloud layers relative to a clear-sky case. Since these analyses are not specific to Summit, direct comparisons cannot be made to RHR values over Summit with 100% certainty. The study, however, is an important step in understanding the radiative impact of clouds in the Arctic, and can likely be applied to Summit under the impression that similar cloud profiles exist in these two locations, as shown in previous sections. These determinations are an important factor in the consideration of TPV evolution, since it is hypothesized in literature that radiative cooling is a major contributor to TPV intensification. The presence of liquid or mixed-phase clouds over Summit, and the knowledge of the RHR profiles they induce, will help in our investigation of cloud profiles near TPVs.

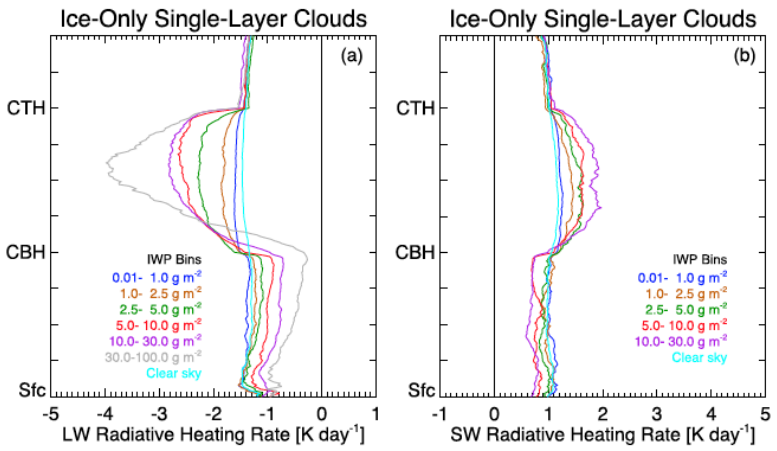


Figure 1.21: Normalized vertical distribution of the median longwave and shortwave RHR values for varying amounts of ice in a single-layer, ice-only cloud, with respect to cloud top height and cloud base height. Figure from Turner et al. (2018).

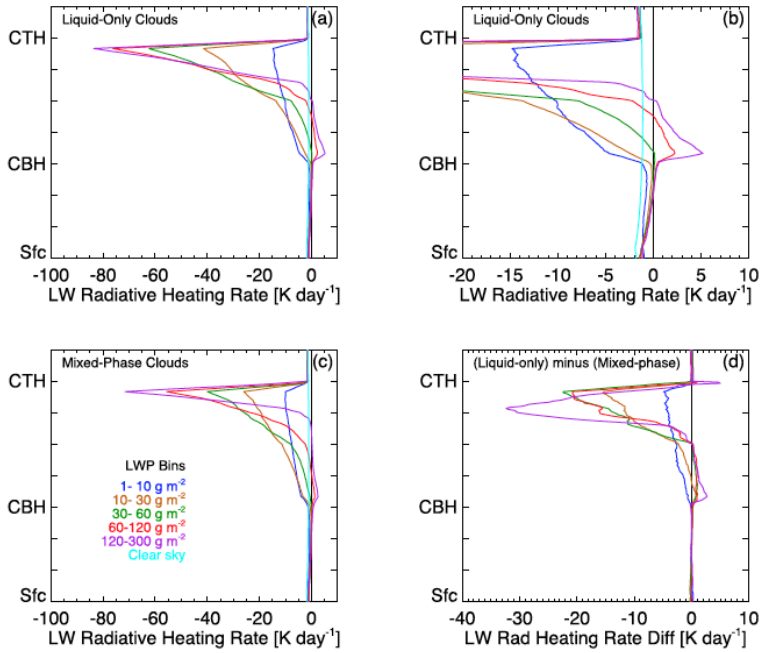


Figure 1.22: Normalized vertical distribution of the median longwave RHR values for varying amounts of liquid in a single-layer, liquid-bearing cloud, with respect to cloud top height and cloud base height. Panel b) shows a closer look at the small-scale changes in heating rates close to 0. Figure from Turner et al. (2018).

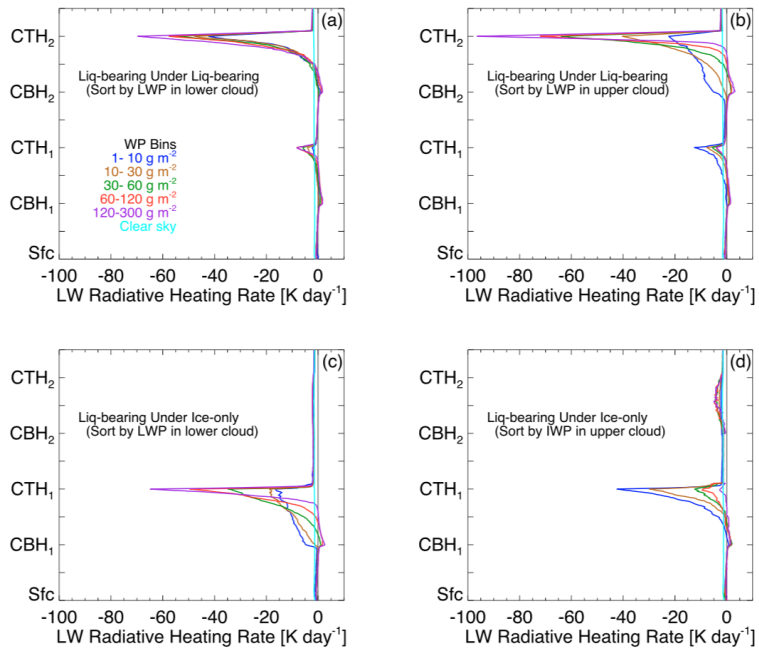


Figure 1.23: The normalized vertical distribution of the median LW RHR for two-layer clouds (a),(b) where both layers contain some liquid water, or (c),(d) where only the bottom layer contains liquid water and the upper layer is ice only. The profiles were normalized between Sfc, first cloud base (CBH1), first cloud top (CTH1), second cloud base (CBH2), and second cloud top (CTH2). Figure from Turner et al. (2018).

1.4 Motivation and Goals

As mentioned in section 1, tropopause polar vortices influence weather and other phenomena and have been studied extensively in the past decade via model simulations and climatological datasets. Much is known about TPV structure, radiative effects, and evolution based on these studies, and the need to know more about these unique features drives research in their genesis, effects on sea ice, and midlatitude interactions. Since most of what is known about TPVs comes from the analysis of models, observational studies are needed to support those findings. Since Cavallo and Hakim (2009) determined that synoptic patterns were not responsible for TPV intensity changes, an important missing piece

of this field of study thus far is the investigation of observations on a local scale to consider the characteristics of TPVs. One reason for this is the sparse nature of observations that are available in the Arctic and the lack of direct measurements of these dynamic features. Since these are based on the tropopause, observations are limited to radiosondes, which are particularly low temporal resolution for these (mostly) mesoscale features, and satellite. Data from Arctic observatories is becoming more readily available, especially since the implementation of the ICECAPS project (Integrated Characterization of Energy, Clouds, Atmospheric state, and Precipitation at Summit) at Summit Station, Greenland (Shupe et al. 2013), which takes continuous measurements of the atmosphere from ground-based instrumentation. Using these ground based instruments and a variety of retrieval methods, data at Summit is available dating back to 2010. These observations are a rich resource in probing the structure and cloud properties associated with a TPV as it moves over the observatory.

Through use of these high temporal resolution observations and data retrievals, one goal of the present study is verifying the composite structure presented in section 1.1.1. It is expected here that a TPV passing over Summit should exhibit characteristics similar to those shown figure 1.1, such as positive (negative) temperature anomalies above (below) the tropopause, positive (negative) moisture anomalies below (above) the tropopause, cyclonic winds, and positive EPV tendencies in the vortex center above the tropopause. Verifying composite structure through observations is of fundamental importance, since direct measurements of TPVs have not been investigated before. Additionally, the results from Cavallo and Hakim (2013) motivate us to consider how TPVs evolve based on clear-sky conditions and various cloud types in their vicinity. Their results suggest that water vapor gradients induced by a TPV led to intensification of the TPV, and that cloud-top cooling was a significant factor aiding in rapid intensification. These results guide us in the primary hypothesis for this thesis:

Cloud top cooling will more likely lead to TPV intensification, especially in the case of liquid or mixed-phase clouds extending to the tropopause, and clear-sky water vapor gradients will also lead to intensification due to increased radiative cooling in the TPV's core.

Chapter 2

Data and Methodology

2.1 Data

A variety of datasets have been exploited during the course of this project to analyze TPVs over Greenland. These datasets include ERA5, TPV tracks containing location and amplitude, and multiple ground-based instruments measuring atmospheric state located at Summit Station, Greenland. Each of these datasets are described in further detail in sections 2.1.1, 2.1.2, and 2.1.3, respectively. Together, these data allow for a deeper look at the characteristics of TPVs and their surrounding environment.

2.1.1 ERA5 Data and Usage

ERA5 ("ECMWF ReAnalysis") is an atmospheric reanalysis dataset developed by the European Centre for Medium-Range Weather Forecasts (ECMWF) that is available to the public. ERA5 is the fifth major global reanalysis developed by ECMWF, and covers the period from 1950 to present. By combining historical observations with the latest numerical modeling and data assimilation techniques, ERA5 provides hourly estimates of many atmospheric and oceanic variables, succeding the ERA-Interim 6-hourly atmospheric reanalyses. For this study, five-day periods of hourly temperature, specific humidity, and v-wind vertical profiles are used as base atmospheric state parameters, geopotential height and potential temperature of the 2 PVU surface (i.e. the dynamic tropopause), and relative vorticity for calculations of EPV. All ERA5 data is acquired from ECMWF using Meteorological Archival and Retrieval System (MARS) in batch form based on the date of each TPV's closest point to Summit. From the date on which the TPV passes Summit, data is acquired for the two days before and the two days after. Model output comes from the operational, high-resolution (31 km), deterministic analysis (i.e. , and are retrieved either

using 37 standard pressure levels for vertical profile variables or the PV level at 2 PVU for variables that are desired on the dynamic tropopause. The ERA5 high resolution data has a native resolution of 0.28125 degrees, which is the equivalent of about 31 kilometers at the equator and about 9.3 kilometers at the latitude of Summit.

Soundings from Summit Station have been assimilated into ERA5 since January 2012, making ERA5 an appropriate reanalysis dataset to use for high temporal resolution atmospheric state parameters over Greenland. Since Summit Station is located at 72.6°N, 38.5°W, atmospheric profile data is downloaded in a grid box extending from 71°N to 74°N and from 40°W to 36°W at 0.25x0.25 grid spacing. Since the format of ERA5 data is preliminary GRIB1 before conversion, only three decimal places are supported. For this reason, a resolution of 0.25x0.25 is specified to approximate the irregular grid spacing onto the native Gaussian grid on which the data is archived). From each downloaded NetCDF file, the atmospheric state data at the point closest to the location of Summit is extracted and used in the analysis. For the datasets based on the dynamic tropopause, the resolution remained 0.25x.025, however the grid box was larger, extending from 60°N to 85° and 20°W to 60°W. This larger grid box was for the purpose of creating animated maps showing hourly potential temperature on the tropopause over much of Greenland as an alternative method for viewing TPVs and comparing their shapes and locations to the tracker (more in section 2.1.2). From these datasets, the geopotential height of the surface was extracted for the point nearest Summit in order to include tropopause height estimates in the time-height cross section figures created for our analysis (see Chapter 3).

Full documentation for ERA5 can be found at `https://confluence.ecmwf.int/display/CKB/ERA5+data+documentation`.

2.1.2 TPV Tracks

TPV tracks are used in the analysis to visualize how a TPV evolves in shape, size, and strength as it approaches and crosses over the ground-based instruments at Summit. These

tracks are acquired through TPVTrack v1.0, an open-source software package created by Nicholas Szapiro and Steven Cavallo at The University of Oklahoma (Szapiro and Cavallo 2018, in review). TPVTrack is an objective tracking algorithm which was specifically created to automate tracking and characterization of TPVs, based on methodology from various existing approaches. The goals of the tracker include representing the spatial structure of TPVs and representing time evolution including merging and splitting events. The former is achieved by using restricted regional watershed basins which are defined by the surrounding basin that drains by steepest descent to a potential temperature minimum. Then, by using the sign of the local relative vorticity of each cell in the basin, these basins can be segmented into cyclonic and anticyclonic TPVs. A user-defined bounding contour is implemented to further restrict each basin and improve isolation of the anomalies. The bounding contours for this study were restricted to the 10th percentile of boundary amplitudes. The latter, representing time evolution of TPVs, is done by using an overlap correspondence method dominated by advection. Correspondences are classified by advecting a single basin half a time step forward, and another basin half a time step backwards, and comparing the relative overlap in the advected basins. The correspondence type (e.g. form, decay, split, merge, persist) can then be categorized into a major or minor correspondence, where a major correspondence represents the case in which both advected basins are the most similar to only the other and no other basins at the advected time steps. Full tracks are then determined by connecting all major correspondences, and when no major correspondence exists before or after, the track is considered to begin or end, respectively.

The tracker has been used most extensively with ERA-Interim 6-hourly data over the Northern Hemisphere, north of any user-specified latitude, but for this study the tracker uses ERA5 hourly data north of 30°N for the years 2012 through 2014. 30°N was chosen to reduce the dataset for which to run the tracker over, and the years were chosen due to data quality and data availability at Summit. Meteorological inputs to the tracker are zonal wind, meridional wind, relative vertical vorticity, and potential temperature on the

tropopause. Once tracks are formed, tracks were then filtered for specific use in this project. The first filter applied restricted vortices to at least a two-day lifetime, a TPV requirement, providing 11,765 TPVs. The second task was to apply a spatial filter, since the interest of the study is restricted to the single point location of Summit Station. By restricting tracks to TPVs that passed within 100 km of Summit at their closest point, the number of TPVs was reduced to 93. However, after some investigation, it was found that many of the TPVs in the reduced dataset were small enough that even the 100 kilometer distance restriction was not close enough for their presence to be measured at Summit. With this in mind, the distance restriction was reduced to 40 km from Summit at each TPV's closest point, which provided a dataset of 40 TPVs.

2.1.3 Instrumentation at Summit Station, Greenland

The Integrated Characterization of Energy, Clouds, Atmospheric State, and Precipitation at Summit (ICECAPS) Project has been part of an ongoing effort to characterize cloud and atmospheric state properties in the Arctic. This project, funded by the National Science Foundation, was put in place in 2010 and provides a rich resource for probing the atmosphere above the 3,250 meter high Greenland Ice Sheet. Instrumentation at Summit Station is modeled after other Arctic observatories such as the Atmospheric Radiation Measurement site at Barrow, Alaska and the NOAA-Canadian Network for Detection of Atmospheric Change (CANDAC) in Eureka, Canada (Shupe et al. 2013). A large number of instruments are present at Summit Station, including passive instruments such as a Humidity and Temperature Profiler (HATPRO), a microwave radiometer (MWR) and a Polar Atmospheric Emitted Radiance Interferometer (P-AERI). These instruments all provide 5-minute (or higher) temporal resolution atmospheric thermodynamic profiles in the boundary layer. Twice-daily soundings are also launched and this data is uploaded to the Global Telecommunication System (GTS), a system of global telecommunication facilities

that arranges the collection and distribution of weather observations run by the World Meteorological Organization. Cloud properties are measured by instruments such as a Polarization Sensitive MicroPulse Lidar (MPL), a Cloud Aerosol Polarization and Backscatter Lidar (CAPABL), a 35-GHz Millimeter Cloud Radar (MMCR), a ceilometer, and a Sodar. Additionally, a Precipitation Occurrence Sensor System (POSS), and an ice particle imaging camera (IcePIC) are available to characterize ice precipitation. Table 2.1 provides more information on the specifications and parameters derived from each of these instruments. Raw measurements can be viewed via the daily updated quick looks browser at `https://www.esrl.noaa.gov/psd/arctic/observatories/summit/browser/`.

Table 2.1: Table detailing specifications, measurements, and derived parameters for instruments at Summit Station. Original table from Shupe et al. (2013).

Instrument name	Key specifications	Primary measurements	Derived parameters	Institution
P-AERI	530-3,000 cm^{-1} (3 - 19 μm), 1 cm^{-1} res., < 1-min time res.	Downwelling spectral infrared radiance	Cloud phase and microphysics, atmospheric temperature	Washington State University
MWRHF	Frequencies: 90, 150 gHz, 2–4 s time res.	Downwelling brightness temperatures	Cloud LWP, PWV	University of Wisconsin - Madison
HATPRO	Frequencies: 7 channels 22–32 gHz, 7 channels 51–58 gHz, 2–4-s time res.	Downwelling brightness temperatures	Cloud LWP, PWV, atmospheric temperature	University of Wisconsin - Madison
MMCR	Ka band (35 gHz), 8-mm wavelength, 2-s time res., 45-m vertical res.	Reflectivity, mean doppler velocity, doppler spectrum width, doppler spectra	Cloud boundaries, phase, microphysics; cloud-scale dynamics	NOAA Earth System Research Laboratory (ESRL)
MPL	532-nm wavelength, 5-s time res., 15-m vertical res., 2°–4° off zenith	Relative backscatter, hybrid linear–circular depolarization ratio	Cloud-base height, phase, microphysics	DOE ARM
CAPABL	523-nm wavelength, 15-s time res., 30-m vertical res., three-channel receiver, 2°–11° off zenith	Backscatter, linear depolarization ratio, diattenuation	Cloud-base height, phase, microphysics	NOAA/ESRL
Ceilometer	905-nm wavelength, 15-m vertical res., 15-s time res	Backscatter	Cloud-base height	DOE ARM
POSS	X-band (10.5 gHz), 1-min time res., single volume near surface	Reflectivity, doppler spectra	Precipitation rate	Environment Canada
Sodar	2,100 Hz, <1-m vertical res., 1-s time res.	Reflectivity	Boundary layer depth	NOAA/ESRL
IcePIC	Canon d50 dSLr, ~5.6 magnification, 1.5 μm res., 6.1 megapixels	Digital photographs	Ice crystal habit	Washington State University
Radiosondes	1-s time res., twice daily, RS-92K or RS-92SGP sondes	Temperature, relative humidity, pressure, winds	Cloud temperature, tropospheric thermodynamic structure	Summit Station (as part of ICECAPS)

2.1.4 Shupe-Turner Algorithm

The Shupe-Turner (ST) retrieval algorithm is a technique for synthesizing measurements from ground-based remote sensors into cloud properties that can be used to understand radiative fluxes along with a range of other applications. This retrieval algorithm was initially evaluated using a 2-year observational microphysics dataset from Barrow, Alaska. The algorithm is specific to Arctic observatories, making it unique from many cloud property retrieval systems in the past (Shupe et al. 2015). The algorithm relies on the strengths of various instruments working together in concert to fill in missing pieces of the cloud-property puzzle, with the largest contributions coming from the MMCR, MPL, AERI, MWR, ceilometer, and radiosondes. Each instrument has its weaknesses, for example, the MPL is attenuated very easily in the vertical, especially by optically thick clouds and liquid layers. For this reason, it is important to include observations from the MMCR which is not attenuated as easily and provides a better estimate of cloud top height (Shupe et al. 2015). A simplified overview of the ST retrieval process is shown in figure 2.1 and will be described here, as the results from this algorithm are important input for the the Rapid Radiative Transfer Model discussed in section 2.2.2.

The first necessity in the cloud retrieval process is the use of available observations to determine atmospheric state, including temperature and moisture profiles. This is done by starting with a MWR retrieval (MWRRET, which is described in Turner et al. 2007) which provides an initial measurement of liquid water path (LWP) and precipitable water vapor (PWV) from the MWR combined with radiosonde and surface measurements. To improve the temporal resolution of the atmospheric state variables, sounding variables are interpolated between the 12-hourly launches using the European Centre for Medium-Range Weather Forecasts operational model as guidance. This interpolation assists with gaps between soundings and above sounding heights. LWP retrieval accuracy is further improved using another retrieval algorithm, the Mixed-Phase Cloud Retrieval Algorithm (MIXCRA,

described in (Turner 2007)). MIXCRA combines MWR and AERI data to refine LWP estimates, especially for LWP values less than 50 g m^{-2} (Turner 2007). By combining various LWP retrieval techniques, LWP is more accurately and more consistently measured over the entire range of LWP.

Cloud-type classification is an important next step in the algorithm, because the accurate retrieval of microphysics properties is dependent on the correct cloud-type classification. The cloud-type is determined from radar, lidar, and ceilometer measurements and can include ice, liquid, or mixed-phase clouds, as well as precipitation types such as drizzle, rain, or snow (Shupe et al. 2015). Classifications are based on single time-height pixels that are 1 minute by 50-100 meters and the types of hydrometeors that exist in each pixel. Based on the strengths and weaknesses of different instruments and measurement techniques, retrieval methods are specific to different cloud scenes. The vertical distribution of cloud types determined from the cloud-type classification step is then used to apply a scene classification. This scene classification is a deterministic step in which retrieval conditions are applied based on the cloud type.

The final step in the algorithm is applying the specific retrieval based on the cloud scene classification. These retrievals include ice water content (IWC), ice water path (IWP) (the vertically integrated IWC), ice particle effective radius, liquid water content (LWC), and liquid particle effective radius. The cloud ice properties are highly dependent on the returns from the MMCR due to the instrument's sensitivity to large particles, and the retrievals cannot be acquired without the availability of this radar data. The uncertainty associated with ice particle retrievals can be up to 46% for the particle size and a factor of 2 for IWC. Retrieving cloud liquid is not as straightforward as retrieving cloud ice. Since LWP is generally very well measured by the MWR and AERI, this provides a helpful constraint on determining the vertical distribution of liquid to achieve a result for LWC. Radar, lidar, and radiosonde thermodynamic profiles are all used in determining the LWC throughout the profile. While LWP is generally very well measured by MIXCRA (uncertainties of

less than 5 g m^{-2} (Turner 2005)), derived LWC values at a given height can have a higher relative uncertainty, depending on the conditions. Alternatively, liquid particle effective radius is easily retrieved in optically thin clouds, with a retrieval bias of less than 1 μm when compared to in situ aircraft observations (Turner 2007). For optically thick clouds with no large hydrometeors present, liquid effective radius retrievals have uncertainties up to 32% (Shupe et al. 2015). For optically thick clouds where large hydrometeors are present, liquid effective radius cannot be easily derived and a climatological value of 8 μm is assigned based on previous studies of Arctic cloud particle sizes for liquid (Shupe et al. 2015).

Uncertainty of this technique as a whole has not been determined, since it is not clear how the uncertainties of the individual retrievals would aggregate. Despite this fact, the radiative closure study in Shupe et al. (2015) demonstrated that the retrieved cloud properties do provide good agreement with the surface radiative flux observations, which is a necessary step in the validation of these techniques. More details, example results, and evaluation of the ST retrieval are available in Shupe et al. (2015).

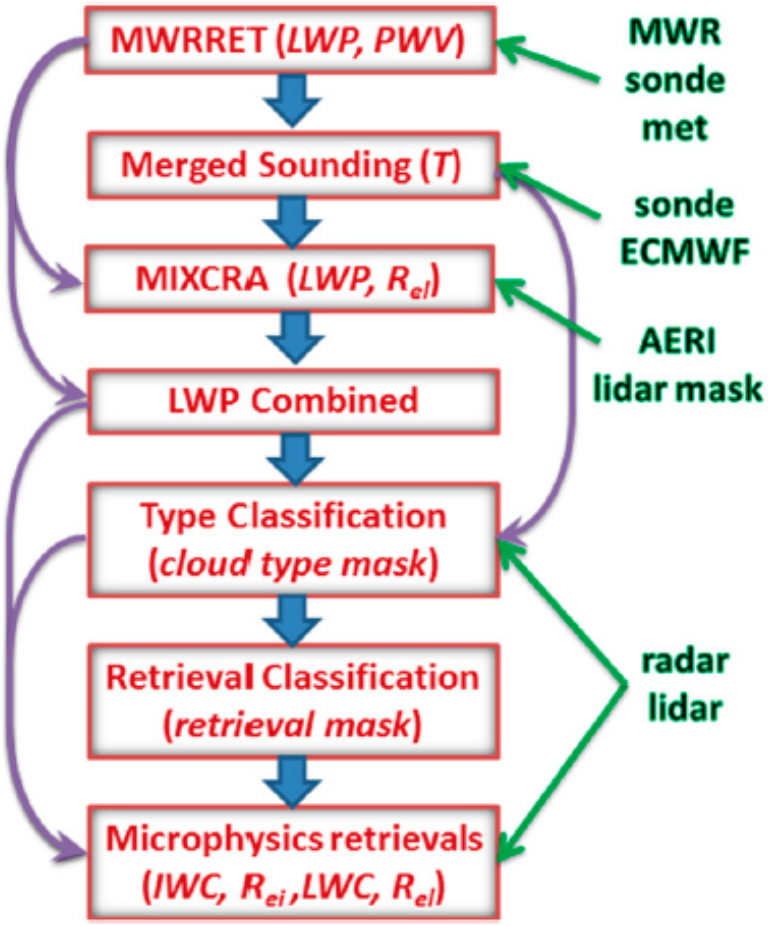


Figure 2.1: The Shupe-Turner microphysics retrieval flowchart showing input measurement streams in green and individual algorithm elements in red boxes. (Shupe et al. 2015)

2.2 Methods

2.2.1 Verification of Composite Structure

Data from ERA5 are plotted as time-height cross sections to compare the composite structure of the 40 TPVs observed over Summit with the composite structure derived from model simulations that was shown in section 1.1.1. Temperature, mixing ratio, v-wind, and Ertel potential vorticity (EPV) time-height cross sections are created by plotting 24-hour periods of each variable centered on the hour of the TPV's closest point to Summit. The height axis

in these figures and all others presented in this study is in terms of kilometers above ground level, rather than with respect to sea level. The time axis for these plots is in hourly increments, and height above ground level is found by using the hypsometric equation to convert the standard pressure levels from ERA5 to height levels at each time step. Temperature is plotted in Kelvin, while water vapor mixing ratio is plotted in terms of the log of the mixing ratio since water vapor decreases exponentially with height at saturation. In addition to the raw data plots, anomaly plots are created for each case. Standardized anomalies are defined here as the difference from the mean value in each vertical layer, divided by the standard deviation of the values in that layer. Composites of each variable were made based on all 40 cases to compare to the composite structure described in Cavallo and Hakim (2010). The composites are based on time from the TPV's closest point to Summit and the anomalies relative to this time (i.e. $\pm$3 hours from closest passage).

Using the TPV tracks described in 2.1.2, basins representing TPVs are plotted in 3-hour increments for $\pm$ 6 hours from the TPV's closest passage and color-filled based on their amplitude at each time step. These maps are beneficial when trying to consider how the TPV may be influencing the environment at Summit.

2.2.2 Rapid Radiative Transfer Model

Developed by Atmospheric and Environmental Research, the Rapid Radiative Transfer Model is a highly accurate and efficient radiative transfer model which uses the correlated-k approach to calculate fluxes and heating rates. This model can run within a general circulation model (RRTMG) or as a stand-alone model (RRTM). The stand-alone version is used in this study. The RRTM offers a great amount of flexibility and speed, with a variety of input options. Shortwave (SW) and longwave (LW) versions are available, both with different inputs required and outputs provided, however the LW version has the most importance in this study. The LW RRTM features fluxes and cooling rates which can be calculated over sixteen contiguous bands in the longwave (10-3250 cm^{-1}), however for simplicity the

entire LW spectrum is considered. Fluxes and heating rates from the LW RRTM have been compared to a line-by-line radiative transfer model (LBLRTM) which has been validated by observations at ARM climate research facilities, and and RRTM outputs agree with the LBLRTM outputs within 1.5 W m^{-2} for fluxes at all levels and 0.1 K day^{-1} for heating rates in the troposphere (Clough et al. 2005). The SW RRTM has similar features, such as calculation of heating rates for fourteen bands in the shortwave (820-50000 cm^{-1}) and 1 W m^{-2} direct irradiance agreement with the LBLRTM (Clough et al. 2005).

Emissivity, surface reflectivity, and values of many molecular species are taken as the default climatological values for a subarctic winter model, unless otherwise defined. For our study, water vapor mixing ratio is the only molecular species that is specified by our data rather than the subarctic winter climatology value. Variables that are required inputs for the RRTM for all cases include the user-defined layers at which to evaluate heating rates, pressure, and temperature of each level of data.

Heating rates are calculated by the RRTM for a single atmospheric profile for a single time. In order to get a larger time period of heating rates, for example, it is necessary to run the RRTM on a loop through the atmospheric profiles of temperature, water vapor, pressure, and cloud properties for each time step in the time period. The details of this process for clear-sky and all-sky cases are described in the following sections.

2.2.2.1 Clear-Sky

Clear-sky cases are those run without the inclusion of cloud properties. While clouds exist in many cases, a clear-sky run characterizes the background heating rates from temperature and water vapor. The model levels are defined prior to any RRTM runs and remain the same in every time step. The model levels start at 0 kilometers above ground level and extend to 75 kilometers above ground level, however resolution is higher in the lowest 10 kilometers. From 0 to 10 kilometers, model levels are set up in 90 meter increments. This number was chosen to complement the microphysics data, since the bin sizes for the

Shupe-Turner microphysics product are 45 meters by 1 minute. Above 10 kilometers, high vertical resolution becomes less important, but these upper levels remained necessary for the inclusion of the radiative effect of other gases such as ozone. Layer thicknesses above 10 kilometers increase by 20% up to 75 kilometers.

After the model levels are defined, atmospheric state data from ERA5 is read in and pre-processed for the RRTM. Relative vorticity downloaded from ERA5 needs to be converted to absolute vorticity for use in later analysis, and tropopause height needs to be calculated from geopotential height of the 2 PVU surface to add to all time-height figures. Absolute vorticity is found using the following:

$$\zeta_a = \zeta + 2\Omega \sin\theta \tag{2.1}$$

where Ω is the angular speed of the earth ($7.27x10^{-5}$ radians per second) and θ is the latitude (72.6°N). Tropopause height, in kilometers above ground level, is calculated using the following:

$$z = \frac{\phi}{g * 1000m} - 3.255 \tag{2.2}$$

where here, ϕ represents the geopotential in $m^2\ s^{-2}$, and g represents the acceleration due to gravity (9.8 m s^{-2}). Since data downloaded from ERA5 comes in terms of standard pressure levels, the hypsometric equation (shown below) is applied at each hourly time step to get height values from the pressure and temperature fields.

$$z_2 = \frac{R_d \overline{T_v}}{g} ln(\frac{p_1}{p_2}) + z_1 \tag{2.3}$$

Where R_d = 287 J K^{-1} kg^{-1} is the dry air gas constant, $\overline{T_v}$ is the mean virtual temperature in the layer, g is the acceleration due to gravity, and p_1 and p_2 are the pressures of adjacent layers at heights z_1 and z_2, with p_1 and z_1 representing the lower of the two layers. For clear-sky cases, the time range for the analysis is a 5-day period taken at hourly increments. Another intricacy of working with data at Summit is the altitude at which Summit sits.

Since data comes from ERA5 in terms of pressure levels, which start at 1000 hPa, many of these levels are null at Summit since standard surface pressure wavers around 650 hPa, as observed by the met station at Summit. For this reason, when using equation 2.3, 3.255 km is subtracted off of each height value after they are calculated, which gives negative values for all levels below the surface. This allows us to retain only the data corresponding to positive height values in all appropriate datasets (e.g. temperature, water vapor, vorticity). The next step is then to interpolate variables at the calculated height values to the model levels specified for the RRTM. In addition, since the RRTM requires pressure levels for each temperature and water vapor level, the inverse hypsometric equation is then used to convert the RRTM model levels (which are in terms of kilometers above ground level) to the associated pressure levels, since the ERA5 data has been converted to heights matching the RRTM model levels. After doing this, new variables T_{interp}, w_{interp}, and p_{RRTM} are ready to be placed into the RRTM time-by-time for evaluation.

By default for this study, the SW model is turned off and only LW is considered. In the case that SW is turned on, a few extra steps are taken for accurate calculations in the SW RRTM. Since the sun angle is important for SW calculations, reference latitude and the TPV's date are used to determine the solar zenith angle (SZA). If the SZA is greater than 90°, the SW model run is skipped. In these cases, the temporary heating rate array from the LW run becomes the total heating rate. If the SZA is less than 90°, the SW model runs and returns a temporary array which stores the SW heating rate. At this point, the saved LW and SW heating rates are combined to find the total heating rate, that is if the SW model was run and the addition is needed.

After the total heating rate is found for the single time step, EPV tendency is calculated for the vertical profile. Recall equation 1.2 from section 1.1.2:

$$\frac{D\Pi}{Dt} = \frac{\omega_a}{\rho} \cdot \nabla \frac{D\theta}{Dt} \simeq \frac{\zeta_a}{\rho} \frac{\partial}{\partial z} \left(\frac{d\theta}{dt} \right) \tag{2.4}$$

The vertical heating rate gradient is needed, as well as the density (ρ =1.225 kg m^{-3}), and the absolute vorticity, which is calculated prior to the RHR values. Vertical heating rate gradient is calculated using a centered-difference approach:

$$\left(\frac{\partial \dot{\theta}}{\partial z}\right)_i = \frac{\dot{\theta}_{i+1} - \dot{\theta}_{i-1}}{h_{i+1} - h_{i-1}} \tag{2.5}$$

where h represents the height of the layer, and i represents the layer numbers. For the top and bottom layers, the average value of that layer and the single adjacent layer was used. The vertical heating rate is then multiplied by the vertical profile of vorticity (which has been interpolated to match the heating rate levels output by the RRTM), and divided by ρ to calculate EPV. At this point, EPV has been calculated is in terms of (K s^{-1} km^{-1} kg^{-1} m^3) day^{-1} (since heating rate values are output as K day^{-1}). By dividing this by 1000, the units are in terms of meters only instead of kilometers. Then dividing by 10^{-6} gives EPV in potential vorticity units (PVU) per day (1 PVU = 10^{-6} K s^{-1} kg^{-1} m^2). Since the characteristics of TPVs are considered on such a localized scale, only $\pm$12 hours from the TPV's point of closest passage to Summit are plotted. Anomalies are found based on the mean heating rate from a time period 48 to 24 hours before the TPV's closest passage. This mean is used instead of a total 5-day mean in order to take a sample of the environment at Summit prior to the TPV's influence.

2.2.2.2 All-Sky

Microphysics data (the Shupe-Turner retrieval product) have been processed for dates before August, 2014. Microphysics data prior to April, 2012 are not being used due to instrumentation issues with the MPL at Summit. For the cases where microphysics data are available and data quality is good, which are most cases between the dates of April 2012 and August 2014, all-sky heating rates and EPV tendencies are calculated and plotted in addition to the clear-sky heating rates. For these cases, the methods described in section

2.2.2.1 remain the same, however an additional flag is set to identify that clouds will be included which requires several extra steps prior to running the RRTM.

The all-sky cases required pre-processing of the microphysics data prior to its entrance into the RRTM. When the all-sky flag is set to 'on', the RRTM also requires a cloud input file (IN_CLD_RRTM), which provides information on the cloudy layers and the cloud types. The data in this file comes from the cloud microphysics data in the ST product.

Once it has been determined that the run is an all-sky run, adjustments are made to the ST data to make it compatible with our user-defined RRTM layers. First, the appropriate ST files corresponding to the TPV's date are found, and then the ice water content (IWC), liquid water content (LWC), effective ice radius R_i and effective liquid radius R_l are extracted for a 3-day period, combining all three days into a single 3-day long array for each separate variable. A time increment (also user defined) is used to determine the resolution at which to use the data. For example, if half-hour runs are desired, the time increment would be set to 2, since there are 2 half-hours in one hour. For this study, an increment of 12 is used to consider 5-minutely cloud data. For simplicity, and since the values of R_i and R_l do not vary significantly over the time period, the mean values of R_i and R_l for each layer over the 3-day period are used.

The RRTM also requires the layer number of the cloudy layers (in regards to the model layers pre-defined for the RRTM to evaluate), total cloud water path for each cloudy layer, cloud fraction, and effective size of the ice and liquid particles in the layer. LWC, IWC, R_i and R_l come in 316 height bins which are have 45 meter resolution, however the RRTM layers are defined by 124 vertical levels (for this study). Because of this, LWC, IWC, R_i and R_l must be reduced to match the 124 levels that are provided for the RRTM, and LWC and IWC specifically must be integrated to find values for liquid water path (LWP) and ice water path (IWP) in each layer. As described in section 2.2.2.1, the RRTM layers are defined by 90 meter increments from 0 to 10 km above ground level. Cloud properties are not considered above 10 km, so all cloud features are set to 0 above this height, which also helps

account for the occasional spurious retrieval that appears in the data above these heights. For R_i and R_l, values are averaged in adjacent layers, starting with an odd-numbered layer and averaging with the layer above it.

LWP and IWP values for each model layer in the RRTM were found by integrating the LWC and IWC values in the following way:

$$\mathrm{LWP}_j = (\mathrm{LWC}_i)\Delta(\mathrm{h}_i) + (\mathrm{LWC}_{i+1})\Delta(\mathrm{h}_{i+1}) \tag{2.6}$$

where j represents the layer number in the model, i represents the layer number in the cloud retrievals dataset, and $\Delta(\mathrm{h}_i) = \mathrm{z}_{i+1} - \mathrm{z}_i$. The same process is used for IWP.

The heights associated with the original cloud data correspond to the center of the bin, and the center of the first bin exists at 135 m because the MMCR does not receive data below this point. For that reason, the first model level (from the surface to 90 m) maintains a value of 0 for all LWP and IWP arrays. Above this level, up to 10 km, values for LWP and IWP in adjacent layers are combined starting on odd numbered layers and saved in a new array that matches the vertical resolution of the RRTM layers. The top layer in this combined dataset corresponds to a height of 9855 m, which corresponds appropriately to the RRTM layers, considering that the first 135 m above ground level are neglected while combining bins. The final array contains cloud LWP and IWP from the surface to 10 km in 90 m increments, starting from layer 1, which is 90 m to 180 m, and layer 0 is left with 0 for all cloud property values to account for the radar's blind spot.

Total cloud water path (CWP) and ice fraction for each layer are calculated on an element-wise basis by the following method:

$$\mathrm{CWP}_{t,j} = \mathrm{LWP}_{t,j} + \mathrm{IWP}_{t,j} \tag{2.7}$$

$$\mathrm{FracIce}_{t,j} = \frac{\mathrm{IWP}_{t,j}}{\mathrm{CWP}_{t,j}} \tag{2.8}$$

where again j represents the layer number in the model and t represents the time. In the case that CWP is 0, FracIce is set to 0 to avoid division issues. This process is repeated for the entire time period, returning CWP, IWP, FRACICE, LWP, R_i and R_l as time by height arrays with the height field matching the RRTM model layers. A time range is set up matching the time increments set in the cloud pre-processing step. This time range becomes the RRTM calculations loop, which is higher temporal resolution than the clear-sky case. For this study, the RRTM is set to calculate separate ice and liquid cloud optical depths, requiring specification of cloud fraction, CWP, ice fraction, and effective radii for each layer. The RRTM is set to compute ice-cloud optical properties by a method based on the parameterization given in Fu et al. (1998) and compute liquid-cloud optical properties by a method based on the parameterization of water clouds by Hu and Stamnes (1993). Cloudy layers are found by taking the indices where CWP is greater than 0 for a given time step. Indices are taken as the layer number of the cloudy layer, and fill in the appropriate CWP, ice fraction, and effective radii of ice and liquid for each layer. Cloud fraction is taken as 1 for all cloudy layers. Once IN_CLD_RRTM is created, the methods follow the same steps as the clear-sky cases, running the LW RRTM and then the SW RRTM, if applicable. Heating rate gradients and EPV tendency are also calculated at the end of each time step and stored with 5-minute temporal resolution rather than hourly as in the clear-sky case. Anomalies in heating rates are calculated in the all-sky case with respect to the clear-sky mean values for each layer.

This method allows for flexibility in testing heating rates through the RRTM. To compute the heating rate from only changes in water vapor, the RRTM is run with the mean values of temperature in each layer and evaluate changes in the heating rates due to only the changes in water vapor. Multiple experiments of this type are run for this analysis. A summary of the experiment types that are tested and analyzed for this study is provided in Table 2.2.

Experiment 1 begins with the longwave radiative heating rate from all contributors, i.e. the all-sky case. The all-sky case shows the product of all forcings working together to contribute to the evolution of the radiative field. The following breakdown of experiment types allows us to consider how different forcings are contributing to the all-sky radiative field and possibly the evolution of a TPV.

Experiment 2 is the standard clear-sky case, used to test the sensitivity of only temperature and water vapor to the total heating rate field. In this experiment, the RRTM is run with the hourly values of temperature and water vapor only. Experiments 3-6 are used to then break down the clear-sky heating rate contributions further into components from the mean state of temperature and water vapor and the perturbations by temperature and water vapor. Experiment 3 considers the heating rate due to the mean temperature and the mean water vapor in the entire analysis period. The result of this experiment is a single radiative heating rate vertical profile. Experiment 4 tests the sensitivity of the heating rate to the background temperature only by holding water vapor mixing ratio at 0 g kg^{-1} and computing the radiative heating rate profile based on the mean temperature only. The outputs from experiments 3 and 4 provide a baseline value for the background fields' contributions to the total radiative field.

Experiments 5 and 6 are created to test the sensitivity of the radiative field to temperature and water vapor perturbations. Experiment 5 accomplishes this by using the background (mean) temperature profile from experiment 4 while taking the observed water vapor profile at each time step to acquire a time series of heating rate profiles that are due to water vapor changes only. Experiment 6 is similar to experiment 5, however it uses the background (mean) water vapor for each time step while considering the observed temperature profile to consider how the radiative heating rates change due to temperature.

The final two experiments, 7 and 8, are designed to test the sensitivity of the heating rate field to ice and liquid clouds, respectively. Experiment 7 uses the background temperature and background water vapor used in experiment 3 but also considers the effects of ice

in clouds, ignoring liquid. Experiment 8 uses the also uses background temperature and background water vapor but considers the effects of liquid in clouds, ignoring ice. These experiments provide a method to isolate the radiative effects of various cloud types, based on observed quantities of liquid and ice over Summit, and consider their contributions to the total longwave radiative field shown by experiment 1.

Experiment	$\overline{T}$	$\overline{q_v}$	T	q_v	q_i	q_l	**Description**
1			X	X	X	X	**All sky** - heating rate from all forcings
2			X	X			**Clear Sky** - heating rate from temperature and water vapor only
3	X	X					Heating rate from *background temperature* and *background water vapor*
4	X						Heating rate from *background temperature* only
5	X			X			Heating rate contribution from *water vapor* perturbation
6		X	X				Heating rate contribution from *temperature* perturbation
7	X	X			X		Heating rate contribution from *ice* in clouds
8	X	X				X	Heating rate contribution from *liquid* in clouds

Table 2.2: Summary of experiments run for this study using the RRTM and different forcings. An X represents the presence of the forcing in the respective experiment.

Chapter 3

Results and Analysis

The goal of this research study is to improve the understanding of TPVs by taking a unique look at observed characteristics. Observationally, the structure, cloud properties, and radiative properties of passing TPVs are evaluated to compare to previous literature. To begin, a case study is broken down to illustrate the challenges and details associated with this analysis. The case study will help set the stage for an evaluation of composite features based on all TPVs in this study.

3.1 Case Study

The case study at hand is a TPV that existed from 17 July 2012 to 31 July 2012. This TPV progressed north to south over Summit before moving off to the east, with its core passing the closest to Summit at 23Z on 24 July 2012 (Figure 3.1). This case was chosen based on the simplicity of its track over Summit (i.e. follows a straight path rather than jagged, allowing for a straightforward analysis of its structure and properties as it passes), its proximity to Summit at its closest point (17.6 km), and because mixed-phase clouds exist during its passage over Summit allowing for the analysis of the radiative effects of such clouds. This TPV is one of the larger TPVs from the dataset used, with an estimated radius of 339 km at its closest point, averaging about 350 km in radius during the $\pm$12 hours surrounding its passage. During a 12-hour period, including 6 hours before and 6 hours after the TPV's closest passage, this TPV had a net amplitude increase of about 2 K, increasing from about 15 K to 17 K (Figure 3.2). While many hourly fluctuations in amplitude are apparent from reanalysis during this period, the TPV had an average hourly amplitude increase of 0.05 K over the 12 hour period (equivalent to 0.1 K day^{-1}). The core potential temperature remained steady within this 12 hour period at about 298 K, and

the last closed contour potential temperature increased by only about 1 K over the 12 hour period, from 305 K to 306 K.

The Shupe-Turner cloud product showed that mixed-phase clouds were present during this TPV's passage over Summit (Figure 3.3). Optically thin, low-level ice clouds existed at Summit as early as 11Z on the 24th, which contained liquid layers within. Between 15Z and 19Z, a liquid layer formed at about 1 km in height, above an ice cloud extending to the ground. At 18Z, ice clouds grew and the liquid layer dissipated, with light precipitation in the form of ice. Ice precipitation began to increase at Summit at 20Z, coinciding with the time the TPV's core was beginning to reach Summit (ref. Figure 3.1). From 22Z to 23Z, the ice precipitation was accompanied by liquid precipitation, before the cloud dissipated around 00Z on the 25th. At this time, the TPV still existed over Summit but was beginning to move away to the east. Small amounts of liquid existed near the surface after 00Z but the environment at Summit was mostly clear-sky until 04Z when an ice cloud formed between 3 and 4 km. This cloud may or may not have been associated with the TPV, since the outer contours of the TPV are still near Summit, however it is difficult to say with certainty which clouds in the environment were due to the TPV and which were not.

The structure of this TPV is evident in the temperature and moisture changes it induces at Summit as it passes (Figures 3.4 and 3.5). The tropopause has already begun to lower as early as July 24th at 11Z, which is when outer boundaries of the TPV begin to reach Summit (Recall Figure 3.1). Beginning around 13Z on the 24th, isotherms that are representative of the stratosphere begin to decrease in height along with the lowering tropopause, indicating that the TPV's presence is influencing the midlevels at Summit. Temperatures in the 230 K - 240 K range, which are prevalent above the tropopause, reach as low as 4 km, breaking the band of near 220 K temperatures at heights representative of the tropopause when the TPV is not near (Figure 3.4a). This temperature change is clear when looking at temperature anomalies (Figure 3.4b), in which warm, stratospheric air is associated with a

positive anomaly above the tropopause where cool, tropospheric air usually exists. Negative temperature anomalies below the tropopause extend from about 14Z to nearly 07Z on the 25th. These anomalies are associated with the cool air from the top of the troposphere reaching lower levels where the environment is generally warmer. The coldest anomalies exist just below the tropopause near the TPV's center, which is at the time when the TPV is closest to Summit and the tropopause is the lowest.

Relative humidity (RH) values at Summit are high at the tropopause at the earliest times of the TPV's approach (i.e. 11Z to 15Z), reaching values above 80% (Figure 3.5a). Consistently lower values of RH exist above 6 km. As the tropopause lowers, beginning around 15Z on the 24th, RH drops to near 50% just above the tropopause with a relatively drier pocket of air between the background tropopause (6 km AGL) and the lowered tropopause (4-5 km AGL) from 15Z on the 24th to 00Z on the 25th. This dry pocket of air continues to extend downward after the TPV passes, creating a "sloped" structure, evident by the near 50% RH values extending from the tropopause at 23Z to the surface at 09Z the next day. Drier values exist below the tropopause after the TPV's passage likely due to subsidence on the upstream side of a TPV, a common property of PV anomalies (Holton 2004). While subsidence associated with PV anomalies is a previously noted feature, the shape (i.e., the narrow, descending dry air) of this specific feature is unique from previous literature, and is also found in the composite structure of TPVs (ref. section 3.2.2). Similar features are notable when considering anomalous RH over the time period. Negative anomalies exist above the tropopause during times when the tropopause is lowered, as dry stratospheric air is intruding into the normally moist tropospheric air (Figure 3.5b). Positive RH anomalies are apparent below the tropopause leading up to the time of closest passage and near the surface shortly after passage. These positive anomalies could be due to southerly flow ahead of the TPV transporting moisture into the region.

Radiative properties of this TPV are investigated in a series of experiments described by table 2.2, beginning with a brief overview of the full radiative forcing. Generally, cooling

rates are greater in the presence of clouds (Figure 3.6a). For example, radiative heating rate (RHR) values of less than -5 K day^{-1} exist where notable gradients in optical depth are present, such as between ice and liquid layers from 15Z to 18Z. This also occurs near cloud top from 21Z to 23Z, where there is a significant gradient in optical depth due to the cloud to no-cloud transition above the tropopause. At this time, liquid to ice RHR gradients also exist in the cloud-top region. Background RHR values remain mostly between -1 K day^{-1} and -2 K day^{-1}, which is consistent with LW clear-sky RHR values found by Turner et al. (2018) (e.g., figures 1.21, 1.22, 1.23). Anomalous values of RHR show enhanced cooling in the regions described (e.g. ice to liquid gradients and cloud to no-cloud gradients), with positive anomalies in RHR values below cloud bases and in small regions below areas of liquid inside ice clouds (Figure 3.6b).

The radiative scene can be broken down by considering the clear-sky properties of the TPV as analyzed at the point location of Summit. Clear-sky RHR values show the largest cooling near the surface during the entire time period considered, at values near -3 K day^{-1} (Figure 3.7a). RHR values at the tropopause remain consistently between -1 K day^{-1} and -2 K day^{-1}, however a notable area of higher RHR values is apparent between 4 and 6 km from 18Z on the 24th to 02Z on the 25th. This time period is coincident with the TPV's presence over Summit. Before 23Z, these relatively small RHR values are above the tropopause, but beginning at 23Z, the tropopause begins to rise again allowing the pocket of smaller values to exist below the tropopause for an additional 2 hours. clear-sky heating rate anomalies appear to be relatively constant over the time period analyzed. For example, a band of negative anomalies exists at 6 km from 11Z on the 24th to 10Z on the 25th. Positive heating rate anomalies encompass the tropopause during the entire time period. The highest anomalies exist after the TPV's passage, extending downward to the surface between 02Z and 09Z (Figure 3.7b).

To better understand the clear-sky RHR values associated with this TPV, a break down of heating rate contributions from various forcings is done. The background state of water

vapor in the atmosphere over Summit has a larger contribution to the total heating rate profiles than temperature alone (Figure 3.8). When including water vapor in the computation of the background heating rate profile, RHR values throughout the profile decrease from only about -0.5 K day^{-1} to less than -1.0 K day^{-1} below 8 km and up to -2.0 K below 1 km. The radiative influence of the background water vapor is greatly impacted by the presence of higher water vapor concentrations near the surface than aloft. In addition, water vapor's radiative influence is also likely impacted by the presence of mixed-phase clouds during much of the analysis period. Considering the profile of RHR from the mean water vapor, there are layers of increased cooling between 0.25 km and 1.25 km. These layers correlate relatively well with heights in which cloud optical depth and relative humidity change (ref. figures 3.3 and 3.5). Near the surface, low level clouds exist over much of the time period, with cloud top heights located below 2 km. RHR is below -1.5 K day^{-1} up to 4 km (Figure 3.8), with most clouds existing below this height. The evaluation of RHR due to the mean state of temperature and water vapor done here is important to consider for the remainder of the analysis. Experiments 5-8 make use of these RHR profiles to investigate the effects from perturbations of these state variables and clouds.

RHR values from temperature and water vapor perturbations remain somewhat steady during the analysis period, with small indications that the TPV is present. RHR values from water vapor perturbations show lower cooling rates above the tropopause relative to the stronger cooling below, as expected, since water vapor concentration greatly decreases above tropopause height (Figure 3.9a). The time period between 21Z and 03Z shows stronger cooling rates (between -2 K day^{-1} and -3 K day^{-1}) below the tropopause, which is during the time the TPV was directly over Summit and the tropopause was the lowest. During this time, relative humidity was higher than average below the tropopause, as shown in figure 3.5b. The gradient in moisture between 1 km and 2 km leads to the increased cooling at this level. At the tropopause during this time, RHR values are between

-1 K day^{-1} and -2 K day^{-1}, representative of the general magnitude of clear-sky cooling rates.

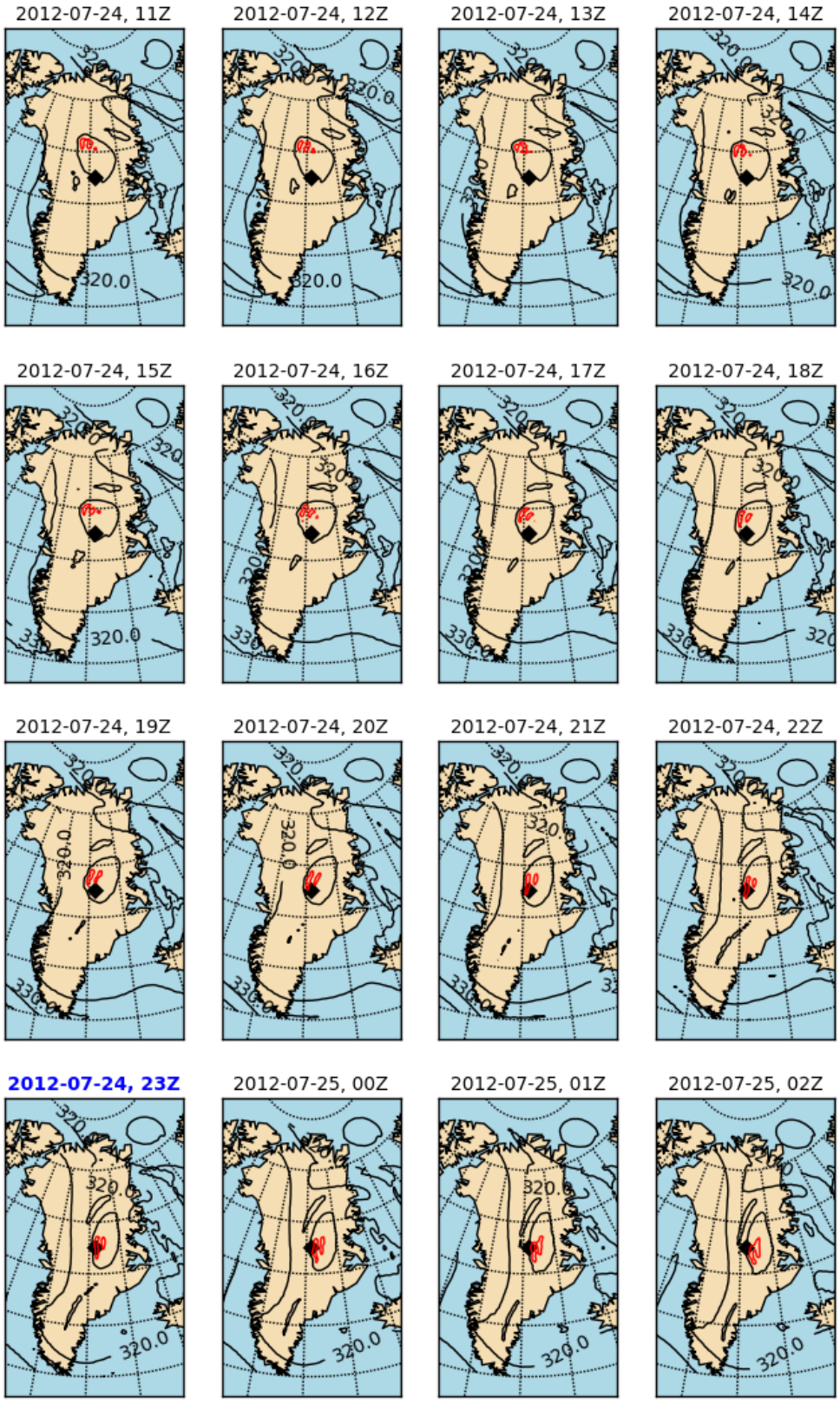
RHR values due to temperature perturbations only (Figure 3.9b) show values in the -1 K day^{-1} to -2 K day^{-1} range at the tropopause level for much of the time period, with a small region of smaller than average cooling (between 0 K day^{-1} and -1 K day^{-1}) just below the tropopause from 21Z to 00Z. A region of stronger cooling exists above the tropopause, near 6 km above ground level, throughout much of the time period. These RHR values, the weaker cooling below the tropopause and stronger above, coincide with regions of anomalously low temperatures below the tropopause and anomalously high temperatures above, respectively, as seen in figure 3.4b. Comparing to figure 3.8, RHR values in the lowest levels are consistent with water vapor gradients from the mean water vapor in the profile. While temperature perturbations offer some changes to the heating rate, these changes are small. Considering the difference between the RHR from water vapor perturbations and temperature perturbations, it is clear that water vapor has much more influence on the clear-sky RHR below the tropopause and temperature has more influence on the clear-sky RHR above the tropopause (Figure 3.9c). This fact becomes important in later sections when considering RHR and EPV tendency composites broken down by forcing.

While figures 3.8, and 3.9 show longwave cooling at the tropopause during the time period when the TPV is over Summit, these values are relatively small compared to RHR with clouds. Along with this fact, anomaly values from figure 3.7b show that clear-sky cooling rates at the tropopause during the entire analysis period are higher than average, making it unlikely that clear-sky radiative effects are significantly contributing to the 12 hour net increase in amplitude that this TPV experienced according to reanalysis. An important next step is to consider the radiative effects of the clouds present during the time of this TPV's passage and question whether these clouds assisted in the intensification of the TPV.

Longwave radiative cooling rates were enhanced due to ice clouds present during the TPV's passage. During the time period between 18Z and 00Z, radiative cooling within the

growing ice cloud increases (Figure 3.10a). This enhanced cooling, with RHR values less than -5 K day^{-1}, is present within the cloud and throughout the depth of the layer between the surface and the tropopause. This cloud extends slightly above the tropopause and the cooling rates within the cloud overlap the tropopause during the time when the TPV's core was directly over Summit. An elevated ice cloud also exists between 03Z and 08Z on the 25th of July, however this cloud is likely not influencing the TPV, as the TPV's core has already moved away from Summit by this time. The liquid clouds present during the analysis period also enhance the longwave cooling significantly. While many of the hours before the TPV's closest point show liquid layers close to the surface, liquid exists at the top of the ice cloud that is present between 18Z and 00Z (Figure 3.10b). This cloud-top liquid provides further enhancement of radiative cooling at the tropopause during the time period when the TPV's core is over Summit.

When considering all forcings together, it is clear that clouds greatly enhance the radiative cooling during the analysis period, July 24th, 11Z to July 25th, 11Z. More importantly, this enhanced cooling is found across the tropopause which is hypothesized to be important for intensification of TPVs. During the time when the tropopause was the lowest and the TPV's core was the closest to Summit, enhanced cloud top cooling from both ice and liquid clouds exists at the tropopause (Figure 3.6a). RHR anomalies have large negative values at the tropopause from approximately 19Z to 23Z due to the presence of clouds (Figure 3.6b), in opposition to the weak positive anomalies at the tropopause noted in the clear-sky case. For this case, it is likely that cloud top radiative cooling in the TPV's core contributed to the average hourly amplitude increase seen over a 12 hour period.


2012-07-24, 11Z
2012-07-24, 12Z
2012-07-24, 13Z
2012-07-24, 14Z
2012-07-24, 15Z
2012-07-24, 16Z
2012-07-24, 17Z
2012-07-24, 18Z
2012-07-24, 19Z
2012-07-24, 20Z
2012-07-24, 21Z
2012-07-24, 22Z
2012-07-24, 23Z
2012-07-25, 00Z
2012-07-25, 01Z
2012-07-25, 02Z

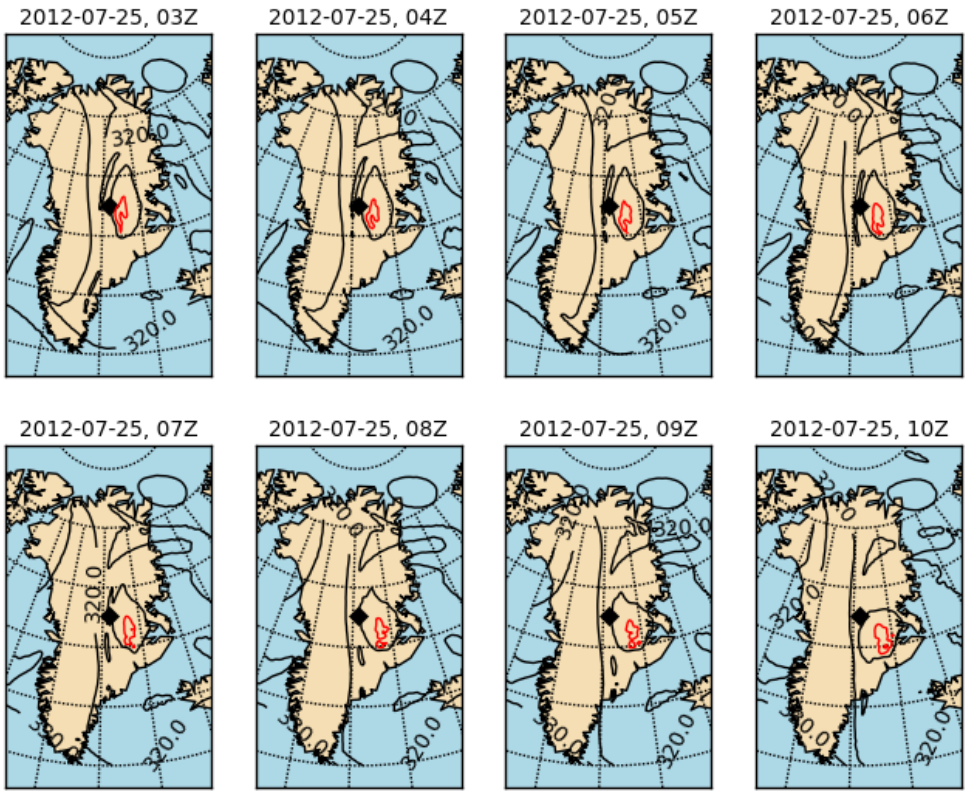


Figure 3.1: Hourly plots of potential temperature contours on the 2 PVU surface for ± 12 hours of the TPV passing over Summit on 2012-07-24 at 23Z (highlighted in blue). The red contour is representative of the TPV's core (minimum θ: 298 K, red contour: 300 K). Contours intervals are 10 K (i.e., the first black contour outward from the red contour is 310 K).

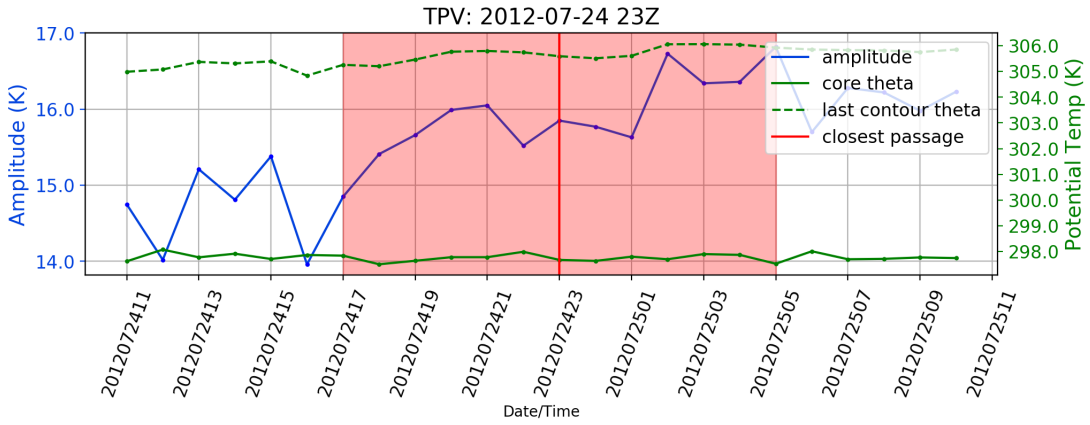


Figure 3.2: Line plots showing the TPV's amplitude (blue), core potential temperature (green), and last closed contour potential temperature (green dashed). The vertical red line represents the time of the TPV's closest passage, on 24 July 2012 at 23Z. The red shading represents the $\pm$6 hours from the TPV's closest passage

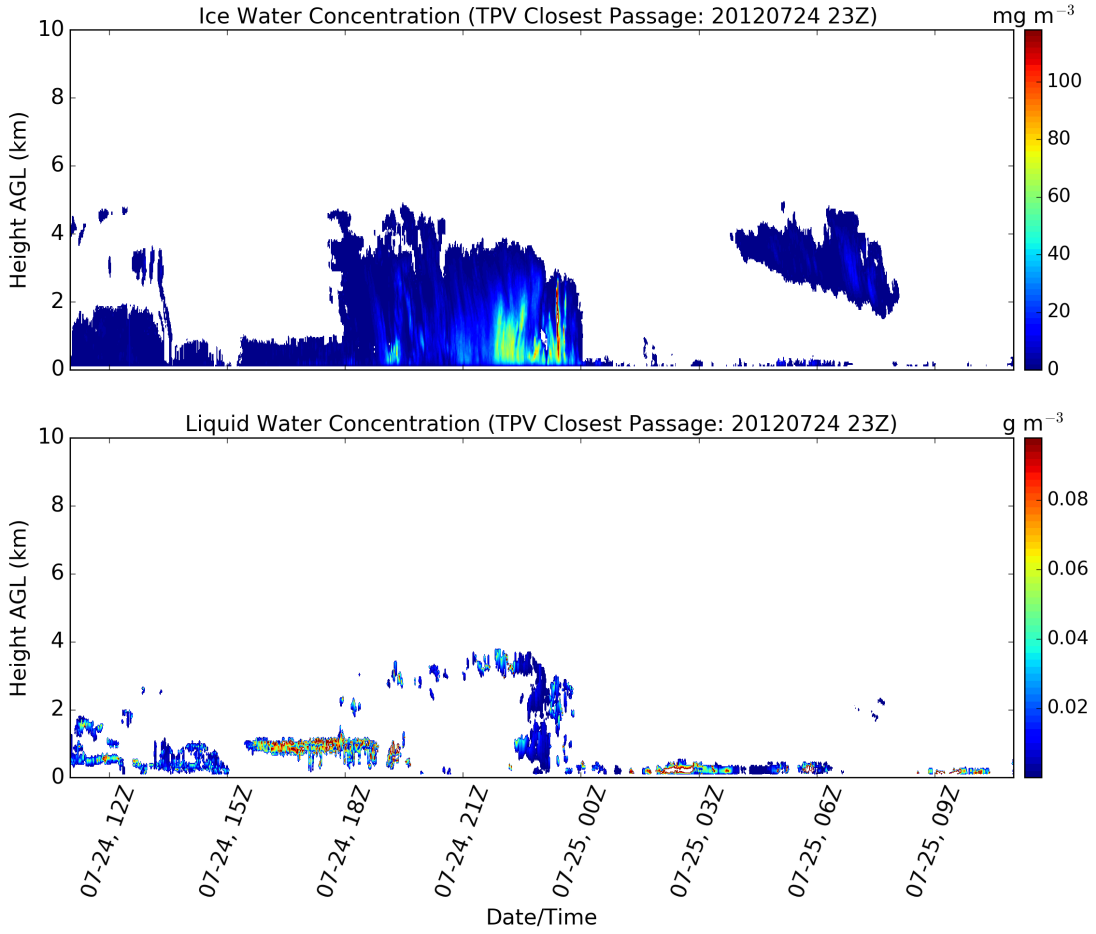


Figure 3.3: Time-height cross sections showing ice water concentration (top) and liquid water concentration (bottom) at Summit over the time period of the passing TPV on 24 July 2012. Ice water concentration is given in mg m^{-3} and liquid water concentration is given in g m^{-3}.

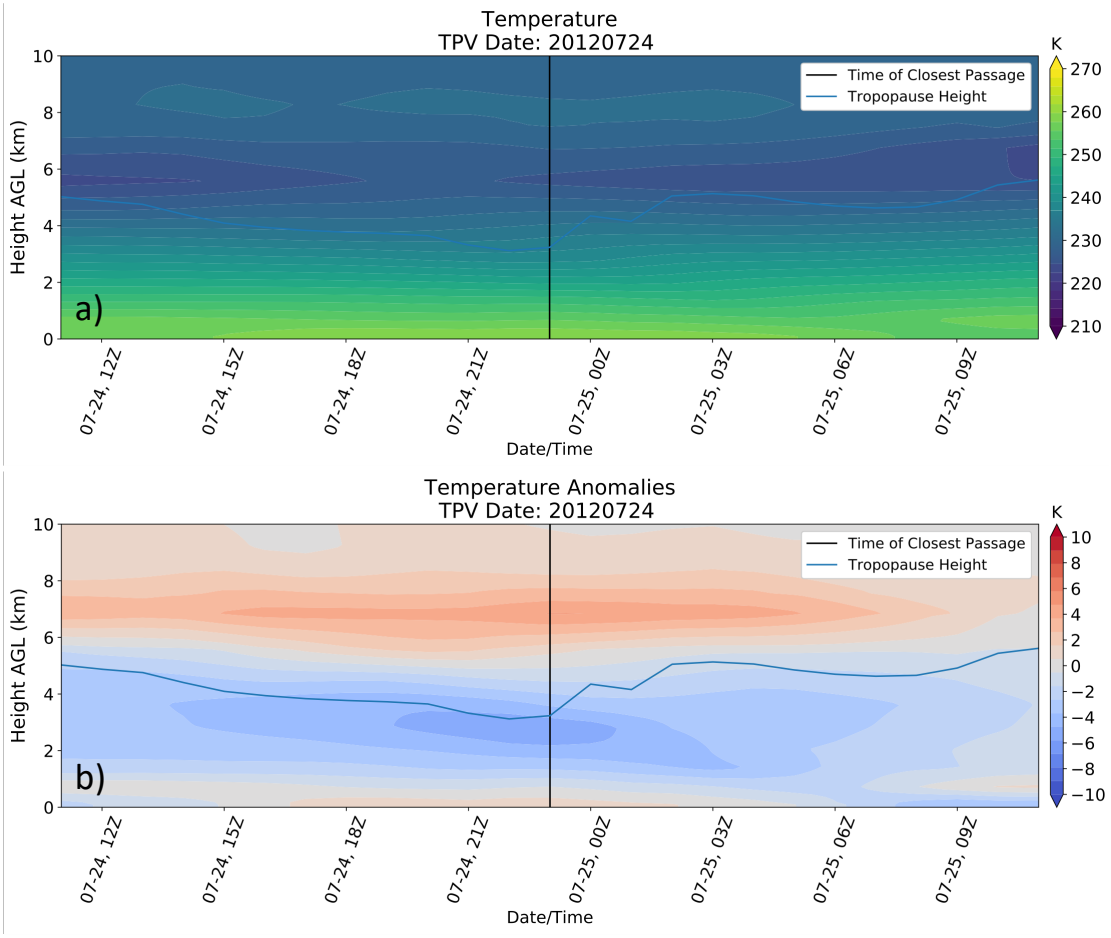


Figure 3.4: Time-height cross sections of a) temperature (K) and b) temperature anomalies (K) centered on 24 July 2012 at 23Z. Height is shown in km above ground level at Summit. The black vertical line represents the time the TPV's core was the closest to Summit, 24 July 2012 at 23Z. The blue line represents the height of the 2 PVU surface from ERA5.

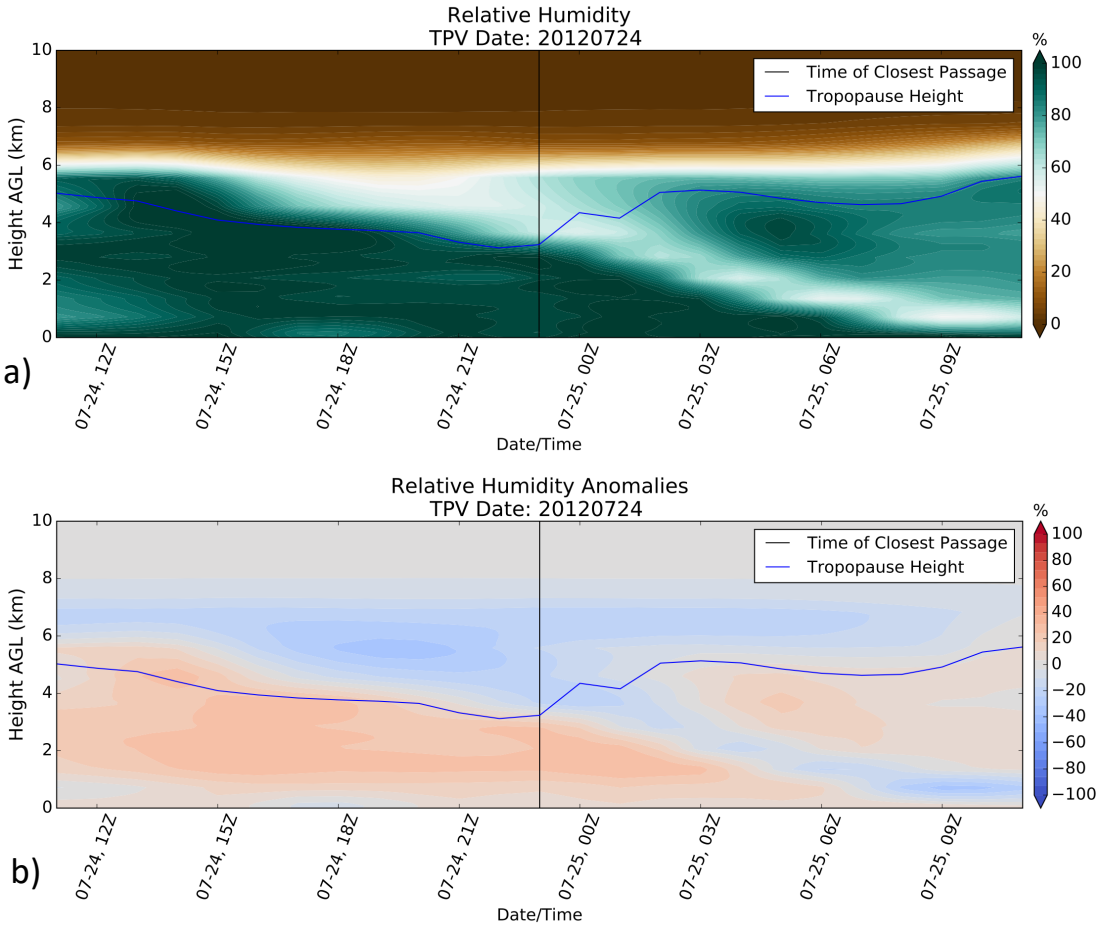


Figure 3.5: Time-height cross sections of a) relative humidity with respect to liquid water (%) and b) relative humidity anomalies (%) centered on July 24th, 2012 at 23Z. Height is shown in km above ground level at Summit. The black vertical line represents the time the TPV's core was the closest to Summit, 24 July 2012 at 23Z. The blue line represents the height of the 2 PVU surface from ERA5.

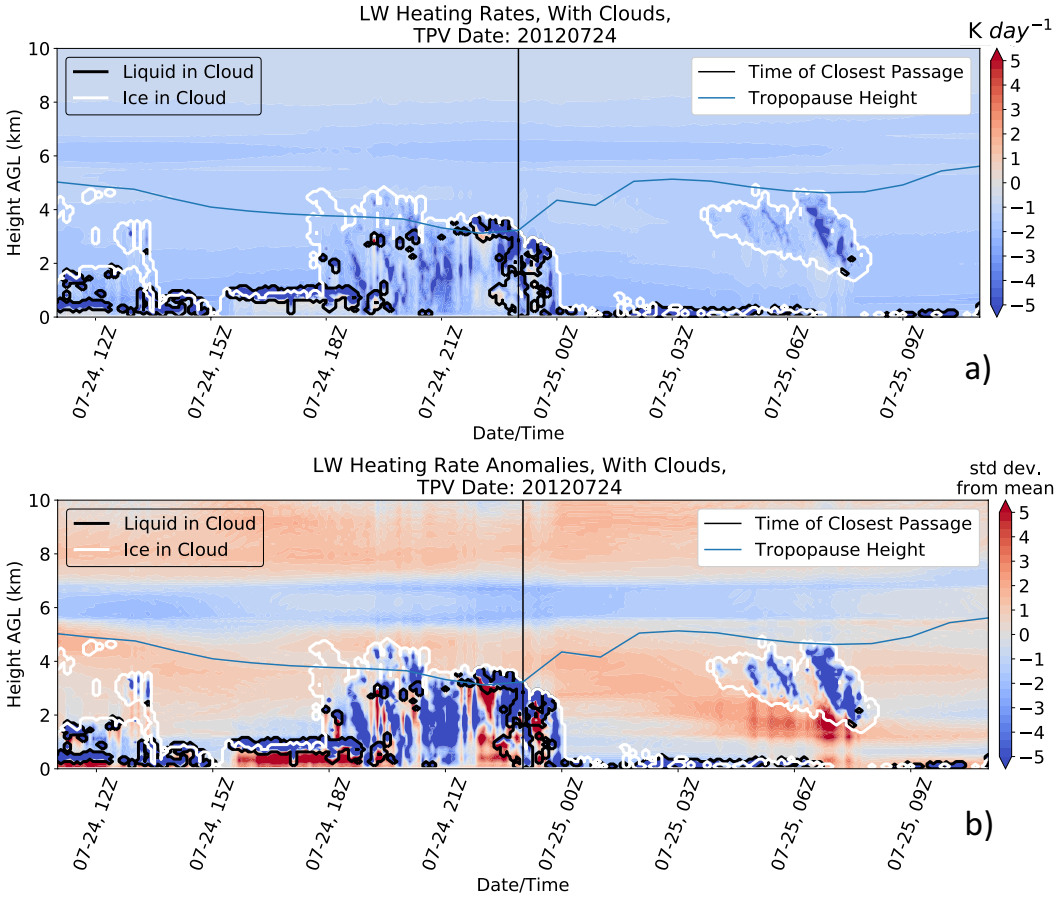


Figure 3.6: Results from experiment 1 in table 2.2 showing the time-height cross section of a) all-sky, longwave RHR centered on 24 July 2012 at 23Z and b) the standardized anomalies of the all-sky, longwave RHR. The black vertical line represents the time the TPV's core was the closest to Summit. The blue line represents the height of the 2 PVU surface from ERA5. Black contours represent liquid clouds and white contours represent ice clouds.

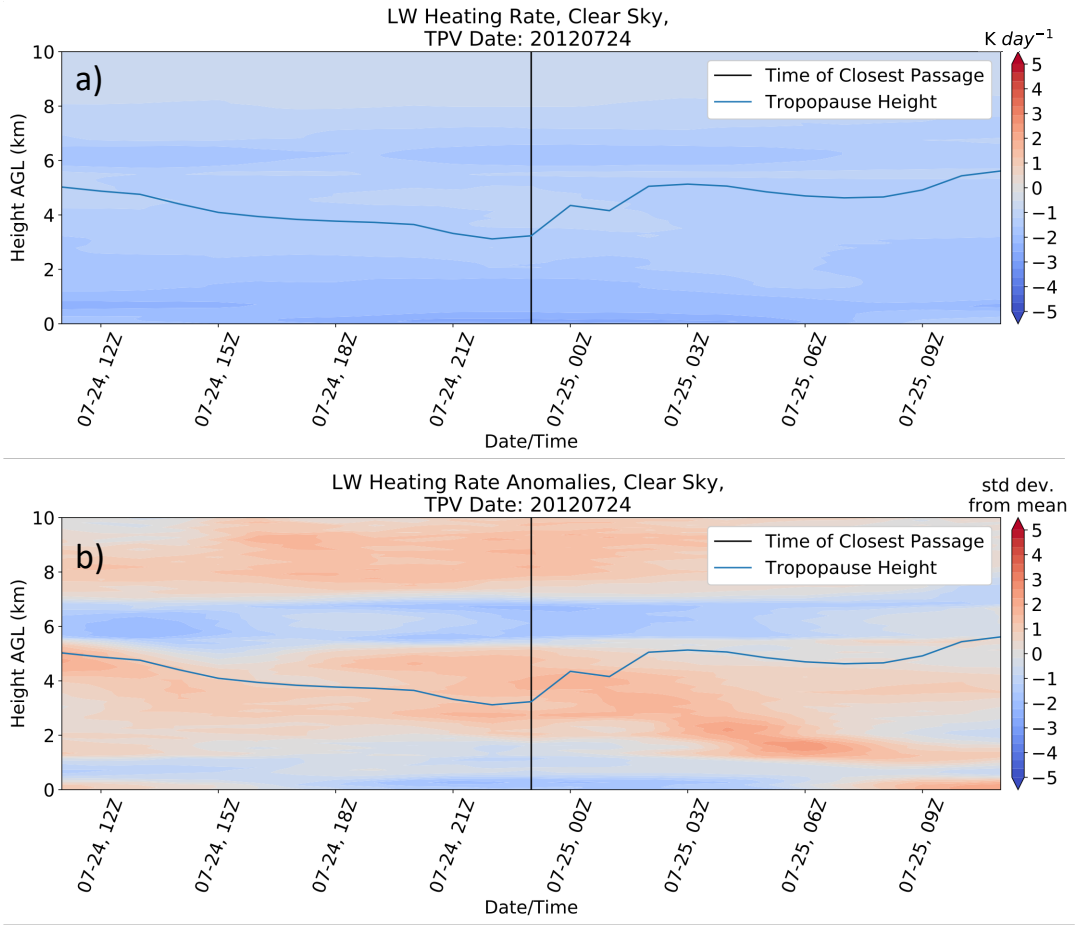


Figure 3.7: Results from experiment 2 in table 2.2 showing the time-height cross section of a) clear-sky, longwave RHR centered on 24 July 2012 at 23Z and b) the standardized anomalies of the clear-sky, longwave RHR. The black vertical line represents the time the TPV's core was the closest to Summit. The blue line represents the height of the 2 PVU surface from ERA5.

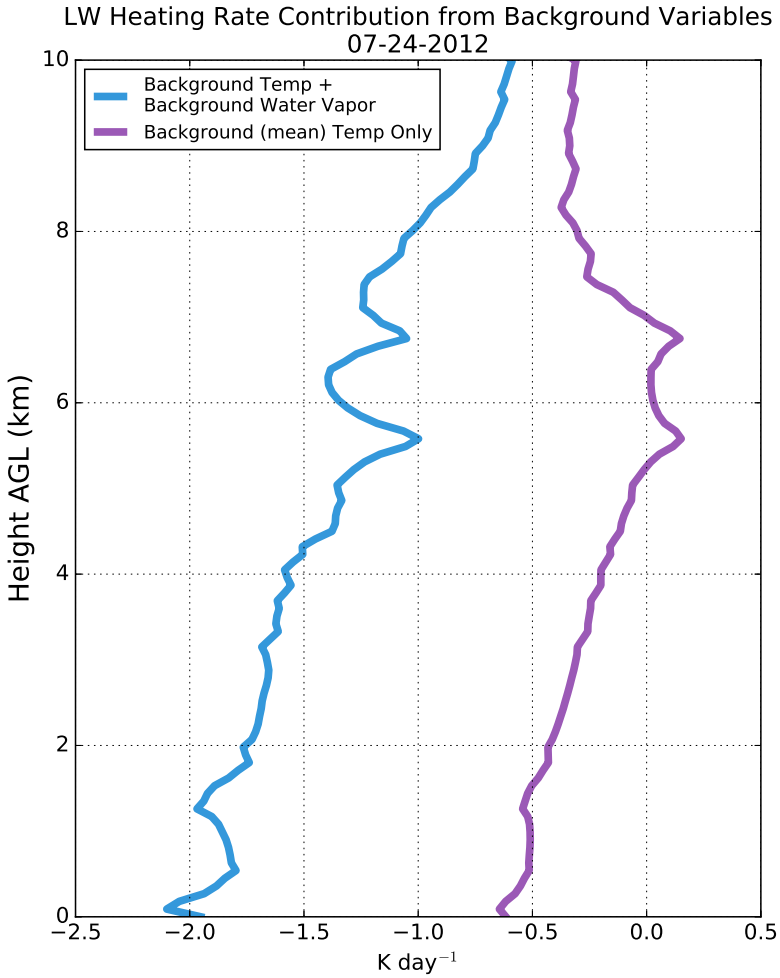


Figure 3.8: Results from experiments 3 and 4 in table 2.2 showing the heating rate profile from the mean water vapor and mean temperature (blue), and the mean temperature only (purple) in each layer over a 5-day period centered on 24 July 2012 at 23Z.

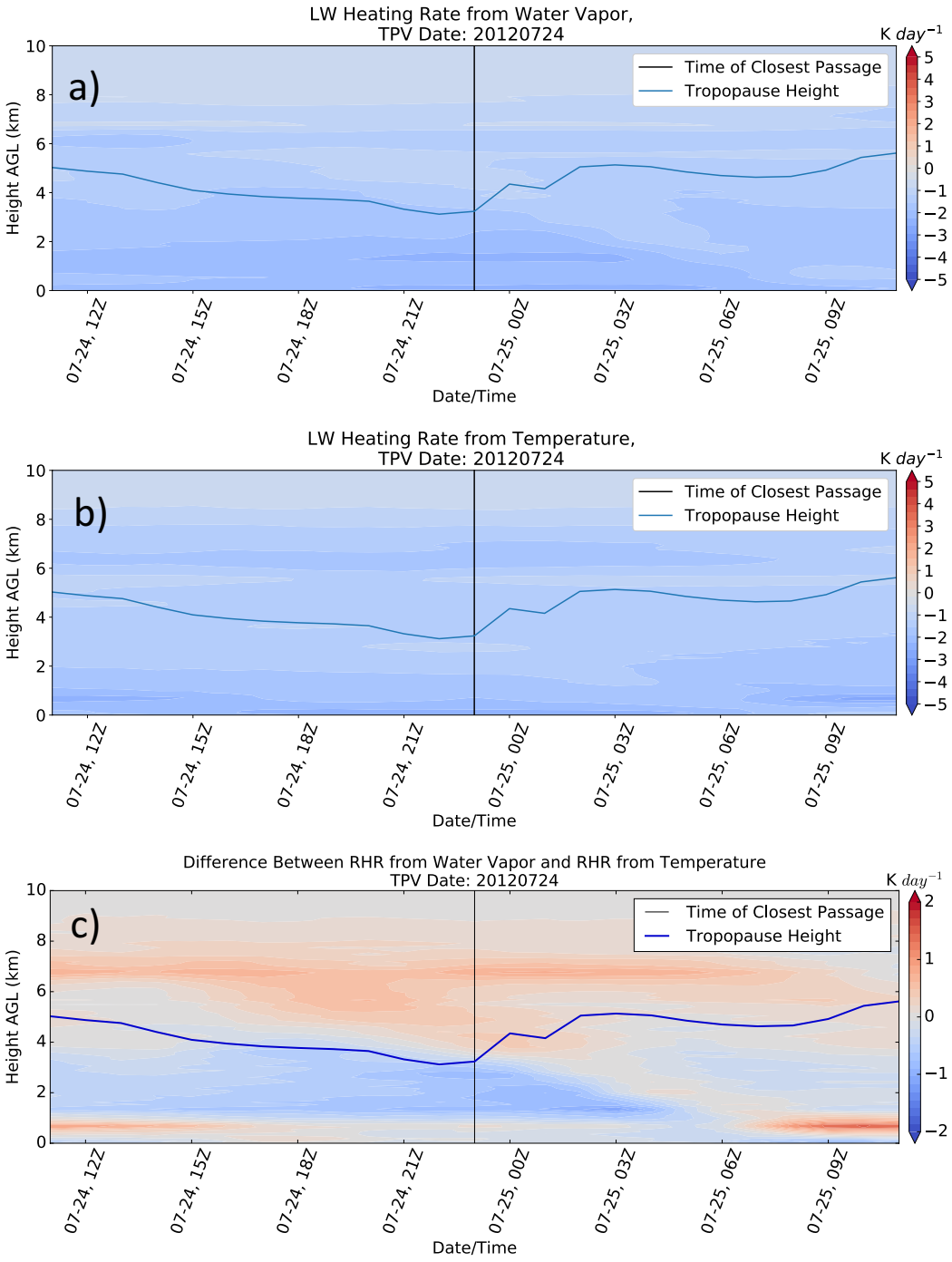


Figure 3.9: Results from experiments 5 and 6 in table 2.2 showing time-height cross sections of longwave RHR values from a) water vapor changes only, b) temperature changes only, and c) the difference between a and b centered on 24 July 2012 at 23Z. The black vertical line represents the time the TPV's core was the closest to Summit. The blue line represents the height of the 2 PVU surface from ERA5.

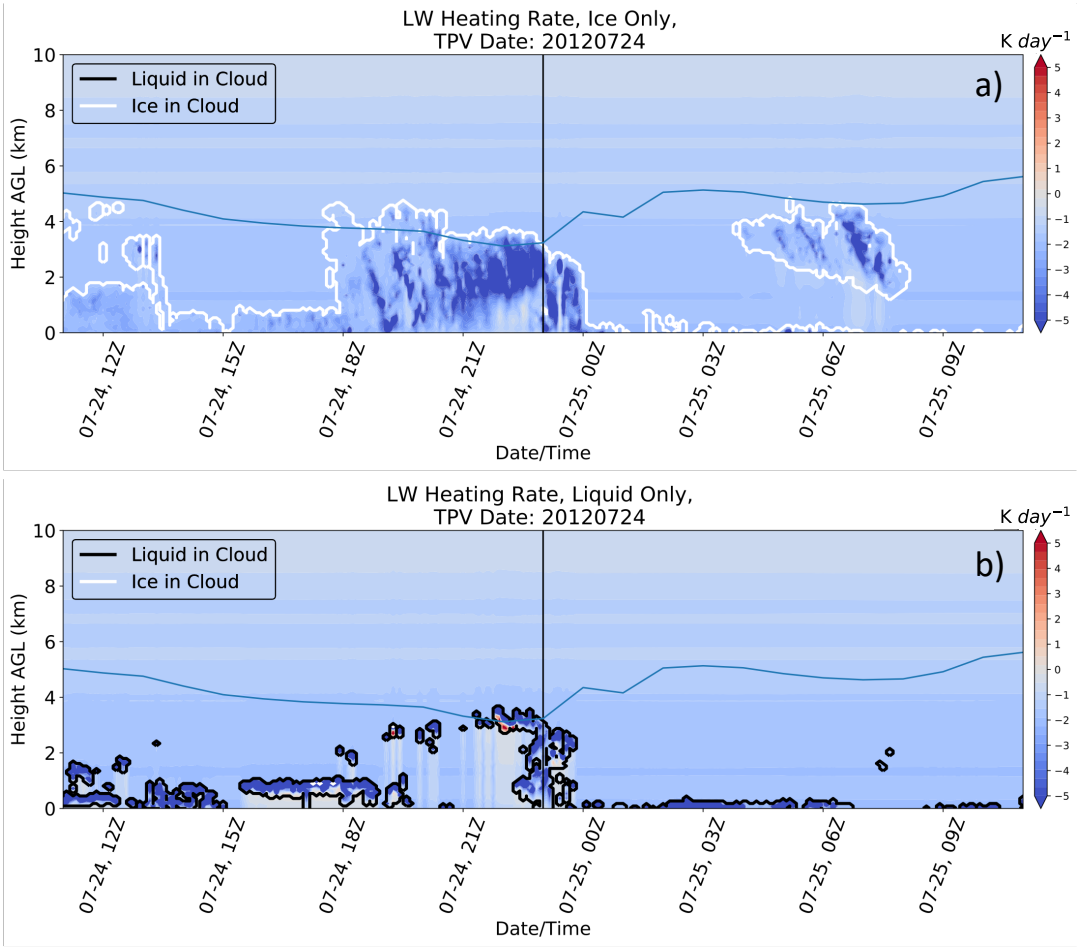


Figure 3.10: Results from experiments 7 and 8 in table 2.2 showing time-height cross sections of longwave RHR values from a) ice in clouds only and b) liquid in clouds only, centered on 24 July 2012 at 23Z. The black vertical line represents the time the TPV's core was the closest to Summit. The blue line represents the height of the 2 PVU surface from ERA5. Black contours represent liquid clouds and white contours represent ice clouds.

3.2 General Characteristics and Composites

TPVs are theorized to have have structures with positive (negative) temperature anomalies above (below) the tropopause, negative (positive) moisture anomalies above (below) the tropopause, cyclonic wind fields, steady increases in amplitude from water vapor gradients, and more dramatic increases in amplitude from clouds (Cavallo and Hakim 2009, 2010). Clouds are expected to be associated with TPVs since TPVs are known to have reduced static stability and higher relative humidities in the lower troposphere (Cavallo and Hakim 2013). This section will investigate the dataset at hand for the hypothesized features of TPVs, starting with an overview of properties of the dataset to understand features on a case-by-case basis and moving into composite cross-sections to analyze structure.

3.2.1 Atmospheric State Properties

The dipoles of anomalous temperature and moisture surrounding the core of a TPV are important features defining a TPV's structure. This study shows that larger and stronger TPVs tend to have stronger dipoles in temperature (figure 3.11a). TPVs in the lowest quadrant of our dataset (i.e., 22 TPVs which are smaller than 170 km in radius and weaker than 10 K at their closest point to Summit; the 10 K threshold was chosen based on visible clustering of TPVs in this section of the plot) have an average temperature anomaly dipole strength of 6.3 K, while TPVs larger and stronger than 170 km and 10 K (18 TPVs), respectively, have an average temperature anomaly dipole strength of 9.4 K. No clear correlations exist between strengthening or weakening TPVs and the strength of the TPV's temperature anomaly dipole, however many of the cases with dipole strengths greater than 10.5 K are TPVs that strengthened on average over the time period considered. This implies that the strength of the temperature dipole may be an important factor in TPV intensification, or possibly that TPV intensification leads to a stronger dipole. This idea will be evaluated further in subsequent sections.

The same correlations do not appear in the case of moisture anomaly dipoles. Larger and stronger TPVs do not have stronger moisture dipoles, as in the temperature anomaly dipoles. It is apparent, however, that while there is a large variety of dipole strength values in the lowest quadrant of the dataset, many of these with the highest values are strengthening cases (figure 3.11b). All but one of the strengthening cases in this lowest quadrant have water vapor mixing ratio anomaly dipoles greater than 0.5 g kg^{-1}, and all but one of the weakening cases in this quadrant have dipole values lower than 0.4 g kg^{-1}. Based on this information, the strength of the water vapor dipole near the core of a TPV appears to be influential in the strengthening of TPVs, especially for smaller or weaker TPVs. Not as much can be said, based on this dataset, for the influence of the water vapor dipole on larger or stronger TPVs. Water vapor gradients will also be considered in further detail in the subsequent sections when considering structure and radiative influences. Note that the case study described in section 3.1 is the TPV with radius 345 km and amplitude 16 K. This was a strengthening case with a temperature anomaly dipole strength of about 9 K and water vapor mixing ratio anomaly strength of about 0.4 g kg^{-1}. Both of these values are near the larger end of the spectrum of dipole strengths.

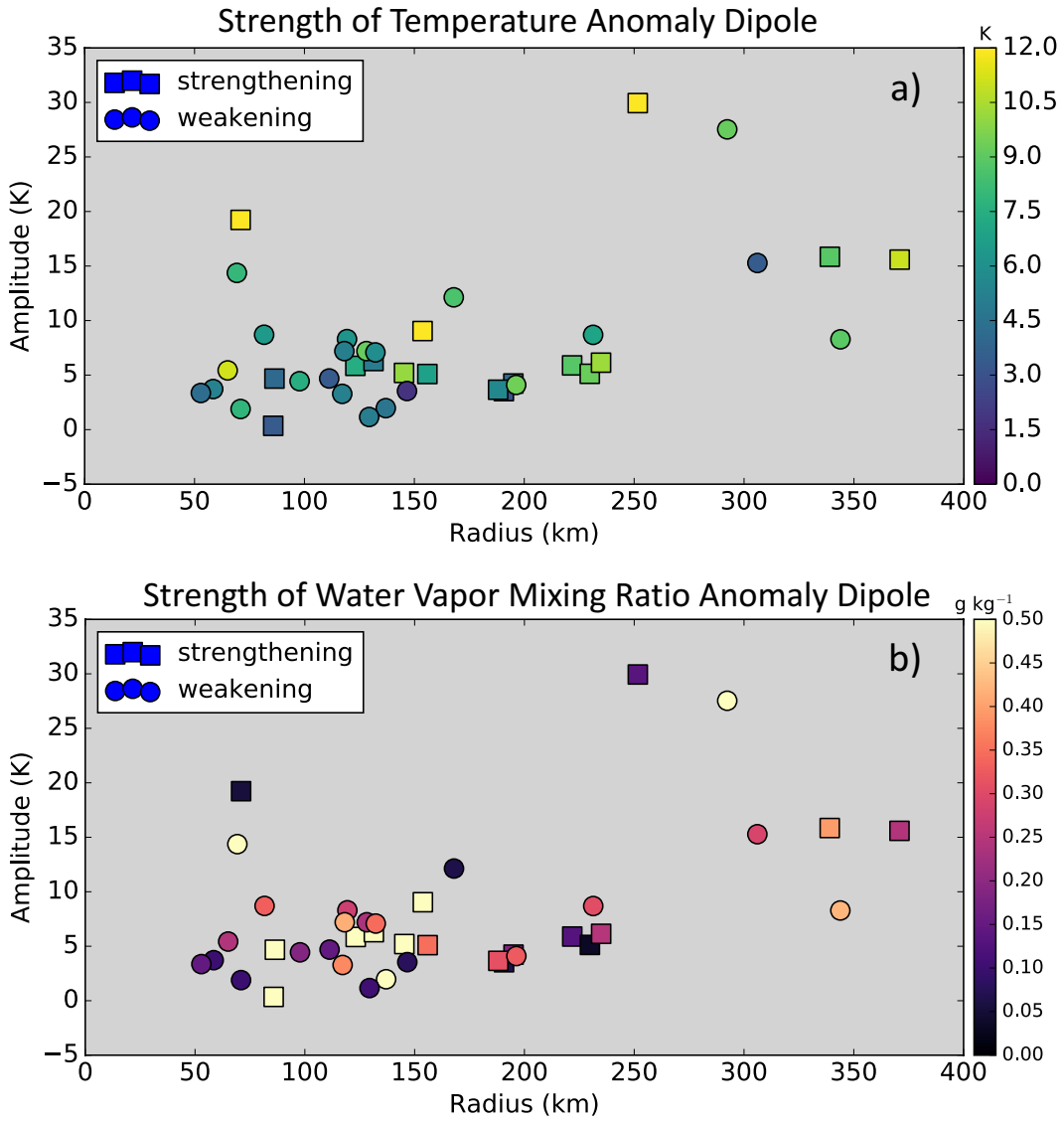


Figure 3.11: Scatter plot showing size, amplitude, and atmospheric state properties for the 40 TPVs in the analysis. The size and amplitude of each TPV are taken at the time of the TPV's closest point to Summit. Squares represent TPVs that strengthened, on average, over a 12-hour period surrounding the TPV's closest passage to Summit, and circles represent TPVs that weakened, on average, over the 12-hour period. Colors represent the average 12-hour difference between the maximum positive anomaly and minimum negative anomaly (i.e. the anomaly dipole) for a) temperature and b) water vapor mixing ratio for $\pm$6 hours from the TPV's closest point to Summit.

3.2.2 Observed Structure

Compositing the variety of cases used in this study is an illustrative way to consider the general properties of TPVs and understand the similarities between cases. In this study, these composites are based on the ERA5 model, which is influenced directly by radiosondes launched from Summit, providing a method to study how observations support or oppose TPV characteristics as defined in literature by simulations. This section will discuss composites of temperature, relative humidity, and u and v wind, while subsequent sections with discuss composites of radiative properties based on the amplitude changes of the TPVs.

Time-height cross sections through all 40 selected TPVs over a $\pm$24 hour period show anomalously warm temperatures above the composite tropopause and anomalously cool temperatures below the composite tropopause (Figure 3.12a). The strongest anomalies, both positive and negative, are found between -3 and 0 hours from closest passage, coincident with the lowest point on composite tropopause. The lowest magnitude of anomalous temperature exists as early as -21 hours and as late as +18 hours. Positive anomalies reach +3 K and negative anomalies reach about -2.5 K. This anomalous temperature structure was also noted in the case study (section 3.1, figure 3.4b) as well as Cavallo and Hakim (2010).

Similar time-height cross sections show mostly anomalously dry values of relative humidity near the composite tropopause (figure 3.12b). The negative anomalies are the greatest just above the tropopause, at values near -30% just before 0 hours. Negative anomalies of around -5% exist as early as -18 hours and as late as +21 hours, similar to the anomalous temperature findings. The negative anomalies extend from about 2 km AGL to nearly 7 km AGL in the vertical, with small positive relative humidity anomalies existing for a short time before the TPV is closest to Summit (i.e. earlier than -24 hours, up to -6 hours, values reaching about +10%). A notable feature in both the temperature and relative humidity time-height cross section anomaly composites is the downward sloping signature after the TPV's passage. The leading edge of the TPV does not show such a feature during

its approach, however the fact that this is evident after the TPV's passage implies that the vortex is modifying its environment. This feature was also noted in the case study when evaluating the relative humidity time-height cross section (ref. section 3.1, figure 3.5).

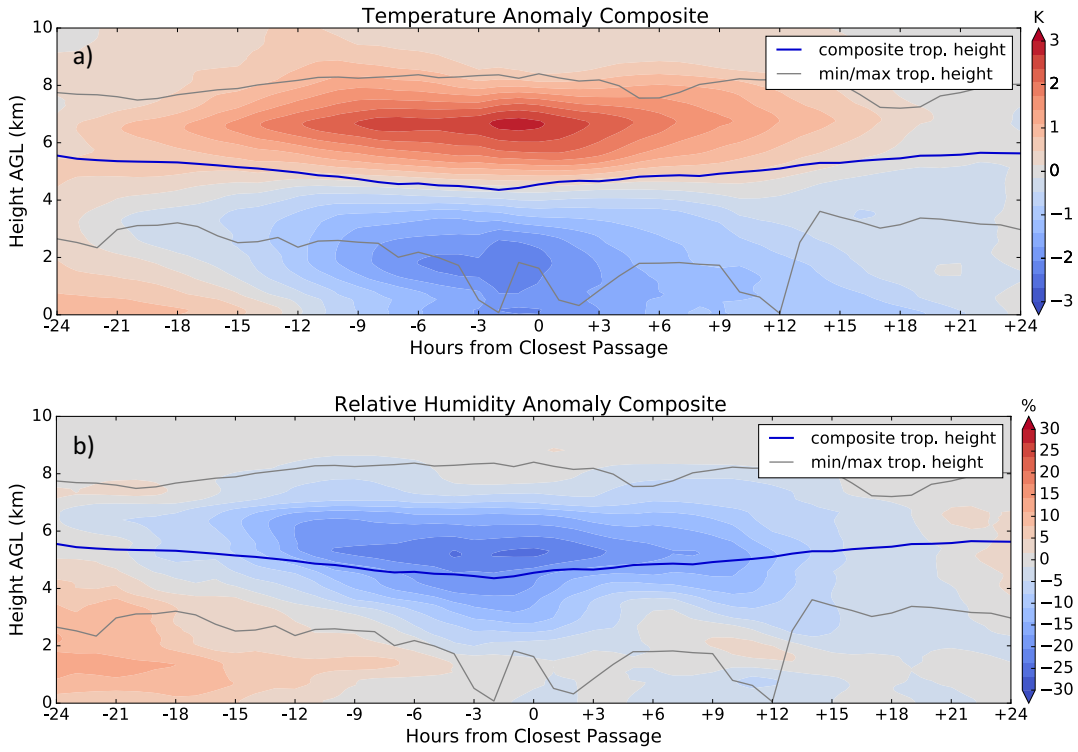


Figure 3.12: Composite time-height cross section of anomalous a) temperature (K) and b) relative humidity (%) for $\pm$24 hours of a TPV's closest passage to Summit, including TPVs passing Summit during the time period from March 2012 to October 2014.

Composite anomalies of u- and v-winds are also analyzed to consider TPV structure. While the u-wind anomaly composite shows very little in the way of an anomalous wind field around the TPV, anomalous v-winds are clearly cyclonic around the vortex core (figure 3.13). The u-wind anomaly composite likely shows only very weak anomalies due to the TPVs being embedded in a mean westerly background flow, as many of the TPVs considered in this composite move from west to east across Summit. The v-wind anomaly composite shows very strong southerly winds starting before the -24 hour mark and extending to the -3 hour mark (figure 3.13a). The strongest southerly wind anomalies are

centered on the tropopause between -22 hours and -16 hours with anomalies greater than 6 m s^{-1}. For TPVs moving from west to east across Summit, this implies that an anomalously strong southerly wind is present on the east side of the vortex as early as 24 hours before its core reaches Summit. The v-wind composite may also imply that on average, Summit is already within the last closed contour of the TPV as early as 24 hours before the core reaches Summit. This may be a consequence of several very large TPVs in the dataset, or several very slow moving TPVs. Alternatively, for the same west to east moving TPVs, the strongest negative anomalies (northerly winds) exist on the west side (i.e. after the TPV has passed), however the negative anomalies are not as strong or long-lived as the positive. The anomalous northerly winds centered on the tropopause only reach values around -3 m s^{-1} and only exist between the hours of +6 and +21, on average. Weak positive anomalies of v-wind also exist near the composite TPV's core, however these small positive anomalies (near +2 m s^{-1}) exist above the tropopause rather than centered on it. The presence of exceptionally strong positive anomalies before the TPV's passage may be due in part to the presence of significant ridging before a TPV's passage, however, in order to diagnose this a case-by-case synoptic overview would need to be considered.

In general, results of composite temperature, relative humidity, u- and v-winds agree with results presented in Cavallo and Hakim (2010) regarding the composite structure of TPVs. Both sources show anomalously warm temperatures above the tropopause and anomalously cool temperatures below, however Cavallo and Hakim (2010) show stronger anomalies with values reaching +5.5 K and -8.5 K. While relative humidity anomalies from the results here show agreement with Cavallo and Hakim (2010) in terms of anomalously dry air above the tropopause, there is not an indication of anomalous moisture present near the surface below the TPV's core as in figure 1.1d (from Cavallo and Hakim (2010)). This may be influenced by the lower moisture of the atmosphere above Summit in comparison to other Arctic locations (e.g. figures 1.6, 1.15), however a general increase in moisture

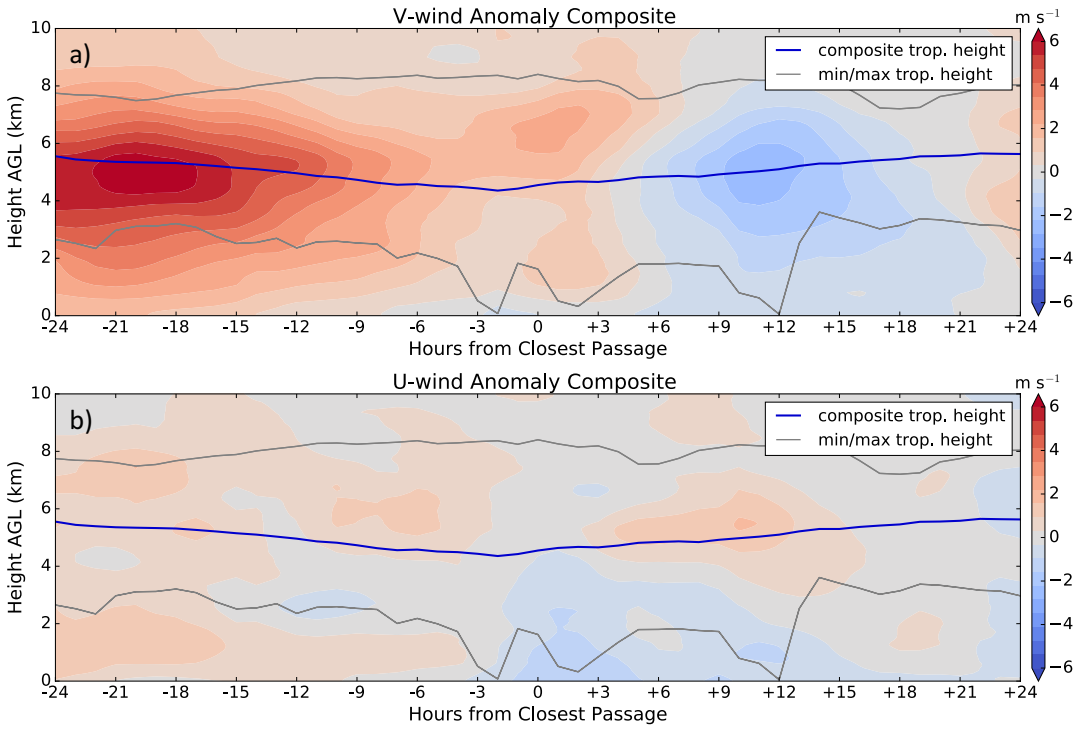


Figure 3.13: As in figure 3.12 with anomalous a) v-wind (m s^{-1}) and b) u-wind (m s^{-1}).

near the surface would still be expected, even if small, based on simulations done in previous studies of TPVs. Anomalous moisture does appear to exist during early hours in the composite from our study which, in the case of a west to east moving TPV, would agree somewhat with the anomalous moisture present in midlevels on the east side of the composite TPV from figure 1.1d. Further analysis would be needed to determine whether this anomalous moisture is in fact due to the presence of the TPV. Cavallo and Hakim (2010) do not discuss u-wind composites since they consider only west-east cross sections, however their results do show cyclonic motion around the core of the vortex in terms of v-wind, in agreement with the results presented here. Two differences, however, are the strength of the anomalies and the symmetry of the anomalies. Figure 1.1b shows a symmetric cyclonic structure, with equal anomalous winds on both sides of the vortex core reaching values close to ± 16 m s^{-1}. The results from figure 3.13a do not show symmetric northerly and southerly winds, and the anomalies are less than half the value of the anomalies from figure

1.1b. Figure 1.1b also does not show an anomalous southerly wind component above the tropopause at the location of the core as 3.13a does. The causes for these differences may be due to the inconsistent nature of the movement of TPVs over Summit in the observed cases or the obscure shapes of some TPVs, leading to ambiguities in the composite structure of wind fields. It is also important to note that the sample used for the composites in this study is small (40 TPVs) and included more weak TPVs than strong TPVs, likely reducing the strength of the expected signal.

3.2.3 Observed Radiative Properties

Composites of radiative heating rate (RHR) properties were only created for the clear-sky cases due to the inconsistent nature of the clouds in and around TPVs in the 40 cases compiled and lack of cloud data available for 25% of cases. The composites were broken down into those for strengthening cases and those for weakening cases based on the average hourly amplitude change over the $\pm$6 hour period from the TPV's closest passage. For this analysis, there are 17 cases included in the strengthening cases composites and 22 included in the weakening cases composites. The average hourly amplitude change for the 17 strengthening cases is +0.25 K hr^{-1} and for the weakening cases is -0.28 K hr^{-1}. One case maintained an average hourly amplitude change of 0 and was not included in either composite. To better understand the breakdown of RHR contribution over a large range of cases, composites were created based on experiments 2 (clear-sky), 5 (water vapor perturbation contribution), and 6 (temperature perturbation contribution) (similar to figure 3.9 for the case study).

3.2.3.1 Strengthening Cases

Beginning with the strengthening cases, RHR time-height cross sections show radiative cooling as strong as -2 K day^{-1} in all three clear-sky experiments, mainly confined to near the surface (figure 3.14). The largest cooling is in the clear-sky and water vapor contribution

cases (figure 3.14a and b). Fluctuations in heating rate exist throughout the time period, mostly in the clear-sky case and water vapor contribution case, with the RHR values due to temperature perturbations remaining mostly constant over the $\pm$24 hour time period. This result indicates that water vapor perturbations are the most influential component of the clear-sky RHR. Alternatively, there is a region of stronger cooling in the temperature perturbations case above the tropopause between -12 hours and +3 hours (figure 3.14c) which is not seen in the water vapor perturbations profile. This cooling could be an artifact of cooling from mean water vapor at 6 km, since there is a band of cooling at 6 km in the water vapor perturbations case near the edges of the $\pm$24 hour period (figure 3.14b), which would influence the mean at that level.

Heating rate anomaly composites provide a different perspective to allow for the analysis the influence of temperature and water vapor on TPVs. For strengthening TPVs, the clear-sky anomaly composite shows positive anomalies of RHR on and around the tropopause for the entire time period considered, however the largest anomalies are found in the -6 hours to +9 hours time period (figure 3.15a). Between -3 hours and +3 hours, these strong positive anomalies extend downward to nearly 2 km, and extend upward to 7 km, nearly 3 km above the tropopause. Negative anomalies of RHR are located near the surface before 0 hours and above the tropopause in a band near 7 km. When considering only the water vapor perturbation contributions to RHR, positive anomalies are found mostly above the tropopause, starting as early as -12 hours and extending to +15 hours (figure 3.15b). This is likely due to the larger relative change in water vapor concentration above the tropopause. The strong positive anomalies shift downward and fall below the tropopause at +6 hours, eventually approaching the surface by +18 hours. The sloping nature of the water vapor RHR anomaly composite is similar to the sloping feature after the TPV's passage in the relative humidity analysis for the case study (figure 3.5) and the relative humidity composite (figure 3.12b). As in the RHR composites for strengthening

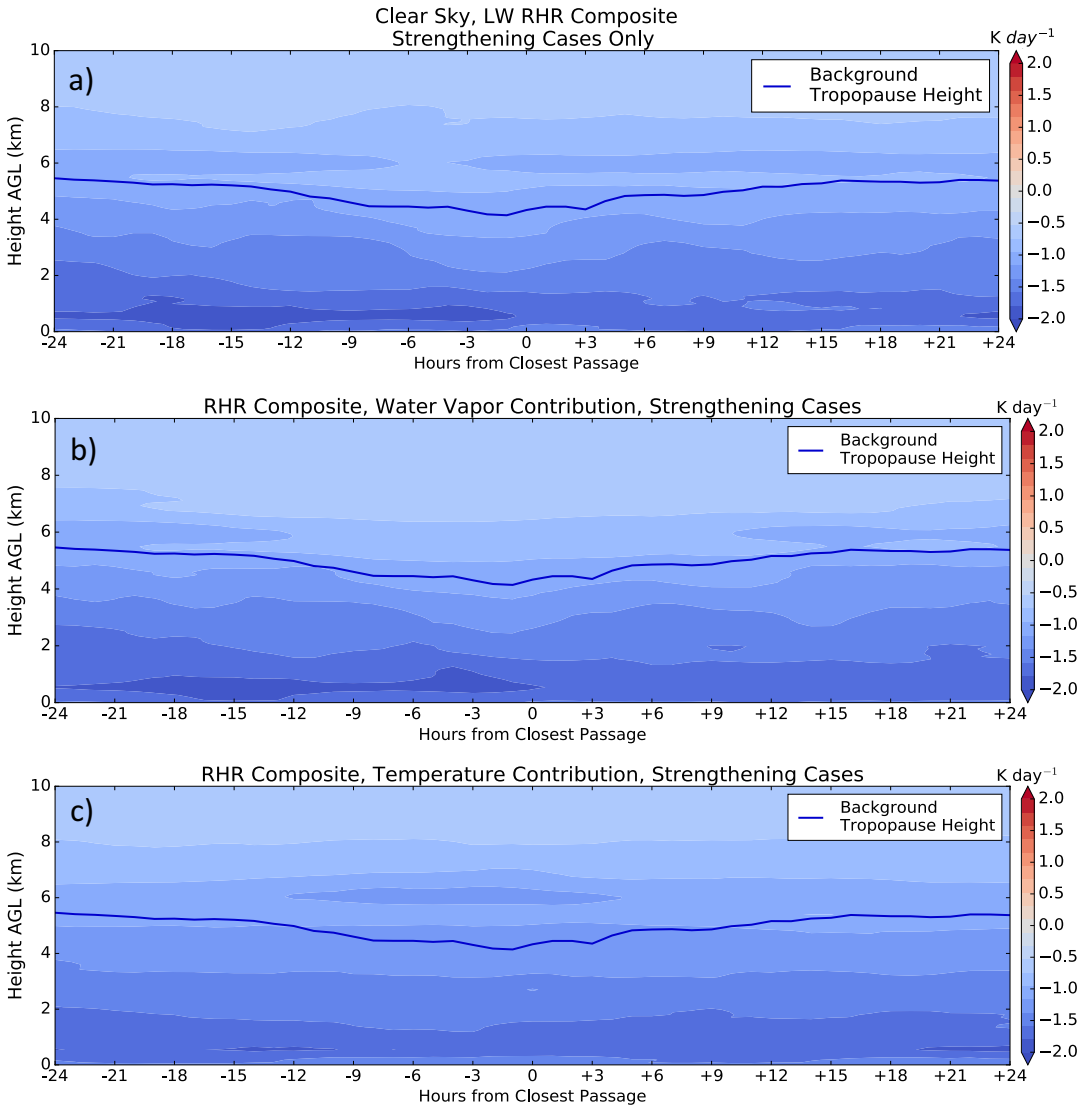


Figure 3.14: Composite time-height cross section of RHR for a) clear-sky (experiment 2), b) water vapor contributions (experiment 5), and c) temperature contributions (experiment 6) based on $\pm$24 hours of a TPV's closest passage considering only TPVs that strengthened on average over a $\pm$6 hour period.

cases, variability in heating rate anomalies with time is not as high in the temperature perturbation contribution composite (figure 3.15c). Negative anomalies are found above the tropopause for the entire period, with the strongest of those existing from -6 hours to 0

hours. Positive anomalies, weaker than those found in the clear-sky and water vapor contribution RHR anomaly cases, exist below the tropopause at all times. As opposed to the clear-sky and water vapor contribution RHR anomaly cases, the tropopause in the temperature perturbation RHR composite acts almost as a dividing line between positive anomalies and negative anomalies. While negative anomalies exist above the tropopause in this composite, these anomalies are weaker in comparison to stronger positive anomalies from the water vapor perturbation composite, which leads to the positive anomalies present in much of the time-height cross section of the clear-sky anomaly composite.

The results for composite anomalous RHR for strengthening cases agrees with expected results. In the clear-sky and water vapor contribution to RHR cases, RHR anomalies are negative near the surface throughout much of the time leading up to the TPV's 0 hour, however, positive anomalies grow in strength at and above the tropopause as the TPV approaches Summit. Recalling equation 1.2, positive vertical gradients in heating rate across the tropopause provide a positive contribution to EPV tendency. The water vapor composite of RHR shows an increased vertical gradient in RHR across the tropopause throughout the TPV's center as compared to the "outsides" of the vortex, which provides a positive contribution to EPV creation, acting to strengthen the vortex. The temperature contribution RHR anomalies show the opposite, i.e., that there is a negative vertical gradient in heating rate, which acts to weaken EPV tendency and weaken the vortex. From the clear-sky composite, it is obvious that the water vapor contribution has a larger effect on the total clear-sky RHR values than temperature, allowing these TPVs to strengthen due to clear-sky water vapor effects rather than weaken by clear-sky temperature effects.

Time height cross sections of composite EPV tendency anomalies show more variability than the RHR cross sections for strengthening cases. There are, however, notable features in these composites that aid in our understanding of TPVs. In the clear-sky EPV anomaly composite, positive anomalies exist just below the tropopause between -9 and +6 hours (figure 3.16a). This is a notable feature in the clear-sky case, since at many times outside

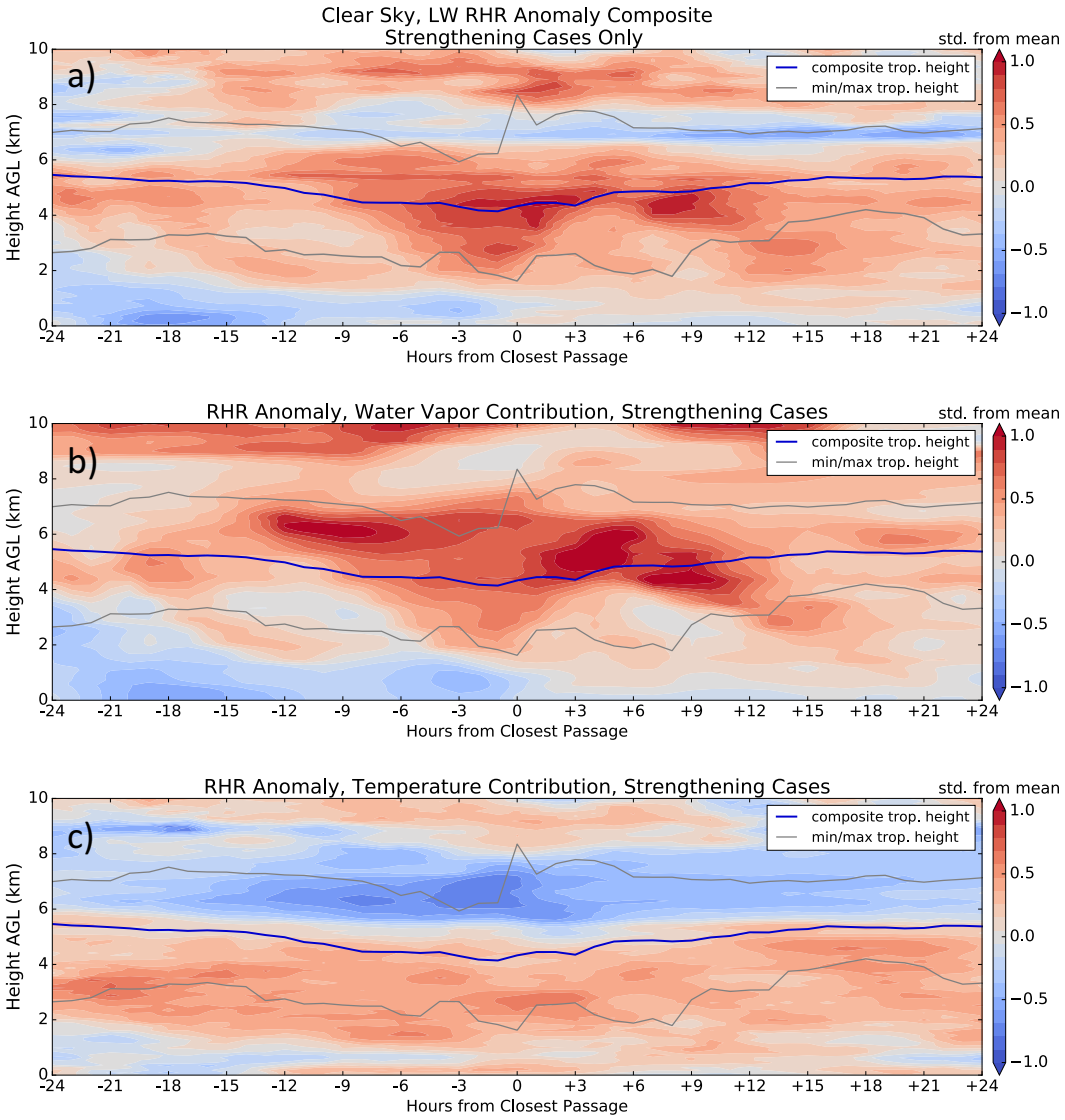


Figure 3.15: Composite time-height cross section of anomalous RHR for a) clear-sky (experiment 2), b) water vapor contributions (experiment 5), and c) temperature contributions (experiment 6) based on $\pm$24 hours of a TPV's closest passage considering only TPVs that strengthened on average over a $\pm$6 hour period. Anomalies are measured in standard deviations from the mean heating rate.

of this -9 to +6 time period, the EPV tendency anomaly is negative on the tropopause. This signal becomes more clear when considering the composite anomalies of EPV tendency due to water vapor only, in which the features described for the clear-sky case are amplified

(figure 3.16b). In this case, positive EPV anomalies extend from the tropopause to about 1 km between the time period from -9 to +9 hours, with negative or neutral anomalies elsewhere along the tropopause. While the composite for the temperature-only contribution to EPV tendency has fewer distinct areas of positive or negative anomalies, a close analysis shows that positive anomalies exist in the same region as they do for the clear-sky and water vapor only cases, i.e., from -9 to +3 just below the tropopause (figure 3.16c). The outer time periods also have similar features to the clear-sky and water vapor only cases, with negative anomalies near the tropopause at all times outside of the specified time period.

Results for anomalous EPV tendency for strengthening TPVs complement what is expected for strengthening TPVs. Since, in general, higher values of EPV exist in the stratosphere as compared to the troposphere, positive anomalies of EPV tendency below the tropopause act to strengthen TPVs. This would increase PV in the troposphere beneath the TPV's core. The results presented show this feature, with the largest signal existing in the water vapor contribution case (figure 3.16b). Strong positive anomalies exist directly below the tropopause and extend downward under the TPV's core. This implies that the water vapor contribution is acting to enhance the EPV below the tropopause and strengthen the vortex. The clear-sky experiment for composite anomalous EPV tendency also shows this signal, however the anomalies are not as strong. An important feature to note is the general negative nature of anomalies on the tropopause for all times outside of the vortex "core". The fact that positive anomalies only exist within regions that are more representative of the core implies that more EPV is being created in the center of the vortex than on the outside, which would lead to a strengthening vortex.

3.2.3.2 Weakening Cases

Features in the RHR composites for weakening cases are similar to those in the RHR composites for strengthening cases. As in the RHR composites for strengthening cases, RHR

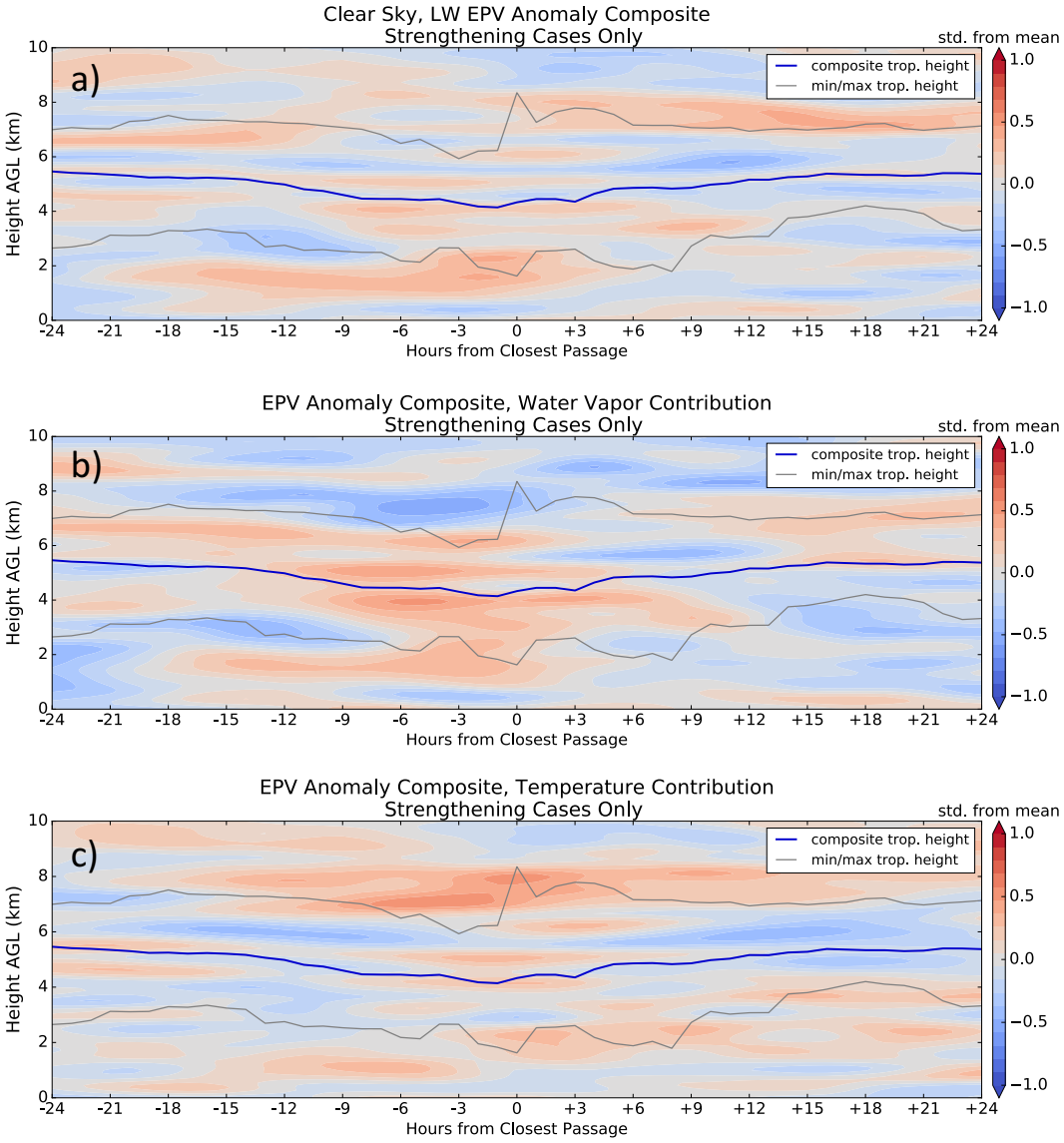


Figure 3.16: Composite time-height cross section of anomalous EPV tendency for a) clear-sky (experiment 2), b) water vapor contributions (experiment 5), and c) temperature contributions (experiment 6) based on $\pm$24 hours of a TPV's closest passage considering only TPVs that strengthened on average over a $\pm$6 hour period. Anomalies are measured in standard deviations from the mean EPV tendency, measured in PVU day^{-1}.

composites for weakening cases show a similar range of RHR values (i.e., minimum values around -2 K day^{-1}) and the largest cooling near the surface (figure 3.17). In addition,

the majority of heating rate variability is seen in the clear-sky and water vapor contribution composites, implying once again that water vapor is the more influential perturbation between that and temperature. Another similarity is the area of increased cooling above the tropopause in the temperature perturbations composite. This cooling is above the tropopause between the times of -9 hours and +6 hours, at values between -1 K day^{-1} and -1.5 K day^{-1} (figure 3.17c). The variability in RHR in the temperature perturbation composite for the weakening cases is slightly higher than that of the temperature perturbation composite for the strengthening cases, however the vertical gradient in RHR is still mostly representative the background water vapor profile used in this experiment.

While features from the RHR composites of weakening cases show many subtle similarities to the RHR composites for strengthening cases, the RHR anomaly composites for the weakening cases show some of the more notable differences. In the clear-sky composite for weakening cases, the largest signal is an area of positive RHR anomalies that exist just below the tropopause from -13 hours to about +3 hours (figure 3.18a). These anomalies reach values at or above +1 standard deviation away from the mean value of the RHR. Much of this anomalously positive area comes from water vapor perturbations, which can be seen in the composite for RHR from water vapor. Large positive anomalies in RHR exist between -3 hours and 0 hours just below the tropopause in the water vapor contribution composite, with positive, but weaker, anomalies extending just above the tropopause at this time (figure 3.18b). Another short time period of positive anomalies exists above the tropopause at -12 hours. Other than the time from -12 hours to +3 where these strong positive anomalies exist, most of the other signals in this time-height cross section are weak. The composite of RHR anomaly from temperature contributions for the weakening cases shows a similar signal to that of the strengthening cases, with negative anomalies above the tropopause and positive below (figure 3.18c). The difference in the weakening cases, however, is that this signal is much stronger, with anomalies greater than ± 1 standard deviation from the mean. The negative anomalies exist from about -9 hours to +9 hours, almost

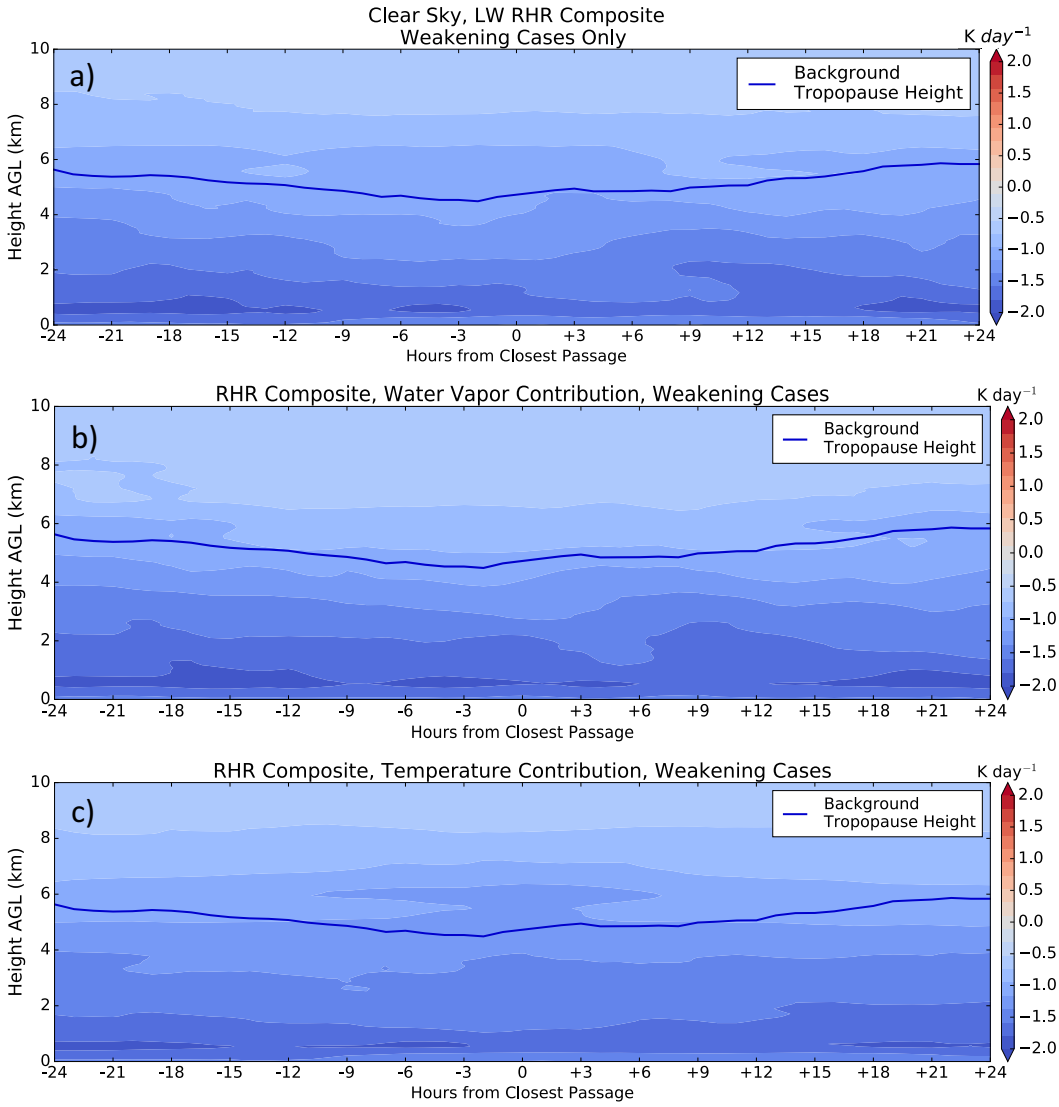


Figure 3.17: As in figure 3.14, but considering only TPVs that weakened on average over a $\pm$6 hour period.

exactly centered on the time of the TPVs closest passage, while the positive anomalies are offset to the earlier hours, extending from about -12 hours to 0 hours. The negative anomalies exist less than 1 km above the tropopause and the positive anomalies exist about 1 km below the tropopause, extending down to about 1.5 km above the surface.

Results from the weakening cases of composite anomalous RHR also agree with our understanding of TPVs from literature. As described in section 3.2.3.1, the vertical gradient

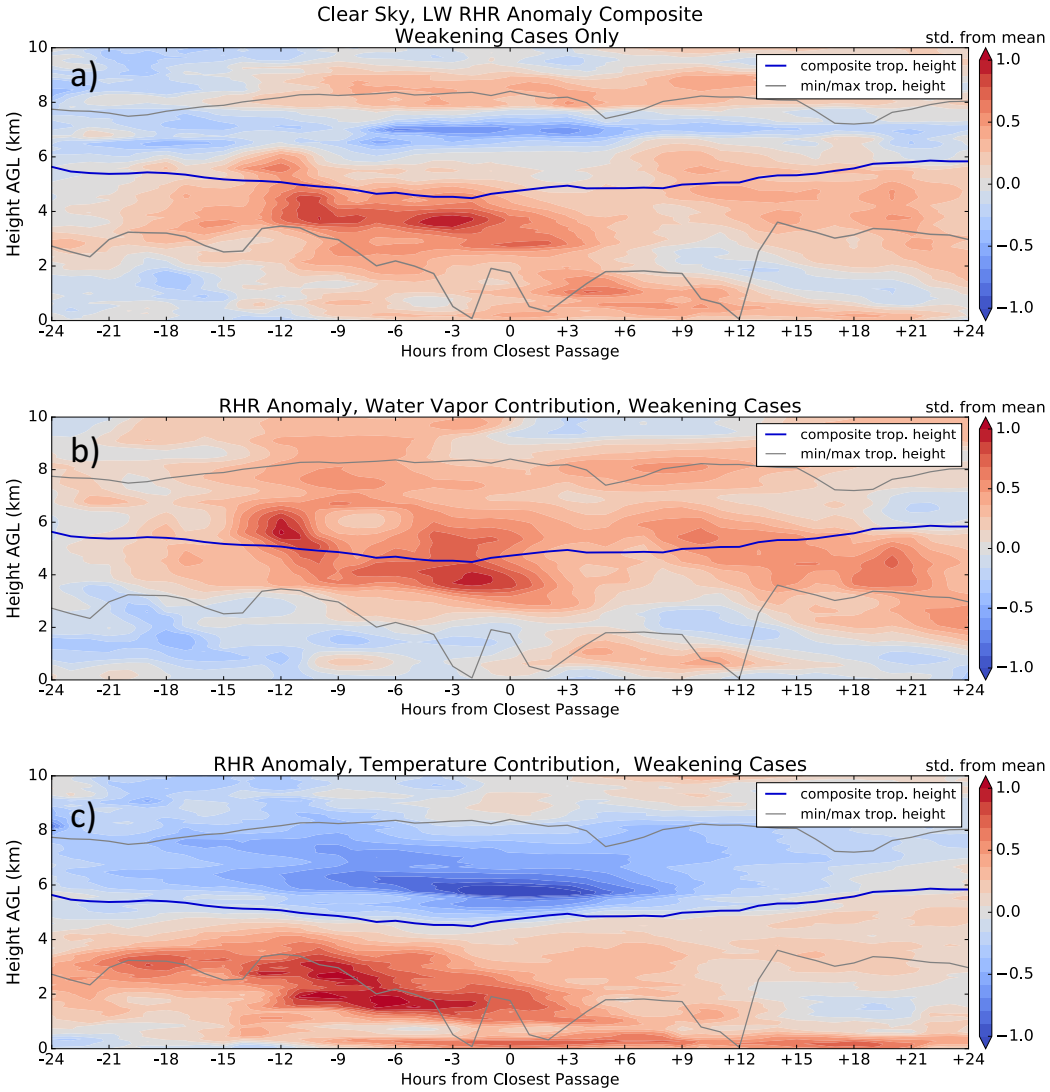


Figure 3.18: As in figure 3.15, but considering only TPVs that weakened on average over a ± 6 hour period.

of RHR across the tropopause is important for EPV tendency. In the water vapor contribution case, there is a positive vertical gradient of RHR from the surface to the maximum positive anomalous RHR which exists below the tropopause. However, since this maximum positive anomaly exists below the tropopause, the vertical gradient in RHR across the tropopause is negative. Above the tropopause, RHR anomalies are decreasing vertically even though they remain positive in the stratosphere. The difference in this case,

as compared to the strengthening cases, is that the change in this vertical gradient within the core compared to the outside is not as obvious. The negative anomalies present above the tropopause in the RHR anomaly composite from temperature are stronger than those noted in the strengthening case. The temperature contribution to RHR always acts to lower EPV tendency since the vertical gradient in RHR is negative across the tropopause. In the weakening cases presented, the temperature contribution is an important factor in opposing any positive EPV tendency that water vapor creates. Ultimately, combining the two effects and considering the clear-sky RHR anomalies, there is a negative vertical gradient in RHR across the tropopause which acts to weaken the vortex.

As in the strengthening cases, anomalous EPV tendency composites for weakening TPVs show slightly more variability over the time period analyzed. The clear-sky case of anomalous EPV tendency offers no obvious signal, however close evaluation of the values at the tropopause show slightly negative anomalies for most of the time period, with more notable negative anomalies between -9 and -2 hours (figure 3.19a). Anomalous EPV tendency in the water vapor contribution case is more distinct, with positive values at or above the tropopause from -12 hours to +12 hours (figure 3.19b). These positive values are between 0.5 and 1 standard deviation from the mean. Another area of similar-magnitude positive anomalies exists between -3 and 0 hours, however this area is 1-2 km below the tropopause. Anomalies of EPV tendency due to the temperature contribution have negative values on the tropopause during most of the time period, and larger positive anomalies existing only at much higher altitudes, far above the background tropopause (figure 3.19c). Other fluctuations in anomalous EPV tendency during the time period are minor, and the focus on EPV tendency anomaly at or near the tropopause remains the most important aspect for consideration.

Considering the EPV tendency anomalies shown via compositing all weakening cases, signals are not as obvious as those found in the strengthening cases. Some notable features may be influential in the weakening of TPVs, such as the positive anomalous EPV tendency

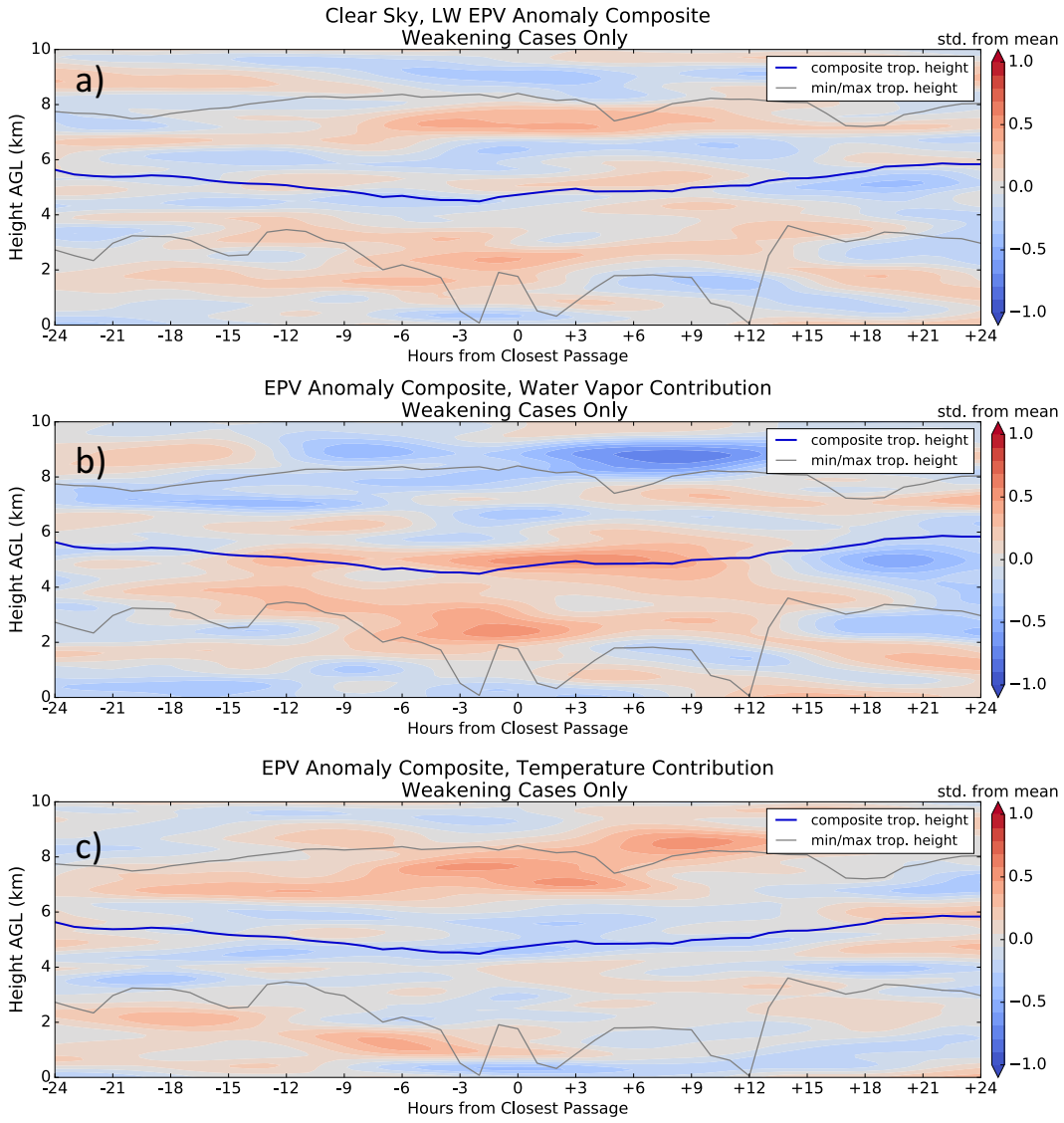


Figure 3.19: As in figure 3.16, but considering only TPVs that weakened on average over a $\pm$6 hour period.

above the tropopause in the water water vapor contribution to EPV tendency case. While positive anomalies of EPV tendency below the tropopause in the center of the vortex would act to increase the amplitude of a TPV, increasing EPV above the tropopause would only act to neutralize an existing TPV since above-tropopause values of EPV are already expected to be higher than below the TPV. It is also important to note that negative anomalies, while

small, exist at the tropopause in the temperature contribution anomaly composite. Negative anomalous EPV tendency at the tropopause would be expected to weaken a TPV as well as positive anomalous EPV tendency above the tropopause. The negative values at the tropopause are small in the clear-sky case and, without further analysis, no explicit conclusions can be drawn as to whether or not the magnitude of these anomalies are influential in weakening TPVs in general.

3.2.4 Cloud Properties

Based on literature, cloud properties associated with TPVs are generally not well known due to the sparse nature of previously existing observations of TPVs. For this study, the 30 cases with cloud profile observations are too few and too variable to draw definitive conclusions from composites. While cloud properties were not included in composites, cloud microphysics and cloud influences on radiative properties can be considered through other methods. Here, the idea of how cloud microphysics may be related to the size, strength, or amplitude changes of TPVs is considered by investigating the column-integrated LWP and IWP surrounding the TPV's core. Focusing attention to ± 6 hours from the TPV's closest point to Summit, the average IWP and average LWP do not appear to have a strong correlation with the size or strength of TPVs, however TPVs smaller than 150 km in radius tend to have higher cloud water path values than TPVs larger than 150 in radius (figure 3.20). The two largest TPVs in the dataset also have cloud water path values at the higher end of the spectrum, with average IWP values above 18 g m^{-2} and LWP values above 8 g m^{-2}, both of which are higher values than most TPVs larger than 150 km in radius. When considering average IWP, the majority of TPVs with IWP values greater than 15 g m^{-2} are weakening TPVs, and the strengthening TPVs, other than the two above 300 km in radius, all have relatively small IWP values in comparison to the weakening cases (figure 3.20a). The average value of average column-integrated IWP for strengthening TPVs is 12.3 g m^{-2} while for weakening cases it is 45.1 g m^{-2}. The average LWP for the TPVs considered offers similar

results to the average IWP, with the majority of high-LWP cases being weakening cases. Six out of eight TPVs with LWP greater than 7 g m^{-2} are weakening cases (figure 3.20b). Most of the TPVs considered have zero or near-zero LWP values. The average value of average column-integrated LWP for strengthening TPVs is 1.9 g m^{-2} while for weakening cases it is 13.5 g m^{-2}, however it is important to note that a wide range of LWP averages exist in each category. LWP average values for strengthening TPVs range from 0 to 9 g m^{-2}, and values for weakening TPVs range from 0 to 102 g m^{-2}. LWP values are highly variable in the dataset because all seasons are included and LWP values are much higher in the summer months. The case study described in section 3.1 is the TPV with radius near 345 km and amplitude near 16 K. Since the case study is a July TPV and liquid water was notably present during its evolution, it is not surprising that this TPV is on the higher end of the spectrum of average LWP values. The values for average IWP associated with this TPV are moderate compared to the full dataset of TPVs, with an average 12-hour value between 15-18 g m^{-2}.

Many of the variations in LWP and IWP values associated with TPVs are likely due to seasonal variations in temperature and moisture in the environment at Summit. Based on the averaged column-integrated LWP and IWP for the times surrounding the TPV's closest point, it is difficult to deduce whether cloud water is related to TPV amplitude changes, however it does appear that smaller TPVs and/or weakening TPVs tend to contain more cloud water. It is also important to note that the location of the cloud vertically within a TPV is theorized to be important for amplitude changes, however this information is not provided through the use of column-integrated LWP and IWP. While it may be difficult to composite cloud properties due to their complexity and uniqueness between cases, these cloud microphysical properties can be used to analyze how cloud water affects radiative properties in the central regions of the TPVs as compared to the clear-sky counterpart.

Typically, TPVs have similar features and a common structure, however radiative properties can vary greatly between cases due to clouds and other environmental influences.

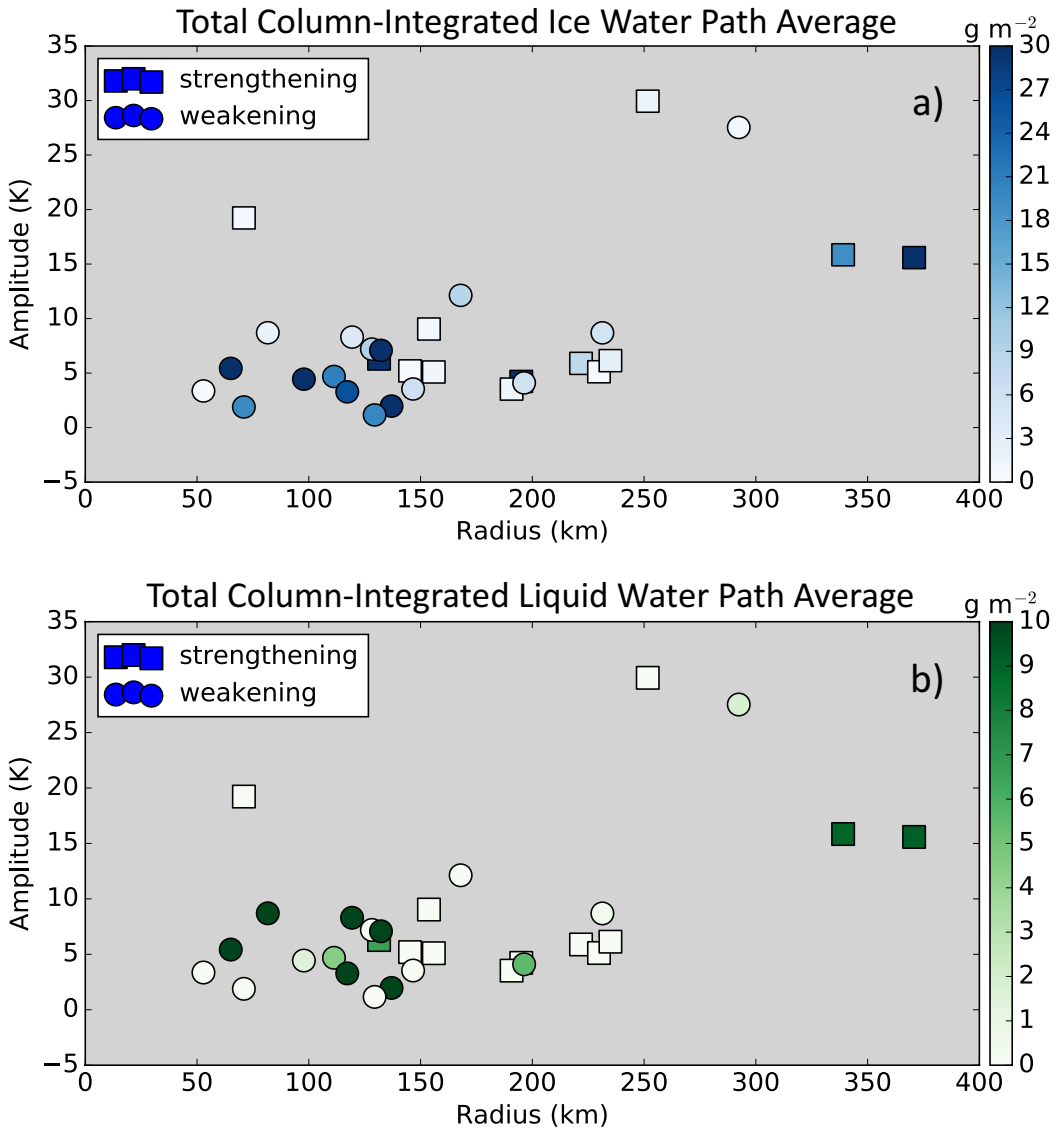


Figure 3.20: Scatter plot showing size, amplitude, and cloud microphysical properties for the TPVs in the analysis with cloud data available. The size and amplitude of each TPV are taken at the time of the TPV's closest point to Summit. Squares represent TPVs that strengthened, on average, over a 12-hour period surrounding the TPV's closest passage to Summit, and circles represent TPVs that weakened, on average, over the 12-hour period. Colors represent the average 12-hour column integrated a) ice water path and b) liquid water path for $\pm$6 hours from the TPV's closest point to Summit.

For example, in many of the cases studied here, the average clear-sky RHR anomalies are positive on the tropopause for the ± 6 hour period around the TPV's closest passage (figure 3.21a). The majority of cases (31 out of 40) have positive average RHR anomalies on the tropopause, while 2 are near neutral and 7 have negative anomalies. All 7 of the TPVs with negative average clear-sky RHR anomalies on the tropopause are cases that weakened on average over the 12 hour period. For clear-sky considerations only, RHR anomalies on the tropopause do not show any clear correlation to the size or amplitude of the TPV.

When considering clouds (i.e., the all-sky case), negative average anomalies on the tropopause are much more prominent among the cases studied here (figure 3.21b). Many cases of positive average RHR anomalies in the clear-sky case become cases of negative average RHR anomalies in the all-sky case, implying that clouds, of some type, must exist at the tropopause. The existence of clouds at the tropopause increases the radiative cooling, therefore lowering the RHR anomalies on the tropopause. Clouds located at tropopause level have a net cooling effect, as evident when considering the all-sky anomalies in the absence of the clear-sky RHR contribution (figure 3.21c). Many of the cases maintain positive anomalies, however the cases that become negative in the all sky case are mostly weakening cases with the exception of 3 strengthening cases. In addition, most of the cases containing negative anomalies in the clear-sky case maintained their negative nature but with an increased magnitude. It is possible that the presence of clouds in these cases modified the environment and influenced the RHR anomaly even in the clear-sky case. While again, no correlation is notable between RHR anomalies and size or amplitude, it does appear that many of the TPVs with the strongest negative anomalies are on the smaller, weaker end of the spectrum, coinciding with cases of larger cloud water path values. It cannot be concluded from this, however, that smaller or weaker TPVs are associated with stronger cooling in their center, as these anomalies may only be a product of the random nature of clouds present in the vicinity of these specific TPVs.

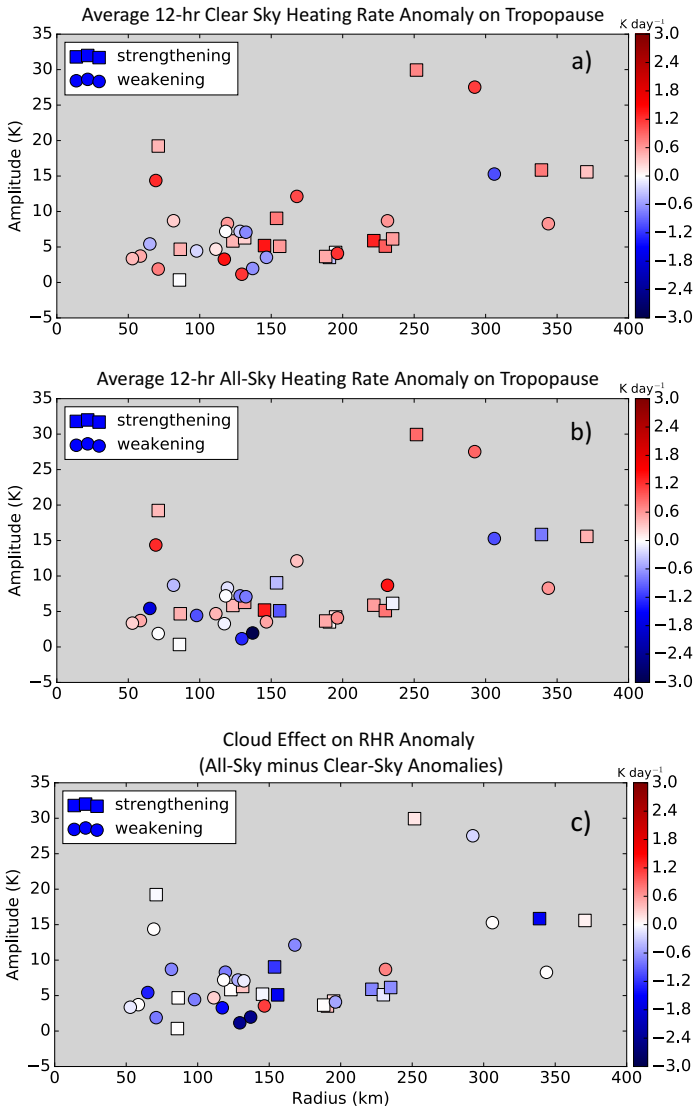


Figure 3.21: Scatter plot showing size, amplitude, and average 12-hour heating rate anomaly on the tropopause for all TPVs included in the analysis. The size and amplitude of each TPV are taken at the time of the TPV's closest point to Summit. Squares represent TPVs that strengthened, on average, over the 12-hour period, and circles represent TPVs that weakened, on average, over the 12-hour period. Colors represent the average 12-hour heating rate anomaly on the tropopause for a) the clear-sky case and b) the all-sky case in terms of standard deviations from the mean. Panel c) shows the difference in the anomalies between b) and a). For cases with no cloud data available, the clear-sky anomaly averages were used for the both the clear-sky and the all-sky cases.

Chapter 4

Summary and Conclusions

Tropopause polar vortices have gained significant interest in recent years due to their ever-growing importance in meteorology. TPVs have been shown to aid in the formation of surface cyclones, which then lead to other events such as the thinning of sea ice, or in lower latitudes, extreme weather. Previous studies have used simulations to evaluate structure, amplitude changes, and radiative characteristics of TPVs, while observations of these polar features have remained sparse and unstudied. This study combined reanalysis data with ground based cloud observing systems located at the Summit of Greenland to analyze the same previously studied features but from a unique perspective.

Given that previous literature showed the importance of water vapor gradients and cloud top radiative cooling in the intensification of TPVs, it was hypothesized that the water vapor gradient induced by TPVs, as well as cloud top radiative cooling, would aid in the intensification of TPVs. To begin the investigation, a case study was chosen with a direct path over Summit to fully utilize the cloud observatory located there and investigate the cloud and radiative scene associated with the case. An in-depth analysis of radiative features of this TPV showed radiative heating rate anomalies were positive in and around the TPV's core for the clear-sky case, with a weak vertical RHR gradient likely not contributing significantly to strengthening the vortex. The all-sky case, however, revealed that strong radiative cooling from clouds was present at the tropopause in the TPVs center. This TPV had an overall strengthening trend on average, and since clear-sky RHR values did not suggest strong intensification, this strengthening was attributed to cloud-top longwave radiative cooling in the TPV's core. Additionally, clear-sky and all-sky RHR values were in general agreement with previous studies of Arctic RHR profiles such as those shown in Turner et al. (2018). Clear-sky RHR values in the case study (as well as the composites)

were between -1 K day^{-1} and -3 K day^{-1}. When clouds were included in RHR calculations, RHR values were considerably smaller, with values exceeding -5 K day^{-1}. Cooling in ice clouds was fairly evenly distributed between cloud base and cloud top, in agreement with the results presented for single-layer ice-only clouds in Turner et al. (2018) (ref. figure 1.21). Liquid layers in the case study analysis were mostly located at cloud top. However, the general profile of enhanced cooling at cloud top and slight warming below cloud base for liquid-only clouds agrees with RHR profiles from previous literature (e.g., Turner et al. (2018), ref. figure 1.22).

Composite results allowed a consideration of how the results from the case study compare to all cases in general. Anomalous temperature, relative humidity, and winds were composited in time-height cross sections among the 40 cases available. Temperature composites showed positive (negative) anomalies above (below) the composite tropopause, in agreement with composites presented by Cavallo and Hakim (2010). Relative humidity composite results showed negative anomalies above the tropopause, but no significant anomalies near the surface, which does not agree with the positive RH anomalies found near the surface in composites done by Cavallo and Hakim (2010). This may be due to outside environmental factors, such as advection of dry air at low levels in many of the cases composited which acts to dry out any abnormal moisture induced by the TPV at low levels. This may also be due to the relatively dry nature of Summit in general during all seasons (see section 1.3.3), and Summit's high altitude making it difficult to advect moisture in. V-wind composites were presented by Cavallo and Hakim (2010) as well, showing a cyclonic wind field, which is also what was found in the observed composites, however the positive and negative anomalies around the center were not equal in magnitude. The u-wind composite did not show a specific signal, likely due to the primarily west to east movement of TPVs in the dataset.

Composite results for RHR and EPV tendency were broken down by cases that were strengthening on average and those weakening on average over a 12 hour period. The composites of strengthening cases provide complementary ideas to previous literature. Considering the RHR anomalies, Cavallo and Hakim (2013) suggests that anomalous cooling just below the tropopause and heating above (figure 1.3d) are present due to the water vapor gradient in the TPV's core, however our results show that anomalous heating is present in a much larger area surrounding the core with very little anomalous cooling. While the cooling was small, the general trend in the strengthening cases was the positive vertical gradient in RHR across the tropopause, leading to a positive contribution to EPV tendency. EPV tendency composites for the strengthening cases do show areas along the tropopause with positive EPV tendencies, which is expected for strengthening TPVs. RHR composites for weakening cases show a similar scene with large areas of positive anomalies near the tropopause. In the weakening cases, there is an obvious difference in the location of the strongest positive anomalies as compared to the RHR composites of the strengthening cases. The weakening composites revealed maximum positive anomalies in RHR below the tropopause, creating a negative vertical gradient in RHR across the tropopause, contributing a negative component to EPV tendency. Composites of EPV tendency for weakening cases show slightly negative values on the tropopause for the clear-sky total. The water vapor contribution to this composite presents a positive EPV anomaly above the tropopause, and the temperature contribution showed negative EPV anomalies on the tropopause over much of the time period. Both of these effects act to weaken a vortex.

While cloud properties were not included in the composite analysis, cloud properties associated with TPVs were analyzed separately. Total column-integrated IWP and LWP were averaged over a 12 hour period surrounding the TPV's core as it passed over Summit. Results show that smaller and weaker TPVs in the dataset contained more ice and liquid in the core, and many of these cases were weakening on average over the 12-hour time period. The radiative contribution of clouds was considered by comparing the average

of the clear-sky radiative heating rate anomalies on the tropopause to the average all-sky radiative heating rate anomalies on the tropopause for all cases in the analysis. It was found that while many cases maintained positive clear-sky heating rate anomalies on the tropopause (as was also found in the composites), many of the all-sky radiative heating rates changed from positive to negative anomalies. Only 3 of the cases that changed from a positive to a negative anomaly on the tropopause when including clouds in the RHR calculation were cases of strengthening TPVs, and several of the weakening cases with already negative anomalies gained stronger negative anomalies. More work needs to be done to understand just how clouds at the tropopause are influencing TPV evolution and on what time scale.

While most results from this study have agreed with previous studies or theoretical expectations, it is important to note that differences in analysis techniques may lead to some discrepancies between various studies and literature. The use of composites to analyze a general structure based on a dataset of TPVs would be improved by using a larger sample size or a different sample with more controlled variables. For example, by choosing a dataset of only TPVs with amplitudes and radii above a certain threshold, features may be more apparent in composites. However, true isolation of variables, such as those outlined in table 2.2, is difficult when using observations, since the presence of clouds will influence the atmospheric state of the environment even in the clear-sky runs. In terms of TPVs, all cases are unique in many ways, e.g., their speed, direction of movement, size, shape, season, strength, etc. Like many meteorological phenomena, no two are exactly the same. Composite structures and radiative features will be influenced by such differences without a method for controlling these variables, so analyses may be improved or new details uncovered by compositing based on specific features. To do this, a much larger sample size is needed in order to more robustly sample the spectrum of TPVs. With this in mind, the analysis done here could be improved by making use of other Arctic observatories to include many more cases. TPV cases here were limited to years with data available from

the instruments at Summit as well as cases that crossed Summit in close enough proximity to even use this data. These limitations significantly reduced the number of cases available for analysis. By involving other Arctic observatories with similar observing instruments, this analysis could be expanded to include many more observed TPVs.

Going forward, more analysis needs to be done to determine if, and how significantly, the location of RHR anomalies is important in the intensification or weakening of TPVs. The strength of the vertical RHR gradient across the tropopause is an important factor in evolution, however the strength of this gradient has not been studied specifically. Since latent heating has also been shown to be an important factor in destroying EPV and therefore weakening TPVs, an analysis including latent heating may help discern some details of TPV evolution in observed cases. Along with latent heating, shortwave radiation was also neglected in this analysis as a way to control the experiments, however during the summer months the small effects from shortwave radiation may be significant in changing TPV evolution, and in future work this needs to be considered as well. As a final note, ERA5 was the sole reanalysis dataset used in this study. Weaknesses and/or biases of this reanalysis have not been considered in this analysis. For completeness, an important next step would be considering how the results from this study hold through use of various other reanalysis datasets.

Bibliography

Bennartz, R., and Coauthors, 2013: July 2012 Greenland melt extent enhanced by low-level liquid clouds. *Nature*, **496**, 83–86.

Cavallo, S. M., and G. J. Hakim, 2009: Potential vorticity diagnosis of a tropopause polar cyclone. *Monthly Weather Review*, **137 (4)**, 1358–1371, doi:10.1175/2008MWR2670.1.

Cavallo, S. M., and G. J. Hakim, 2010: Composite structure of tropopause polar cyclones. *Monthly Weather Review*, **138 (10)**, 3840–3857, doi:10.1175/2010MWR3371.1.

Cavallo, S. M., and G. J. Hakim, 2012: Radiative impact on tropopause polar vortices over the arctic. *Monthly Weather Review*, **140 (5)**, 1683–1702, doi:10.1175/MWR-D-11-00182.1.

Cavallo, S. M., and G. J. Hakim, 2013: Physical mechanisms of tropopause polar vortex intensity change. *Journal of the Atmospheric Sciences*, **70 (11)**, 3359–3373, doi:10.1175/JAS-D-13-088.1.

Clough, S., M. Shephard, E. Mlawer, J. Delamere, M. Iacono, K. Cady-Pereira, S. Boukabara, and P. Brown, 2005: Atmospheric radiative transfer modeling: a summary of the AER codes. *Journal of Quantitative Spectroscopy and Radiative Transfer*, **91**, 233–244, doi:10.1016/j.jqsrt.2004.05.058.

Curry, J., 1983: On the formation of continental polar air. *Journal of the Atmospheric Sciences*, **40 (9)**, 2278–2292, doi:10.1175/1520-0469(1983)040⟨2278:OTFOCP⟩2.0.CO;2.

Curry, J. A., and G. F. Herman, 1985: Infrared radiative properties of summertime Arctic stratus clouds. *Journal of Climate and Applied Meteorology*, **24 (6)**, 525–538, doi:10.1175/1520-0450(1985)024⟨0525:IRPOSA⟩2.0.CO;2.

Curry, J. A., W. B. Rossow, D. Randall, and J. L. Schramm, 1996: Overview of Arctic cloud and radiation characteristics. *J. Climate*, **9**, 1731–1764, doi:10.1175/1520-0442(1996)009⟨1731:OOACAR⟩2.0.CO;2.

Edwards, C. A., and J. Pedlosky, 1998: Dynamics of nonlinear cross-equatorial flow. part i: Potential vorticity transformation. *Journal of Physical Oceanography*, **28 (12)**, 2382–2406, doi:10.1175/1520-0485(1998)028⟨2382:DONCEF⟩2.0.CO;2.

Hakim, G. J., L. F. Bosart, and D. Keyser, 1995: The Ohio Valley wave-merger cyclogenesis event of 25–26 January 1978. part i: Multiscale case study. *Monthly Weather Review*, **123 (9)**, 2663–2692, doi:10.1175/1520-0493(1995)123⟨2663:TOVWMC⟩2.0.CO;2.

Hakim, G. J., and A. K. Canavan, 2005: Observed cyclone–anticyclone tropopause vortex asymmetries. *Journal of the Atmospheric Sciences*, **62 (1)**, 231–240, doi:10.1175/JAS-3353.1.

Herman, G., and R. Goody, 1976: Formation and persistence of summertime Arctic stratus clouds. *Journal of the Atmospheric Sciences*, **33 (8)**, 1537–1553, doi:10.1175/1520-0469(1976)033⟨1537:FAPOSA⟩2.0.CO;2.

Holton, J. R., 2004: *An introduction to dynamic meteorology*. 4th ed., International Geophysics Series, Elsevier Academic Press,, Burlington, MA, 535 pp., URL http://books.google.com/books?id=fhW5oDv3EPsC.

Hoskins, B. J., M. E. McIntyre, and A. W. Robertson, 1985: On the use and significance of isentropic potential vorticity maps. *Quarterly Journal of the Royal Meteorological Society*, **111 (470)**, 877–946, doi:10.1002/qj.49711147002.

Intrieri, J. M., C. W. Fairall, M. D. Shupe, P. O. G. Persson, E. L. Andreas, P. S. Guest, and R. E. Moritz, 2002a: An annual cycle of Arctic surface cloud forcing at SHEBA. *Journal of Geophysical Research: Oceans*, **107 (C10)**, SHE 13–1–SHE 13–14, doi:10.1029/2000JC000439.

Intrieri, J. M., M. D. Shupe, T. Uttal, and B. J. McCarty, 2002b: An annual cycle of Arctic cloud characteristics observed by radar and lidar at SHEBA. *Journal of Geophysical Research: Oceans*, **107 (C10)**, SHE 5–1–SHE 5–15, doi:10.1029/2000JC000423.

Lacour, A., H. Chepfer, M. D. Shupe, N. B. Miller, V. Noel, J. Kay, D. D. Turner, and R. Guzman, 2017: Greenland clouds observed in CALIPSO-GOCCP: Comparison with ground-based summit observations. *Journal of Climate*, **30 (15)**, 6065–6083, doi:10.1175/JCLI-D-16-0552.1.

Miller, N. B., D. D. Turner, R. Bennartz, M. D. Shupe, M. S. Kulie, M. P. Cadeddu, and V. P. Walden, 2013: Surface-based inversions above central Greenland. *Journal of Geophysical Research: Atmospheres*, **118 (2)**, 495–506, doi:10.1029/2012JD018867.

Morrison, H., G. Boer, G. Feingold, J. Harrington, M. Shupe, and K. Sulia, 2011: Resilience of persistent Arctic mixed-phase clouds. **5**, 11–17.

Serreze, M. C., A. P. Barrett, and J. Stroeve, 2012: Recent changes in tropospheric water vapor over the Arctic as assessed from radiosondes and atmospheric reanalyses. *Journal of Geophysical Research: Atmospheres*, **117 (D10)**, doi:10.1029/2011JD017421.

Serreze, M. C., R. G. Barry, and J. E. Walsh, 1995: Atmospheric water vapor characteristics at 70n. *Journal of Climate*, **8 (4)**, 719–731, doi:10.1175/1520-0442(1995)008⟨0719:AWVCA⟩2.0.CO;2.

Serreze, M. C., R. C. Schnell, and J. D. Kahl, 1992: Low-level temperature inversions of the Eurasian Arctic and comparisons with soviet drifting station data. *Journal of Climate*, **5 (6)**, 615–629, doi:10.1175/1520-0442(1992)005⟨0615:LLTIOT⟩2.0.CO;2.

Shupe, M. D., 2011: Clouds at Arctic atmospheric observatories. part ii: Thermodynamic phase characteristics. *Journal of Applied Meteorology and Climatology*, **50 (3)**, 645–661, doi:10.1175/2010JAMC2468.1.

Shupe, M. D., and J. M. Intrieri, 2004: Cloud radiative forcing of the Arctic surface: The influence of cloud properties, surface albedo, and solar zenith angle. *Journal of Climate*, **17 (3)**, 616–628, doi:10.1175/1520-0442(2004)017⟨0616:CRFOTA⟩2.0.CO;2.

Shupe, M. D., D. D. Turner, A. Zwink, M. M. Thieman, E. J. Mlawer, and T. Shippert, 2015: Deriving Arctic cloud microphysics at Barrow, Alaska: Algorithms, results, and radiative closure. *Journal of Applied Meteorology and Climatology*, **54 (7)**, 1675–1689, doi:10.1175/JAMC-D-15-0054.1.

Shupe, M. D., V. P. Walden, E. Eloranta, T. Uttal, J. R. Campbell, S. M. Starkweather, and M. Shiobara, 2011: Clouds at Arctic atmospheric observatories. part i: Occurrence and macrophysical properties. *Journal of Applied Meteorology and Climatology*, **50 (3)**, 626–644, doi:10.1175/2010JAMC2467.1.

Shupe, M. D., and Coauthors, 2013: High and dry: New observations of tropospheric and cloud properties above the Greenland Ice Sheet. *Bulletin of the American Meteorological Society*, **94 (2)**, 169–186, doi:10.1175/BAMS-D-11-00249.1.

Simmonds, I., and I. Rudeva, 2012: The great Arctic cyclone of August 2012. *Geophysical Research Letters*, **39 (23)**, doi:10.1029/2012GL054259.

Szapiro, N., and S. Cavallo, 2018, in review: Tpvtrack v1.0: A watershed segmentation and overlap correspondence method for tracking tropopause polar vortices. *Geoscientific Model Development Discussions*, **39 (23)**, 1–27, doi:10.5194/gmd-2018-180.

Turner, D. D., 2007: Improved ground-based liquid water path retrievals using a combined infrared and microwave approach. *Journal of Geophysical Research: Atmospheres*, **112 (D15)**, doi:10.1029/2007JD008530.

Turner, D. D., M. D. Shupe, and A. B. Zwink, 2018: Characteristic atmospheric radiative heating rate profiles in Arctic clouds as observed at Barrow, Alaska. *Journal of Applied Meteorology and Climatology*, **57 (4)**, 953–968, doi:10.1175/JAMC-D-17-0252.1.

Uttal, T., and Coauthors, 2002: Surface heat budget of the Arctic ocean. *Bulletin of the American Meteorological Society*, **83 (2)**, 255–276, doi:10.1175/1520-0477(2002)083⟨0255:SHBOTA⟩2.3.CO;2.

Wexler, H., 1936: Cooling in the lower atmosphere and the structure of polar continental air. *Monthly Weather Review*, **64 (4)**, 122–136, doi:10.1175/1520-0493(1936)64⟨122:CITLAA⟩2.0.CO;2.